NTNU
Norwegian University of Science and Technology

Efficient rotor modelling for real-time hybrid testing

Jingyi Yu

Norwegian University of Science and Technology
Department of Marine Technology

TUDelft

Technische Universiteit Delft

NTNU – Trondheim
Norwegian University of
Science and Technology

EWEM

European Wind Energy Master

DELFT UNIVERSITY OF TECHNOLOGY

NORWEGIAN UNIVERSITY OF SCIENCE AND TECHNOLOGY

Preface

This master thesis is performed under the supervision of Norwegian University of Technology and Science (NTNU) and Delft University of Technology (TU Delft) during the spring semester in 2017.

Small-scale model tests in wave basins are important tools for validating numerical tools, evaluating system performance, and studying physical phenomena related to floating wind turbines. In order to model waves accurately, Froude scaling is applied in model scale tests, but a consistent scaling of the wind turbine will result in a reduced Reynolds number compared to the prototype, which leads to generally poor aerodynamic performance. In order to solve such a Froude-Reynolds scaling conflict, a real-time hybrid model test was designed and carried out in SINTEF Ocean. The aerodynamic loads were calculated numerically and applied to the physical model. In order to capture the interaction between the wind-induced and wave-induced responses, the aerodynamic loads must be calculated in real time based on the measured platform positions.

One disadvantage of the NOWITECH experiments in 2015 is that it used a rigid rotor model for the aerodynamic loads in order to minimize the calculation time. The purpose of this master's thesis project is to develop an efficient flexible structural model of the rotor, including the blade bending and torsion deflections, which is coupled to an aerodynamic code such as AeroDyn.

First, a flexible blade model is developed. The blade is assumed to be an Euler-Bernoulli cantilever beam. The stretch, flapwise bending, edgewise bending and torsion deflections are considered. The blade kinetic energy and potential energy are established using a set of hybrid coordinates. The equations of motion are obtained by Hamilton's principle. Finite element analysis is applied to calculate the blade natural frequencies and eigenmodes. Modal analysis is carried out in the time domain, coupled with AeroDyn to simulate the aerodynamic loads.

In the thesis, emulated ReaTHM testing is carried out. The tower, floater and mooring lines are modeled in SIMO-RIFLEX which can interact with the flexible blade model and the AeroDyn code through a dynamic link library(DLL). The computational efficiency of the presented flexible blade model is discussed. The set up of the emulated ReaTHM test is verified by decay tests

and tests in irregular wind and wave.

Then, the effects of blade flexibility in the ReaTHM test are investigated. ReaTHM testing with rigid blades is more conservative for the considered semi-submersible concept. Since 2015 NOWITECH ReaTHM test used a rigid tower model, using flexible blades model will not lead to a significant difference. However, if SINTEF Ocean plans to do the ReaTHM test with tension leg platform(TLP), it is recommended to use the developed methodology to see if flexible blades should be used.

Finally, a sensitivity analysis of limited actuations is carried out. In principle, all six components of simulated aerodynamic loads should be applied on the physical model. The sensitivity analysis shows that, for the semi- submersible in question, the aerodynamic heave force can be removed.

Acknowledgment

First of all, I would like to thank the European Wind Energy Master (EWEM) program, and the program coordinates Prof. Torgier Moan at Norwegian University of Technology and Science (NTNU) and Prof. Andrei Metrikine at Delft University of Techology (TU Delft). It is an exciting master program, from which I not only improved my academic skills but also experienced different cultures in three countries.

I would also like to give my warmest thanks to Prof. Erin Bachynski at NTNU for her supervision and weekly meetings. I am highly appreciated for her help and suggestions. And I am also grateful for Prof. Eliz-Mari Lourens at TU Delft for her co-supervision. During the thesis, I benefited a lot from the discussions with PhD candidate Ping Fu. And PhD candidate Yuna Zhao gave me helpful SIMA guidances.

In addition, I would like to give my sincere thanks to my parents, for their supports, understanding and love. And I am appreciated for the friendships with my classmates in the EWEM program. Thanks for their help and understanding, my life in Denmark, the Netherlands and Norway, was colorful and interesting.

O.N.

(Jingyi Yu)

Contents

Nomenclature

Roman Symbols

a	Axial induction factor
a'	Tangential induction factor
A_0	Aero at the inlet
A_1	Aero at the outlet
A	Blade cross section; Area of the rotor
B	Number of blades
c	Chord line length
C_d	Drag coefficient
C_l	Lift coefficient
C_p	Power coefficient
C_{pmax}	Maximum power corfficient(Betz limit)
d_e	Element deformation vector
dT	Thrust from an annular ring of the rotor
dQ	Torque from an annular ring of the rotor
D	Drag force per length
E	Young's modulus
f_e	Element external force matrix
f	Global external force matrix
F	Prandtl' tip loss factor
F_r	Froude number
g	Gravity
g_e	Element gyroscopic matrix
G	Shear modulus
G	Global gyroscopic matrix
h_e	Beam element length
H_i	Hermite interpolation functions

I	Moment of inertia
I_1	Moment of intertia with respect to principle axis 1
I_2	Moment of intertia with respect to principle axis 2
I_y	Moment of intertia with respect to axis y
I_z	Moment of intertia with respect to axis z
I_{yz}	Product of intertia
$\vec{i}, \vec{j}, \vec{k}$	Local reference frame for rotating blade
$\vec{i}_b, \vec{j}_b, \vec{k}_b$	Unit length in local hub reference frame
$\vec{i}_{ele}, \vec{j}_{ele}, \vec{k}_{ele}$	Unit length in local blade element reference frame
$\vec{i}_h, \vec{j}_h, \vec{k}_h$	Unit length in local hub reference frame
$\vec{i}_s, \vec{j}_s, \vec{k}_s$	Unit length in local shaft reference frame
$\vec{I}, \vec{J}, \vec{K}$	Unit length in global XYZ reference frame
J	Moment of torsion
k_e	Element stiffness matrix
K	Global stiffness matrix
K_D	Blade-pitch controller derivative gain
K_I	Blade-pitch controller integral gain
K_P	Blade-pitch controller proportional gain
L	Lift force per length; Blade length
$\mathscr{L}$	Lagrangian density function or Lagrangian functional
$\dot{m}$	Mass flow rate
m_e	Element mass matrix
M	Global mass matrix
N_{Gen}	High-speed to low-speed gearbox ratio
$\mathbf{N_s}$	Shape function for stretch displacement
$\mathbf{N_v}$	Shape function for chordwise displacement
$\mathbf{N_w}$	Shape function for flapwise displacement
$\mathbf{N_\phi}$	Shape function for torsion displacement
p_0	Ambient pressure
p, p_B	Pressure just in front of the rotor the rotor

p_A	Pressure just behind the rotor the rotor
p_N	Force normal to rotor plane per length
p_T	Force tangential to rotor plane per length
P	Rotor power
Q	Rotor Torque
r	Local blade radius
R	Rotor radius
R_e	Reynolds number
R_{hub}	Hub radius
s	Total stretch length
$\bar{s}$	Weighting functions for the stretch deformation
s_e	Element motion-induced stiffness matrix
S	Global motion-induced stiffness matrix
T	Thrust force; Kinetic energy
T_{Aero}	Low-speed shaft aerodynamic torque
T_{Gen}	High-speed shaft aerodynamic torque
u	Horizontal wind velocity at the rotor; Blade axial deformation
U	Wave celerity
U_∞	Horizontal inflow wind velocity
v	Lateral wind velocity at the rotor; Blade chordwise deformation
$\bar{v}$	Weighting functions for the chordwise deformation
V_∞	Lateral inflow wind velocity
V_0	Inflow velocity
V_1	Wind velocity far from the rotor
$\vec{V}_p$	Velocity vector of point P
V_{rel}	Relative velocity seen by a section of the blade
w	vertical wind velocity at the rotor; Blade flapwise deformation
$\bar{w}$	Weighting functions for the flapwise deformation
W_∞	vertical inflow wind velocity
$\mathscr{W}$	Work done on the system by non-conservative forces

Greek Symbols

α_c	Precone angle
α_p	Pitch angle
α_t	Tilt angle
β	Twist of the blade
θ	Pitch angle
λ	Tip speed ratio
	Froude scaling factor
λ_r	Local speed ratio
μ	Number of mode shapes
ρ	Material density
ϕ	Angle between the plane of rotation
	Torsion angle
$\bar{\phi}$	Weighting functions for the torsion deformation
Φ	Mode shape
φ	Blade rotation angle
η	Dummy variable
ω	Angular velocity imparted to the free stream
Ω	Angular velocity of rotor
σ	Solidity
χ	Azimuth angle
Δp	Pressure jump at the rotor disk
Π	Potential energy

Abbreviations

1D	One dimensional
2D	Two dimensional
BEM	Blade Element Momentum
¨ CAE	Computer-aided-engineering
COE	Cost of energy
eReaTHM(F)	Emulated real-Time Hybrid Model Testing with flexible blades
eReaTHM(R)	Emulated real-Time Hybrid Model Testing with rigid blades
EWEA	European Wind Energy Association
FWT	Floating wind turbine
GDW	Generalized Dynamic Wake
LCOE	Levelised cost of energy
NREL	National Renewable Energy Laboratory
OWT	Offshore wind turbine
PRVS	Pitch-regulated variable speed
ReaTHM	Real-Time Hybrid Model Testing

List of Figures

List of Tables

Chapter 1

Introduction

1.1 Offshore Wind Energy

Wind energy provides a promising clean energy solution for the future. Compared to onshore wind energy, the advantages of offshore wind energy can be summary as[1]:(1)steadier and stronger wind, implying greater electricity production;(2)mitigate or eliminate the issues of visual impact and noise; (3)huge areas available for the installation of large wind parks.

The development of offshore wind energy has been focused on Europe. Since the success of the first offshore wind farm Vindeby in Denmark[2], the offshore wind industry has experienced a rapid growth. At the end of 2016, shown in Figure(1.1), 12.6 GW offshore wind power capacity has been installed in the EU[3], which accounts for 8.2% of the total installed wind power capacity. According to the European Wind Energy Association(EWEA), 40 GW offshore wind energy will be installed, meeting 4% of European electricity demand by 2020. By 2030, offshore wind capacity could total 150 GW, meeting 14% of the EU's total electricity consumption[4].

Currently, commercial offshore wind projects are limited to a water depth less than 50m with bottom fixed structures, but there is a trend toward be installed in deeper water(Figure(1.2)). Deep offshore designs are necessary to unlock the promising offshore market potential in the Atlantic, Mediterranean and deep North Sea waters[4]. Compared to bottom fixed foundations, floating wind turbines are competitive in terms of the levelised cost of energy (LCOE) in more than 5Om water depth[4]. However, the technology is still at a very early stage of development. Experimental methods for offshore wind turbines should be used to verify the new design con-

cepts.
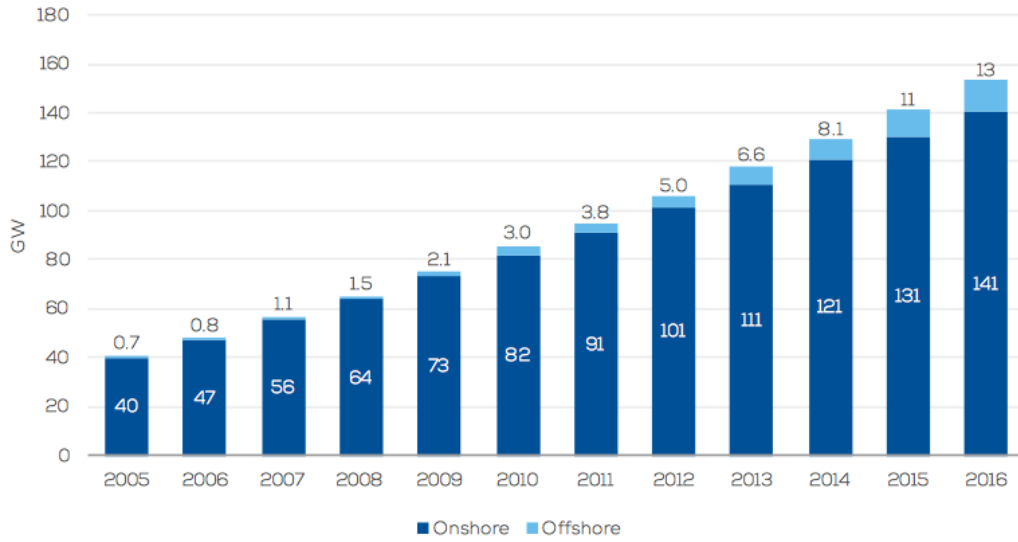
Figure 1.1: Cumulative installations onshore and offshore in the EU. Total 153.7 GW[3]
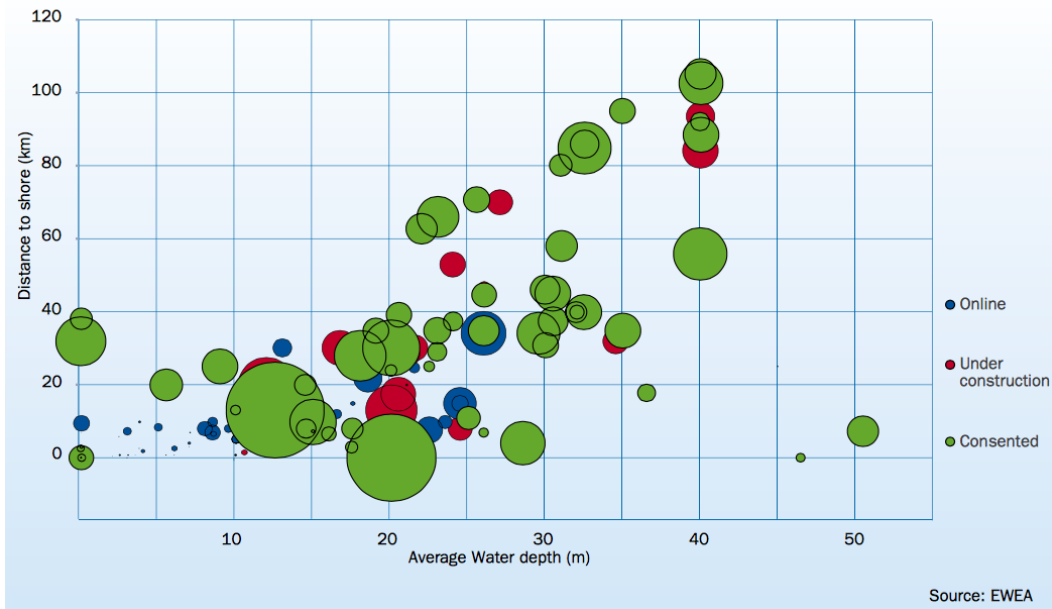
Figure 1.2: Water depth, distance to shore for offshore wind farm [4]

1.2 Experimental methods for offshore wind turbines

Floating wind turbines may be more competitive in deep water(>50m), demonstration projects such as Statoil's Hywind and Principle Power's WindFloat have been built. But no commercial projects have been installed. In order to verify novel designs and validate computer-aided-engineering (CAE) tools[5], model tests should be carried out.

1.2.1 Froude-Reynolds scaling conflict

Hydrodynamic tests usually follow Froude scaling and geometric similarity. Thus, the dominant factors in the hydrodynamic problem, such as gravity and inertia, are properly scaled.

The Froude number is :

$$Fr = U/\sqrt{gL}$$

where U is the wave celerity, g is the local acceleration due to gravity, and L is a characteristic length. Therefore, for hydrodynamic tests:

$$Fr_m = Fr_f$$

where the subscript m, f represent model and full scale prototype, respectively.

The geometric similarity is given as:

$$L_m = \lambda L_f$$

However, under Froude scaling, the Reynolds number is reduced, resulting in lower-than-desired values of thrust and aerodynamic torque. If the same fluid is used, the scale of Reynolds number can be expressed as:

$$Re_m/Re_f = \frac{\rho_m V_m L_m \mu_f}{\rho_f V_f L_f \mu_m} = \sqrt{\lambda}\lambda = \lambda^{3/2}$$

Assuming a $\lambda = 1:50$ model, the scale of the Reynolds number can be $1:353$. The Reynolds number is much lower, resulting in bad aerodynamic performance.

In 2011, the DeepCwind consortium[1] conducted a 1/50 model test campaign on various platform types at MARIN[2]. To counteract the reduced aerodynamic forces on the turbine during the scaled model testing, the wind speed was increased to ensure appropriately scaled thrust forces[5].

Another practical solution to improve the aerodynamic loads under Froude scaling, is to modify the blade airfoil to obtain desired thrust force under low model test Reynolds numbers[6]. However, it is currently impossible to simultaneously match the thrust, torque, and slope of the thrust curve adequately.

In order to solve the Froude-Reynolds scaling conflict, Real-Time Hybrid Model(ReaTHM) Testing[3] was carried out in SINTEF Ocean.

1.2.2   Real-time hybrid model testing

The main concept of Real-Time Hybrid Model Testing is to divide the whole model into two parts: (1) Physical substructure in model-scale; (2) Numerical substructure simulated on a computer. The two parts interact with each other in real-time through a network of sensors and actuators.

Sauder et al.[7] present a method for performing Real-Time Hybrid Model testing of a floating wind turbine (FWT), as shown in Figure(1.3). The physical substructure Froude scaled includes the semi-submersible of the 5-MW-CSC design[8], the tower design described in[9], and the turbine mass.

Aerodynamic and generator loads were estimated numerically. Then, wind loads were scaled down in Froude scaling and applied to physical model .This guaranteed a consistent scaling of the problem, and a controlled incoming wind field[7].

One advantage of this method is that all aerodynamic load components of importance were identified and applied on the physical model, while in previous similar projects, only the aerodynamic thrust force was applied on the physical model[7]. Further, a sensitivity analysis to

---

[1]DeepCwind consortium is a group of universities, national labs, and companies funded under a research initiative by the U.S. Department of Energy (DOE) to support the research and development of floating offshore wind power.

[2]Maritime Institute of the Netherlands in Wageningen, the Netherlands.

[3]$ReaTHM^{TM}$ testing, a trademark of MARINTEK.

limited actuation can be carried out. There are six components of aerodynamic loads: three aerodynamic forces along global x,y,z axis, one aerodynamic pitch moment, one aerodynamic yaw moment and one generator torque. In principle, all of these six components should be applied to the physical model. But, some aerodynamic load components are small, so the corresponding effects can be considered to be small as well. They can be removed to reduce the complexity of experiment setup while ensuring adequate fidelity.

However, one imperfection in the numerical model in 2015 NOWITECH ReaTHM test, was that the blades were assumed to be rigid. Consistently, the tower influence, generating impulse loads at a the triple of the rotor rotation frequency, and inducing blade vibrations, was neglected[7]. Flexible blades may improve the perfomance of the numerical model, but result in longer computation time. Therefore, a reasonable flexible blade model should be provided. This is the key motivation for this thesis work.
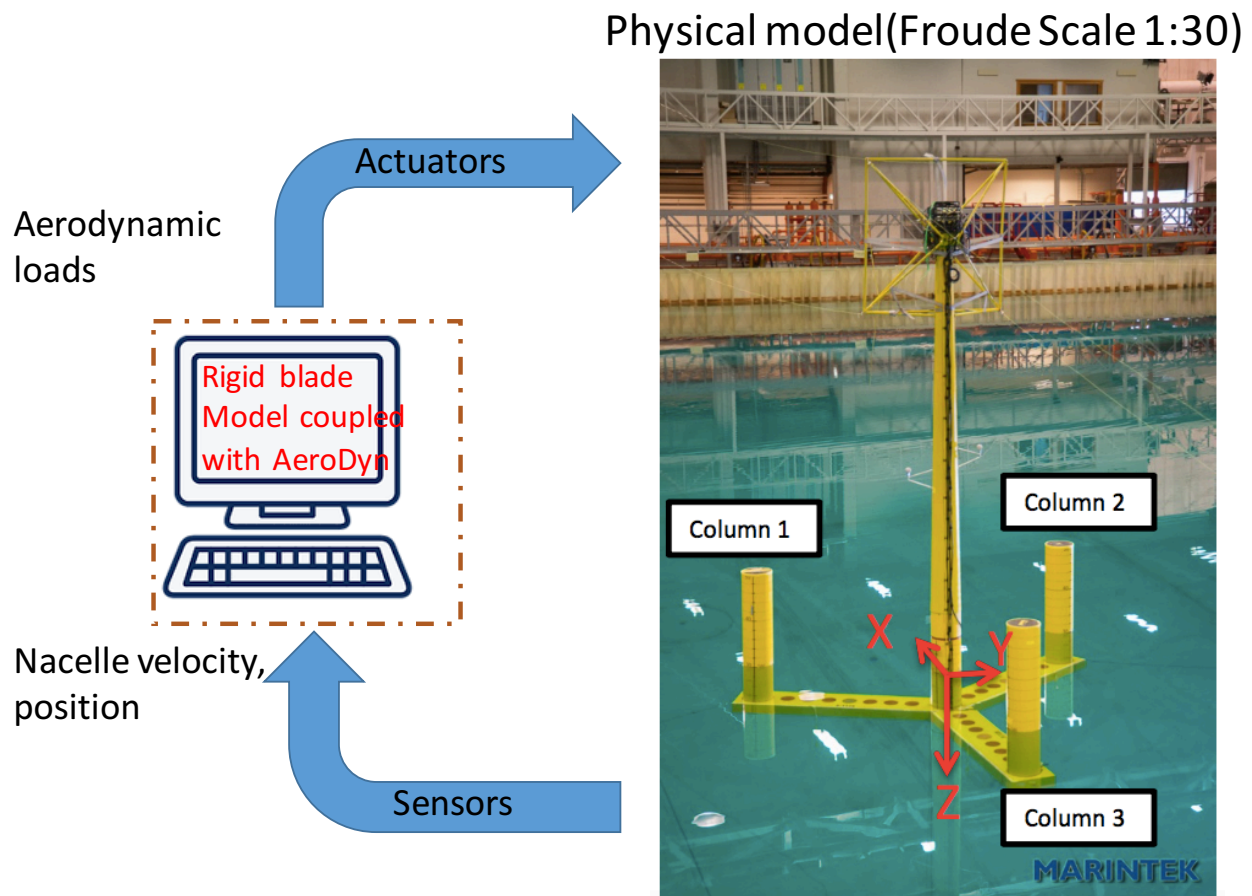
Figure 1.3: Illustration of 2015 NOWITECH Real-time Hybrid Model test

1.3   Research in blade dynamic motion

The problem of modelling the dynamics of rotating beams has received extensive researchers efforts in many areas of engineering applications, such as robot arms, space structures and rotating blades in turbo machinery.

According to Yoo et al.[10], the first modeling approach for rotating beams was introduced in the 1970s. This method is based on the classical linear elastic modelling(C.L.C.), where geometric and material linearity is assumed. The main advantage of this modeling approach is computational efficient. However, when the structures undergo large rotational motions, the approach can be inaccurate.

Some non-linear methods were also introduced based on non-linear relations between the strains and displacements, since the geometric linearity assumption is considered to be the cause for the inaccuracy. However, the non-linear approach requires high computational efforts[10].

Therefore, another modeling approch was provided using a set of hybrid coordinates (two Cartesian and one non-Cartesian). Yoo et al.[11] used this method to obtain the equations of motion and approximated the hybrid set of variables using the Rayleigh-Ritz method. The gyroscopic coupling effect between the stretch and bending motion was also discussed. Yoo et al.[12] derived the full non-linear equations of motion of an Euler-bernoulli beam, which were then linearized and their respective weak forms were derived for application in the finite element method. Yoo et al.[13] also presented equations of motion for the vibration analysis of rotating pre-twisted blades using the hybrid coordinates.

For a slender beam, Euler-Bernoulli beam theory is valid. When the slenderness ratio becomes lower and the beam is thick, Timoshenko beam theory should be applied because the shear stresses and the rotary inertia effects can be large. However, Ref.[14] shows that the differences on the first several natural frequencies are limited.

Ref.[15] reported a research on free vibration analysis of a rotating beam by differential transform method, include the shear deformation and rotary inertia effects

In this thesis, blades are assumed to be Euler-Bernoulli cantilever beams. Finite element analysis and modal analysis methods are applied. The detailed methods refer to analysis on[12] and [16].

1.4   Tools for dynamic analysis of floating wind turbines

For a floating wind turbine system, a method for the coupled structural, hydrodynamic, and aerodynamic analysis should be presented. Researchers have developed some analysis tools to capture the coupled aero-hydro-servo-elastic response of FWTs. Ref[17] presents an overview of the current status of the simulation codes that are capable of performing integrated dynamic calculations for floating offshore wind turbines, and makes a comparison between different tools.

In this thesis, the floating wind turbines(FWTs) analysis is carried out in Simo-Riflex-AeroDyn, while comparison is made with results from FAST-AeroDyn. Thus, in this section, a brief introduction is presented for these two tools.

FAST-AeroDyn

The FAST [4] Code is a publicly available simulation tool for horizontal-axis wind turbines, which was developed by the National Renewable Energy Laboratory (NREL)[18]. The FAST code is developed for land-based fixed-bottom wind turbines, but has been extended with a time-domain hydrodynamics module HydroDyn to enable dynamics analysis for floating wind turbines.

The aerodynamic loads in FAST is calculated using the AeroDyn module. AeroDyn is a series of routines developed by National Renewable Energy Laboratory(NREL), to perform the aerodynamic calculations for aeroelastic simulations of horizontal axis wind turbine configurations. Two aerodynamic models are included in AeroDyn for the effect of wind turbine wakes: the blade element momentum(BEM) theory and the generalized dynamic wake(GDW) theory[19]. BEM assumes static flow, 2D airfoils. GDW is better suited for dynamic inflow, yawed inflow, and higher wind speeds. An overview of aerodynamic models in AeroDyn is shown in Table(1.1).

The FAST code allows for two flapwise and one edgewise bending-mode DOF per blade and two fore-aft and two side-to- side bending-mode DOFs in the tower. Flexibility in the blades and tower is characterized using a linear modal representation that assumes small deflections within each member.

---

[4]Fatigue, Aerodynamics, Structures, and Turbulence

Table 1.1: An overall of the aerodynamic models in AeroDyn

	BEM	GDW
Dynamic Stall	Beddoes-Leishman	Beddoes-Leishman
Dynamic wake	not include	inherent
Tower shadow	Potential flow	Potential flow
Skewed inflow	Pitt and Peters	inherent
Tip Loss	Prandtl	Prandtl
Hub Loss	Prandtl	Prandtl

Simo-Reflex-AeroDyn Integration

Bachynski, E.E[20] has developed a SIMO-RIFLEX-AeroDyn code for the analysis of tension leg platform floating wind turbines in her Ph.D thesis. SIMO (Simulation of Marine Operations) is a time-domain simulation program developed by MARINTEK for the modelling and simulation of offshore structures[21]. RIFLEX is a non-linear FEM program developed by MARINTEK for static and dynamic analysis of slender marine structures[22]. The aerodynamic loads is calculated by AeroDyn based on BEM or GDW model which is the same as the FAST code.

One advantage for SIMO-RIFLEX-AeroDyn(SRA) code is that large volume hydrodynamics and second-order forces in FWT analysis is included[20]. Thus, the coupled simulation tool SIMO-RIFLEX-AeroDyn is well-suited to account for the hydrodynamic modeling of a range of different platforms.

In SIMO-RIFLEX-AeroDyn(SRA) code, the blades, tower and mooring lines are modelled as flexible beams. And the control system for the generator torque and blade pitch can be included.

1.5 Motivations and Structure of thesis

As shown in Figure(1.3), the 2015 NOWITECH Real-time Hybrid model test used a rigid blade assumption in its numerical model. In my thesis, the blades will be modelled to be flexible. And emulated Real-time hybrid model test will be carried out, shown in Figure(1.4). The nacelle, tower, floater and mooring lines in full scale, are modelled by SIMO-RIFLEX simulation tool. The

simulated aerodynamic loads are applied to the nacelle by a dynamic library link(DLL), and the nacelle's positions and velocities are passed to the modified AeroDyn code. The modified Aero-Dyn code can simulate the aerodynamic loads based on the flexible blades or the rigid blades model, so the investigation of the feasibility and the effects of blade flexibility in the ReaTHM test will be made. In addition, the sensitivity analysis of the limited actuation will be carried out by removing the components of the aerodynamic loads one by one.
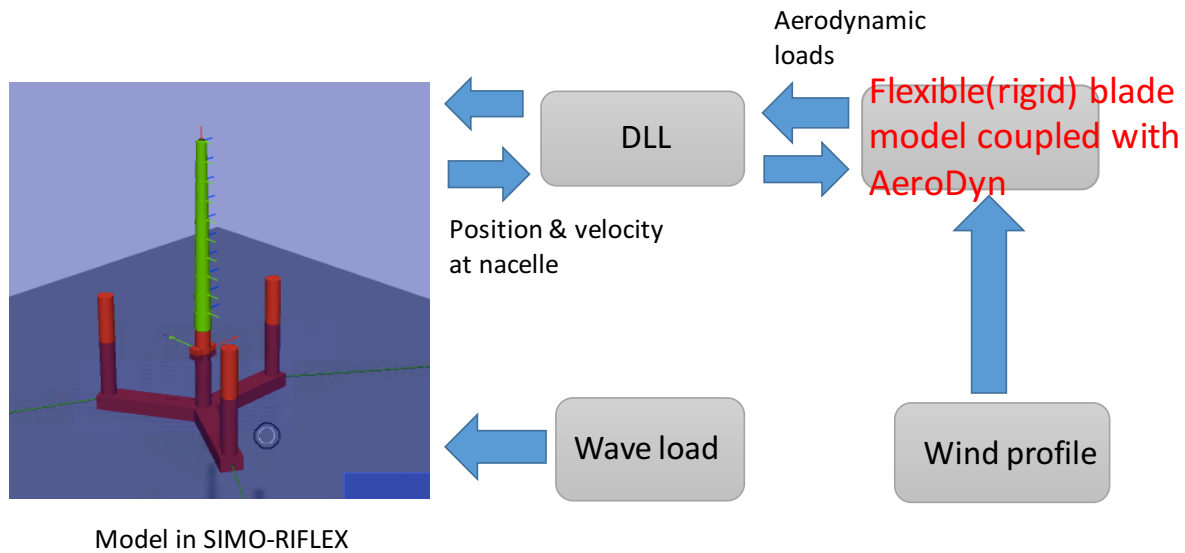
Figure 1.4: Illustration of the emulated ReaTHM test

This thesis is organized in nine chapters. In the present Chapter 1, an introduction of the thesis background is provided. And brief overviews of the problem of rotating cantilever beams, as well as simulation tools for floating wind turbines analysis are given.

In Chapter 2, the theoretical background is introduced, including aerodynamics models, pitch-regulated variable speed control and structural mechanics.

In Chapter 3, the blade kinetic energy and potential energy are established using a set of hybrid coordinates. The equations of motion are obtained by Hamilton's principle. And finite element analysis is applied to calculate the blade natural frequencies and eigenmodes.

Chapter 4 shows how to couple the flexible (or rigid) blade model with AeroDyn code.

The steady-state aerodynamic responses of the flexible and rigid blades are shown in Chapter 5. The results are compared to the results from FAST simulation tool.

In Chapter 6, the emulated real-time hybrid model test is set up and verified by decay tests

and tests in irregular wind and wave. In addition, the computational efficiency of the presented flexible blade model is discussed.

The effect of blade flexibility on the ReaTHM tests is discussed in Chapter 7.

Chapter 8 gives the sensitivity analysis to the limited actuation.

In the last chapter, the recommendations of ReaTHM test are given and some conclusions are drawn from the overall results obtained throughout this thesis.

Chapter 2

Theoretical Background

2.1 Aerodynamics Models

Many aerodynamic models are available from 1-D momentum theory to sophisticated computational fluid dynamics(CFD) method. In practice, blade element momentum(BEM) theory and generalized dynamic wake(GDW) methods are applied since they are computationally efficient and accurate for small blades deflections.

In the present thesis, AeroDyn code is used to calculate the aerodynamic forces. AeroDyn code is based on BEM and GDW methods, with some empirical corrections. And a comparison between BEM and GDW is presented in this section.

2.1.1 Blade Element Momentum Theory

Blade element momentum model can be used to calculate the steady loads and thus also the thrust and power for different settings of wind speed, rotational speed and pitch angle. The thrust and the torque from an annular ring based on momentum theory can be written as:

$$dT = 4a(1-a)\frac{1}{2}\rho V_0^2 2\pi r dr \tag{2.1}$$

$$dQ = 4a'(1-a)\frac{1}{2}\rho V_0 \Omega r^2 2\pi r dr \tag{2.2}$$
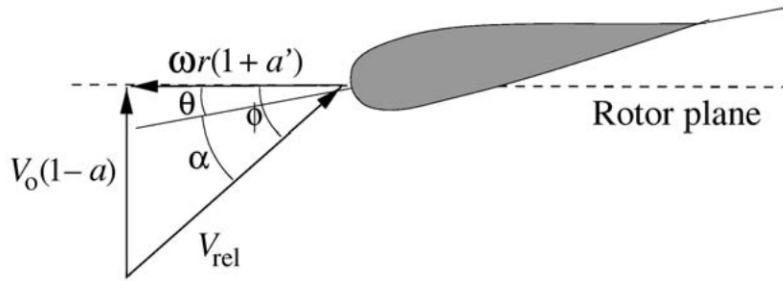
Figure 2.1: Velocities at the rotor plane[23]
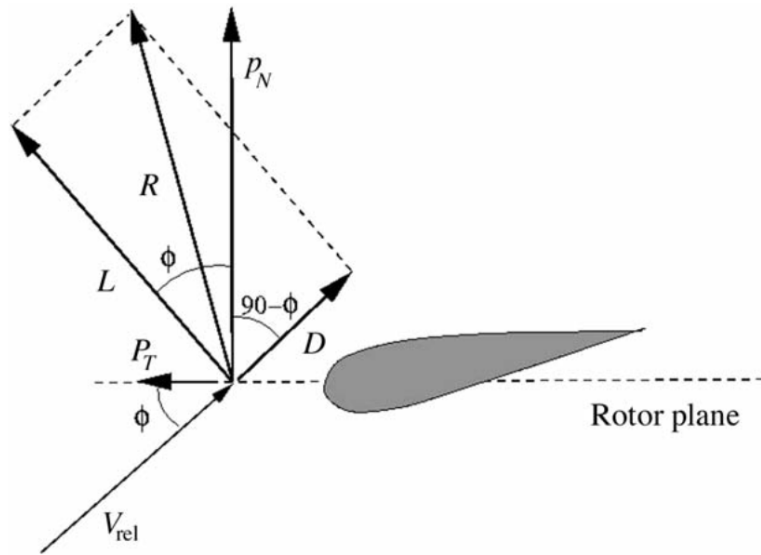
Figure 2.2: The local loads on a blade[23]

The angle ϕ between the plane of rotation and the relative velocity V_{rel} is:

$$\tan\phi = \frac{(1-a)V_0}{(1+a')\omega r} \qquad (2.3)$$

θ is the pitch angle of the blade;

β is the twist angele of the blade;

a is the axial induction factor while a' is the tangential induction factor.

By definition, the lift is perpendicular to the velocity seen by the aerofoil and the drag is parallel to the same velocity. Further, since the lift and drag coefficients C_l and C_d are known,

the lift L and drag D force per length can be found:

$$L = \frac{1}{2}\rho V_{rel}^2 c C_l \qquad D = \frac{1}{2}\rho V_{rel}^2 c C_d \tag{2.4}$$

The force normal to and tangential to the rotor plane is:

$$p_N = L\cos\phi + D\sin\phi \tag{2.5}$$

$$p_T = L\sin\phi - D\cos\phi \tag{2.6}$$

Eq(2.5) and Eq(2.6) are normalized with respect to $\frac{1}{2}\rho V_{rel}^2 c$ yielding:

$$C_n = C_l\cos\phi + C_d\sin\phi \tag{2.7}$$

$$C_t = C_l\sin\phi - C_d\cos\phi \tag{2.8}$$

A solidity σ is defined as the fraction of the annular area control volume which is covered by blades:

$$\sigma(r) = \frac{c(r)B}{2\pi r} \tag{2.9}$$

where B denotes the number of blades, $c(r)$ is the local chord and r is the radial position of the control volume.

The normal force can be found as:

$$dT = Bp_N dr = \frac{1}{2}\rho B \frac{V_0^2(1-a)^2}{\sin^2\phi} c C_n dr \tag{2.10}$$

Similarly, the torque can be expressed as :

$$dQ = \frac{1}{2}\rho B \frac{V_0(1-a)\omega r(1+a')}{\sin\phi\cos\phi} c C_t r dr \tag{2.11}$$

If Equation(2.1) and Equation(2.10) for dT are equalized, the axial induction is:

$$a = \frac{1}{4\sin^2\phi/\sigma C_n + 1} \tag{2.12}$$

And similarly, if Equation(2.2) and Equation(2.11) for dQ are equalized, the tangential induction is:

$$a' = \frac{1}{\dfrac{4\sin\phi\cos\phi}{\sigma C_t} + 1} \tag{2.13}$$

A more detailed description of BEM can be seen in Reference[23].

2.1.2 Empirical Corrections

2.1.2.1 Prandtl Correction

When blades rotate, vortices shed from the blade tips into the wake of induced wind field, which will result in the tip of the blade producing less aerodynamic force. To compensate for this deficiency in BEM theory, the Prandtl' tip loss factor can be used.

The expression is:

$$F = \frac{2}{\pi}\cos^{-1} e^{-f} \tag{2.14}$$

$$f = \frac{B(R-r)}{2r\sin\phi} \tag{2.15}$$

where B is the number of blades, R is the total radius of the rotor, r is the local radius and ϕ is the flow angle.

2.1.2.2 Hub Loss Correction

Like the tip loss model, the hub-loss model is used to correct the induced velocity resulting from a vortex being shed near the hub of the rotor. The hub-loss model is defined as:

$$f = \frac{B}{2}\frac{r - R_{hub}}{r\sin\phi} \tag{2.16}$$

For a given element, the tip loss factor and the hub loss factor should be multiplied to create the total loss.

2.1.2.3 Glauert Correction

BEM theory is only valid for induction factor less than 0.5. When induction factor is greater than 0.5, the wind velocity in the far away from the rotor will be negative. The Glauert correction factor is used for large induction factor: for $a > 0.4$. Different empirical relations between the thrust coefficient C_T and a can be made to fit with measurements, for example[23]:

$$C_T = \begin{cases} 4a(1-a)F & a \le \frac{1}{3} \\ 4a(1 - \frac{1}{4(5-3a)}a)F & a > \frac{1}{3} \end{cases}$$ (2.17)

Another empirical relation is[23]:

$$C_T = \begin{cases} 4a(1-a)F & a \le a_c \\ 4(a_c^2 + (1-2a_c)a)F & a > a_c \end{cases}$$ (2.18)

The last expression is found in Spera (1994) and a_c is approximately 0.2. F is Prandtl's tip loss factor and corrects the assumption of an infinite number of blade.

2.1.2.4 Skewed Wake Correction

Wind turbines operate at yaw angles relative to the incoming wind, which produces a skewed wake behind the rotor. The BEM model needs to be corrected to account for this skewed wake effect. The formulation used in AeroDyn is based on an equation originally developed by Glauert (1926) who was primarily interested in the autogyro[19]. The basic formula of the skewed wake correction he derived is:

$$a_{skew} = a[1 + K\frac{r}{R}\cos\chi]$$ (2.19)

where the constant K is a function of the skew angle; χ is defined as the azimuth angle.

2.1.2.5 Dynamic Wake Correction

BEM theory is considered quasi-static. The induction factor will immediately be updated if there is any change in the inflow wind velocity, the rotor speed and the blade pitch angle. The dynamic wake effect causes a time delay in the induced velocity. Dynamic wake effects are most

significant for heavily loaded rotors, corresponding to high induction factors.

In BEM procedure, this effect can be modelled by the Stig Øye dynamic inflow model, which acts as a filter for induced velocities[19].

2.1.3 Generalized Dynamic Wake

Generalized Dynamic Wake was originally developed for the helicopter industry, and it is also known as the acceleration potential method. GDW model of AeroDyn is based on the work of Peters and He (1989). The advantages and limitations of this method are summarized[19]:

Advantages

(1) Inherent include dynamic wake effect, tip losses, and skewed wake aerodynamics;

(2) The induced velocities are obtained from a set of first-order differential equations. Thus, no iterations are required.

Limitations

(1) In the case of the NREL 5MW turbine, it should not be used when wind velocity below 8m/s due to the instability ;

(2) Does not account for wake rotation. This method in AeroDyn also use BEM equation to calculate the tangential induction factor;

(3) The effect of large aeroelastic deflections is inaccurately modeled due to the assumption of flat disk.

Generalized Dynamic Wake is based on a potential flow solution to Laplace's equation. The Euler Equation is obtained from conservation of momentum for inviscid flow, assuming induced velocities are small compared to incident wind velocity:

$$\frac{\partial u_i}{\partial t} + U_{\infty j}\frac{\partial u_i}{\partial x_j} = -\frac{1}{\rho}\frac{\partial p}{\partial x_i} \tag{2.20}$$

The conservation of the mass can be derived as:

$$\frac{\partial u_i}{\partial x_i} = 0 \tag{2.21}$$

The pressure distribution can be obtained from Laplace's equation:

$$\nabla^2 p = 0 \tag{2.22}$$

The boundary conditions are given by the aerodynamic loading on the blade and the pressure returning to ambient pressure far from the rotor. Also, the discontinuity of the pressure across the rotor plane should equal the thrust force. To solve the set of governing equations, the dimensionless pressure field is split into two terms: one is the spatial variation of the pressure distribution, and one is the unsteadiness. A solution for the induced velocity distribution was obtained using an infinite series(He 1989) and the pressure distribution was developed by Kinner (1937). The detailed derivation and description can be seen in Reference[19].

2.2 Pitch-Regulated Variable Speed Control

For the NREL 5-MW baseline wind turbine, a pitch-regulated variable speed (PRVS) control system is used, which includes two independent basic controller: a generator-torque controller and a full-span rotor-collective blade-pitch controller[24].

PRVS wind turbines generate electricity between the cut-in wind velocity and cut-out wind velocity. In the below-rated wind region, the blade pitch angle keeps constant. The generator torque is increasing with the increase of wind speed so that the tip speed ratio λ is optimal. At the rated wind speed, the wind turbine reaches the rated torque, the rated rotor rotational speed and the rated thrust. In the above-rated wind region, the leading edge of the blades is pitched against the wind to reduce the angle of attack. Thus, the aerodynamic loads on the blade are reduced and the generator torque keeps constant.

2.2.1 Generator-torque controller

The generator torque is computed as a tabulated function of the filtered generator speed[24] in five regions as shown in Figure(2.3).
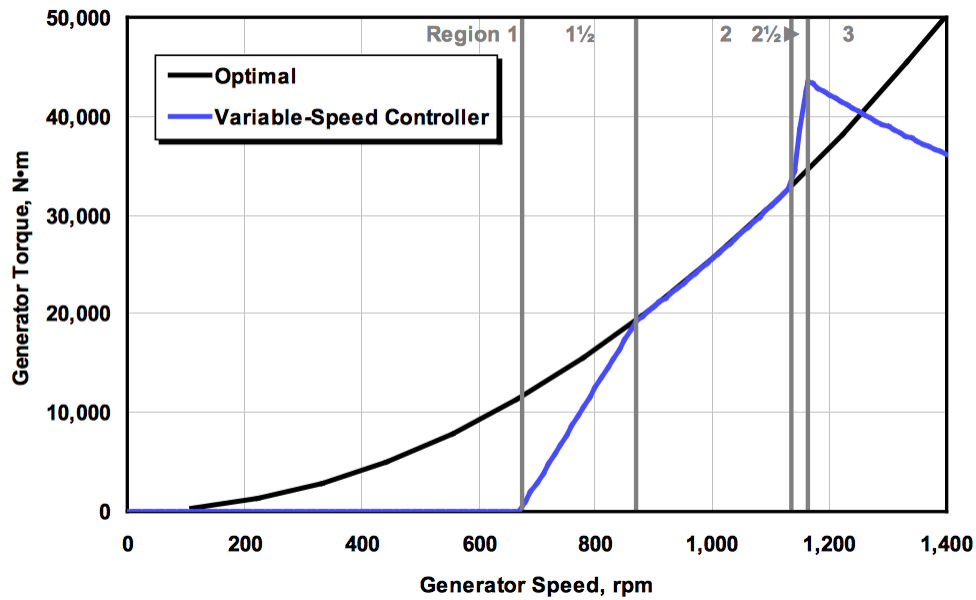
Figure 2.3: Torque-versus-speed response of the variable-speed controller[24]

Region 1 describes a control approach when the wind speed is below the cut-in speed. In this region, the generator torque is zero, which means no power is extracted from winds. Region $1\frac{1}{2}$, a start-up region, is a linear transition between Regions 1 and 2. This region is used to place a lower limit on the generator speed to limit the wind turbine's operational speed range[24]. Region 2 is a control region for below-rated wind speed. Here, the generator torque is proportional to the square of the filtered generator speed to maintain a optimal tip-speed ratio. Region $2\frac{1}{2}$ is a linear transition between Regions 2 and 3 with a torque slope corresponding to the slope of an induction machine. In Region 3, the generator power is held constant so that the generator torque is inversely proportional to the filtered generator speed.

2.2.2 Blade-Pitch Controller

In Region 3, the full-span rotor-collective blade-pitch-angle commands are computed using gain scheduled proportional-integral (PI) control on the speed error between the filtered generator speed and the rated generator speed (1173.7 rpm)[24].

The blade-pitch control system is modeled as a simple single-degree-of-freedom (single-

DOF) model of the wind turbine. The equation of motion is:

$$T_{Aero} - N_{Gear}T_{Gen} = (I_{Rotor} + N_{Gear}^2 I_{Gen})\frac{d}{dt}(\Omega_0 + \Delta\Omega) = I_{Drivetrain}\Delta\dot{\Omega} \qquad (2.23)$$

where T_{Aero} is the low-speed shaft aerodynamic torque, T_{Gen} is the high-speed shaft generator torque, N_{Gear} is the high-speed to low-speed gearbox ratio, $I_{Drivetrain}$ is the drivetrain inertia cast to the low-speed shaft, I_{Rotor} is the rotor inertia, I_{Gen} is the generator inertia relative to the high- speed shaft, Ω_0 is the rated low-speed shaft rotational speed, $\Delta\Omega$ is the small perturbation of low-speed shaft rotational speed about the rated speed, $\Delta\dot{\Omega}$ is the low-speed shaft rotational acceleration, and t is the simulation time.

In region 3, the generator power is constant. Thus, the generator torque in region 3 is defined as:

$$T_{Gen}(N_{Gear}\Omega) = \frac{P_0}{N_{Gear}\Omega} \qquad (2.24)$$

Assuming negligible variation of aerodynamic torque with rotor speed, the aerodynamic torque in Region 3 is:

$$T_{Aero}(\theta) = \frac{P(\theta, \Omega_0)}{\Omega_0} \qquad (2.25)$$

Reference[24] neglects the derivative gains $K_D = 0.0s^2$, and defines the blade-pitch controller proportional $K_P = 0.01882681s$, the integral gains $K_I = 0.008068634$, which is for the land-based wind turbines.

2.2.3 Modification to control systems

In above-rated wind region, assume the FWT has a small velocity in the same direction as the wind, which means the relative velocity between wind and the FWT is smaller. If the blades are pitched to maintain power output, the thrust force applied on the structure will increase, leading to further motion into the wind.Thus, the motion amplitude would be enlarged, which could lead to instability. The FWT has a negative feedback in this situation. In order to solve this problem, the modifications to the control systems from Reference[9] are used.

The first modification is to change the controller frequency. For a semi-submersible FWT, the platform surge and pitch natural frequency are generally lower than the controller frequency

(0.6 rad/s), but the surge damping is generally large enough to avoid unstable response. Reference[9] reduces the controller-response natural frequency to 0.2 rad/s to ensure that it is lower than the platform-pitch natural frequency and also lower than wave-excitation frequency of most sea states.

Another modification in control region 3, Figure(2.3) is made: constant generator torque is applied, instead of constant generator' power. This tends to improve the platform behavior, although power fluctuation may increase.

Table 2.1: Control system parameters

	Original	Modified
K_I at Min. pitch Setting	0.008068634	0.006275604
K_P at Min. pitch Setting	0.01882681 s	0.0008965149 s
$\omega_{\varphi n}$	0.6rad/s	0.2rad/s
strategy on Region 3	constant power	constant torque

2.3 Structural Mechanics

One objective of present work is to provide a structural dynamic model for blades. In this section, finite element analysis and modal analysis are introduced. The natural frequency and eigenmodes can be obtained by eigenvalue decomposition and modal analysis can be carried out in the time domain.

2.3.1 Euler-Bernoulli beam theory

Blades can be modeled as a Timoshenko beam or an Euler-Bernoulli beam. However, for a slender beam, the rotary inertia and the shear deformation are not significant and can be ignored. Thus, in the present work, Euler-Bernoulli beam theory is applied on blades. The assumptions are listed:

- 1. The cross-section of a beam remains plane and normal to the deformed axis of the beam after deformation;

- 2. The deflections are small;

- 3. Shear deformations are neglected.
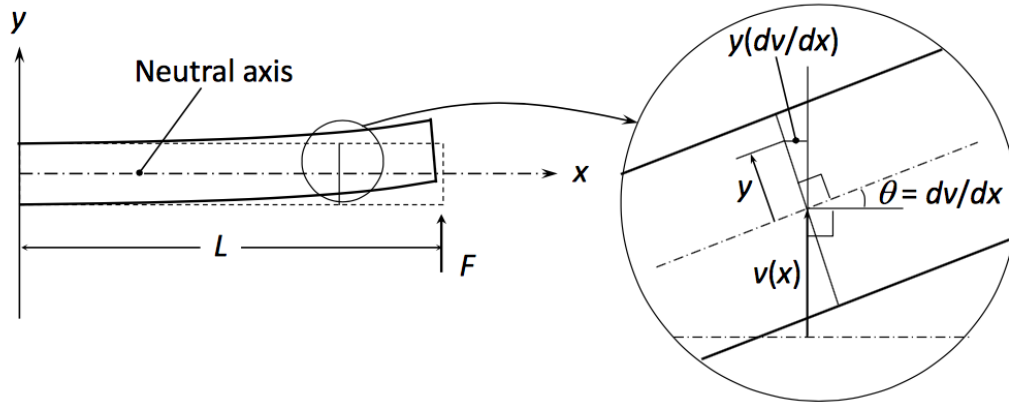
Figure 2.4: Illustration of deflection of Euler-Bernoulli beam

The displacement of point P for a small strain is given by:

$$u(x, y, z) = u_0 - y\frac{dv}{dx} - z\frac{dw}{dx} \tag{2.26}$$

Then, the strain is:

$$\epsilon_{xx} = \frac{\partial u}{\partial x} = \frac{du_0}{dx} - y\frac{d^2 v}{dx^2} - z\frac{d^2 w}{dx^2} \tag{2.27}$$

The axial force and bending moment are derived as:

$$P = EA\frac{du_0}{dx} \tag{2.28}$$

$$M = EI_{yy}\frac{d^2 v}{dx^2} + EI_{zz}\frac{d^2 w}{dx^2} \tag{2.29}$$

where EA is axial rigidity and EI is flexural rigidity.

2.3.2 Finite element analysis

The finite element method (FEM) is a discretization technique in structural mechanics. The basic concept of the FEM is the subdivision of the model into disjoint and non-overlapping

components of simple geometry called finite elements or elements for short. The response of each element is expressed in terms of a finite number of degrees of freedom characterized as the value of an unknown function, or functions, at a set of nodal points.

In the present work, Hamiltion's principle is used to derive the differential equations of motions for a blade. Then, the beam element is defined by two nodes. The displacements are approximated by linear interpolation for stretch and torsion motion, while cubic interpolation for flapwise and edgewise motion. Eigenvalue analysis is also carried out in order to obtain the structure natural frequencies and eigenmodes.

2.3.2.1 Hamilton's principle

The extended Hamilton's principle will be used to derive the differential equations of motion.

$$\delta \int_{t_1}^{t_2} (\mathscr{L} + \mathscr{W}) dt = 0 \tag{2.30}$$

where $\mathscr{L}$ is known as the Lagrangian density function or Lagrangian functional, and $\mathscr{W}$ is work done on the system by non-conservative forces.

The Lagrangian functional $\mathscr{L}$ is related to both kinetic and potential energy, T and Π respectively, and it is given by the following equation:

$$\mathscr{L} = T - \Pi \tag{2.31}$$

Introducing Equation(2.31) into Equation(2.30) and the variational and integration operators are interchangeable, Hamilton's principle can also be stated as:

$$\int_{t_1}^{t_2} (\delta T - \delta \Pi) dt = 0 \tag{2.32}$$

Assume V_P to be the velocity vector of any generic point P of the mechanical system, then the kinetic energy can be determined:

$$T = \frac{1}{2} \int_{v} \rho \boldsymbol{V_P}^T \cdot \boldsymbol{V_P} dV \tag{2.33}$$

where ρ is the material density. The strain energy for Euler–Bernoulli Beam is listed:

- Lateral displacement $\dfrac{1}{2}\int_0^L EI(\dfrac{d^2v}{dx^2})^2 dx$

- Axial displacement $\dfrac{1}{2}\int_0^L EA(\dfrac{du}{dx})^2 dx$

- Torsion $\dfrac{1}{2}\int_0^L GJ(\dfrac{d\phi}{dx})^2 dx$

2.3.2.2   Natural frequency from FEM

The governing equations for structural dynamics can be formulated based on the virtual work. The global form of the governing equation can be written as Eq(2.34):

$$\boldsymbol{M}\ddot{\boldsymbol{d}} + \boldsymbol{B}\dot{\boldsymbol{d}} + \boldsymbol{C}\boldsymbol{d} = \boldsymbol{F} \tag{2.34}$$

where $\boldsymbol{M}$, $\boldsymbol{B}$, $\boldsymbol{C}$ is global mass, damping and stiffness matrix, respectively. $\boldsymbol{F}$ is the external force vector.

In order to obtain natural frequencies and eigenmodes, it is assumed that there is no external force, and ignore the damping term.Thus, the equation can be written as:

$$\boldsymbol{M}\ddot{\boldsymbol{d}} + \boldsymbol{C}\boldsymbol{d} = \boldsymbol{0} \tag{2.35}$$

Assume the displacement vector $\boldsymbol{d}$ as:

$$\boldsymbol{d} = \boldsymbol{d_0}\exp(i\boldsymbol{\omega}t) \tag{2.36}$$

Insert Eq(2.36) into Eq(2.35):

$$-\boldsymbol{M}\boldsymbol{\omega}^2\boldsymbol{d_0}\exp(i\boldsymbol{\omega}t) + \boldsymbol{C}\boldsymbol{d_0}\exp(i\boldsymbol{\omega}t) = \boldsymbol{0} \tag{2.37}$$

Then, the eigenfrequencies is:

$$\boldsymbol{\omega}^2 = eigs(\boldsymbol{C}/\boldsymbol{M}) \tag{2.38}$$

2.3.3   Modal Analysis

Modal analysis is another method in structural mechanics. The deformation variables are approximated by spatial functions and corresponding coordinates.

In the modal analysis, the stretch motion is ignored since the stretch deflection is small. The deformation variables are defined as follows:

$$v(x, t) = \sum_{i=1}^{\mu} \Phi_{1i}(x) q_i(t)$$

$$w(x, t) = \sum_{i=1}^{\mu} \Phi_{2i}(x) q_i(t) \tag{2.39}$$

$$\phi(x, t) = \sum_{i=1}^{\mu} \Phi_{3i}(x) q_i(t)$$

The equations of motions can be obtained from the Lagrange's equation:

$$\frac{d}{dt}\left(\frac{\partial T}{\partial \dot{q}_i}\right) - \frac{\partial T}{\partial q_i} + \frac{\partial \Pi}{\partial q_i} = \frac{\partial W}{\partial q_i} \tag{2.40}$$

Where Π is the total potential energy. T is the total kinetic energy. W is the work done by external force.

In the present work, two flapwise, two edgewise and one torsion mode shapes are used in the model analysis.

2.3.3.1   Time domain formulation

The global governing equation from modal analysis can be written in time domain as:

$$\boldsymbol{M}\ddot{\boldsymbol{q}} + \boldsymbol{B}\dot{\boldsymbol{q}} + \boldsymbol{K}\boldsymbol{q} = \boldsymbol{F} \tag{2.41}$$

where $\boldsymbol{M}, \boldsymbol{B}, \boldsymbol{K}$ are global modal mass, damping and stiffness matrices, respectively. $\boldsymbol{F}$ is external force vector, which changes in each time step.

The system of equations in Eq(2.41) are coupled second-order differential equations due to the pre-twist. The Newmark-β method is used to solve the equations, which is explained in Section 2.3.3.2.

2.3.3.2 Numerical Integration(Newmark-β method)

The governing equations are solved in time domain step by step. In general, explicit or implicit methods can be used for time integration. Explicit algorithms require a smaller time increment for stability, but the computation for each time step is more efficient. Implicit algorithms require more computational time per step, but fewer total steps[25].

In the present work, Newmark-β method is applied. The Newmark-β method is an implicit method.

The finite difference approximations for the Newmark-β method are:

$$\boldsymbol{q}_{i+1} \approx \boldsymbol{q}_i + \Delta t \dot{\boldsymbol{q}}_i + \Delta t^2 \left[\left(\frac{1}{2} - \beta \right) \ddot{\boldsymbol{q}}_i + \beta \ddot{\boldsymbol{q}}_{i+1} \right] \tag{2.42}$$

$$\dot{\boldsymbol{q}}_{i+1} \approx \dot{\boldsymbol{q}}_i + \Delta t \left[\left(1 - \gamma \right) \ddot{\boldsymbol{q}}_i + \gamma \ddot{\boldsymbol{q}}_{i+1} \right] \tag{2.43}$$

where γ and β are numerical factors.

Formulating the finite difference relationships in terms of the increments of the general coordinates:

$$\delta \ddot{\boldsymbol{q}}_i = \frac{1}{\beta \Delta t^2} \delta \boldsymbol{q}_i - \frac{1}{\beta \Delta t} \dot{\boldsymbol{q}}_i - \frac{1}{2\beta} \ddot{\boldsymbol{q}}_i \tag{2.44}$$

$$\delta \dot{\boldsymbol{q}}_i = \frac{\gamma}{\beta \Delta t} \delta \boldsymbol{q}_i - \frac{\gamma}{\beta} \dot{\boldsymbol{q}}_i - \Delta t \left(1 - \frac{\gamma}{2\beta} \right) \ddot{\boldsymbol{q}}_i \tag{2.45}$$

The increment of the general coordinates can be solved as:

$$(\boldsymbol{M} \frac{1}{\beta \Delta t^2} + \boldsymbol{B} \frac{\gamma}{\beta \Delta t} + \boldsymbol{K}) \delta \boldsymbol{q}_i = \delta \boldsymbol{F}_i + (\boldsymbol{M} \frac{1}{\beta \Delta t} + \boldsymbol{B} \frac{\gamma}{\beta}) \dot{\boldsymbol{q}}_i + \left[\boldsymbol{M} \frac{1}{2\beta} + \boldsymbol{B} \Delta t \left(1 - \frac{\gamma}{2\beta} \right) \right] \tag{2.46}$$

The general coordinates can be updated:

$$\begin{aligned} \boldsymbol{q}_{i+1} &= \boldsymbol{q}_i + \delta \boldsymbol{q}_i \\ \dot{\boldsymbol{q}}_{i+1} &= \dot{\boldsymbol{q}}_i + \delta \dot{\boldsymbol{q}}_i \\ \ddot{\boldsymbol{q}}_{i+1} &= \ddot{\boldsymbol{q}}_i + \delta \ddot{\boldsymbol{q}}_i \end{aligned} \tag{2.47}$$

In the present work, $\beta = 0.2564$ and $\gamma = 0.505$. And the time step is set to be $\Delta t = 0.1 s$.

Chapter 3

Flexible blade Model

In this chapter, the blade is modeled as a rotating cantilever beam. Euler-Bernoulli beam theory is applied. The strech, flapwise bending, edgewise bending and torsion are considered. The blade kinetic energy, potential energy are established for obtaining the equations of motion. Finite element method, in Section(3.7)-Section(3.8), and modal analysis in Section(3.9) are used to solve the blade structure dynamics.

3.1   Coordinate System

A local coordinate system xyz is defined. It rotates with the hub. The origin o is at the blade root, with x-axis along the blade before deformation. $\vec{i}, \vec{j}, \vec{k}$ denote the unit length in the x,y,z direction, respectively, as shown in Figure(3.1).

The length of blade is L, and the radius of the hub is defined as r. The hub is rotating about the axis of symmetry with a rotating speed Ω. Since only the deflection of the blade is analyzed, the cone angle and tilt angle can be set as zeros in order to simplify the calculation. And the hub is modelled as rigid.

The deformations of the blade in the directions of $\vec{i}, \vec{j}$ and $\vec{k}$ are generally described by the axial deformation u, the chordwise deformation v and the flapwise deformation w, respectively.
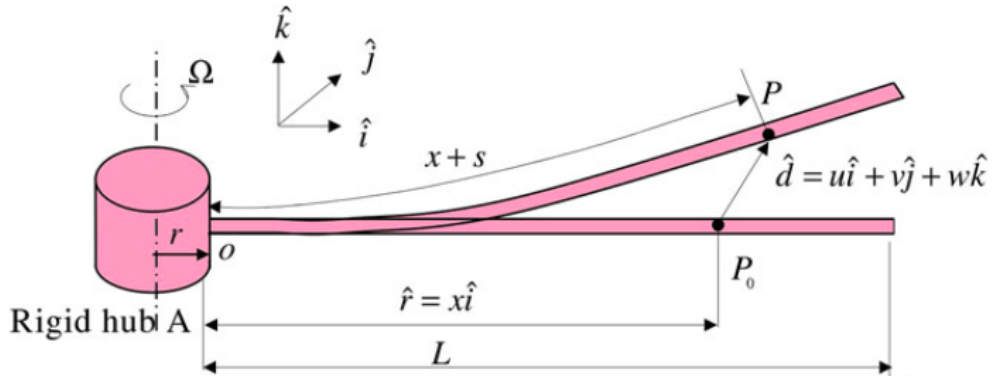
Figure 3.1: Illustration of a rotating cantilever beam[16]

3.2   Relation between stretch and deformation

Figure(3.2) shows the differential arc of the neutral axis of the beam. The total stretch length s of the neutral axis after deformation of the beam can be decomposed into axial deformation u, as well as the deformations caused by the chordwise and flapwise displacements.
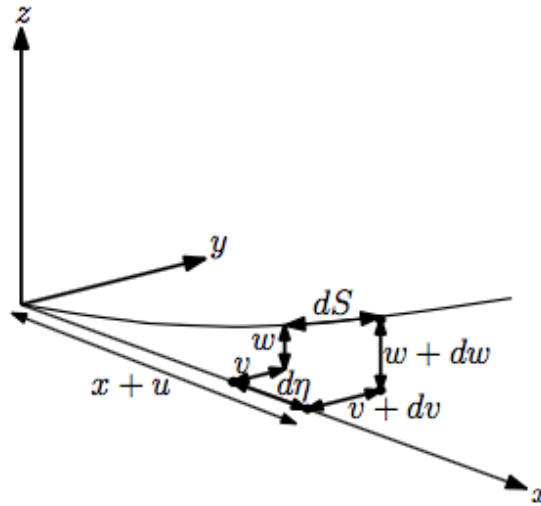
Figure 3.2: Differential arc of the neutral axis of the beam

According to reference[12], the relationship between stretch length s and deformation u,v,w can be writen as:

$$u = s - h_v - h_w \tag{3.1}$$

where

$$h_v = \frac{1}{2} \int_0^x (\frac{\partial v}{\partial \eta})^2 d\eta$$

$$h_w = \frac{1}{2} \int_0^x (\frac{\partial w}{\partial \eta})^2 d\eta$$

in which η is a dummy variable.

Differentiating Eq(3.1) with respect to x is:

$$\frac{\partial u}{\partial x} = \frac{\partial s}{\partial x} - \frac{1}{2}(\frac{\partial v}{\partial x})^2 - \frac{1}{2}(\frac{\partial w}{\partial x})^2 \tag{3.2}$$

3.3 Kinetic Energy

A point on the blade before and after deformation can be expressed at the local frame xyz as,

$$\vec{P}_0 = x\vec{i} \qquad \vec{P}_1 = (x+u)\vec{i} + v\vec{j} + w\vec{k} \tag{3.3}$$

The velocity of point P in the local coordinate can be derived as:

$$\vec{V}_P = \vec{V}_o + \frac{d\vec{P}_1}{dt} + \vec{\omega} \times \vec{P}_1 \tag{3.4}$$

where:

$$\vec{\omega} = \Omega \vec{k}$$

$$\vec{V}_o = r\Omega \vec{j}$$

Then,

$$\vec{V}_P = (\dot{u} - \Omega v)\vec{i} + (\dot{v} + \Omega(r + u + x))\vec{j} + \dot{w}\vec{k} \tag{3.5}$$

where the dots indicates the derivative with respect to time.

The kinetic energy can be expressed as:

$$T = \frac{1}{2}\rho A \int_0^L \vec{V}_P^T \vec{V}_P dx \tag{3.6}$$

Substitute u by Eq(3.1) to Eq(3.6). And since h_v and h_w are of high order $O(v^2)$. Thus, any product of these terms can be neglected. Applying the variational to the kinetic energy:

$$\delta T = \rho A \int_0^L \{ [\dot{s} - \Omega v] \frac{\partial}{\partial t} \delta s + [\dot{s} - \Omega v] \delta (-\Omega v)$$
$$+ [\dot{v} + \Omega(x + r + s)] \frac{\partial}{\partial t} \delta v + [\dot{v} + \Omega(x + r + s)] \delta(\Omega s) \qquad (3.7)$$
$$- \Omega^2 (x + r) \delta (h_v + h_w) + \dot{w} \frac{\partial}{\partial t} \delta w \} dx$$

According to reference[12], the term:

$$\int_0^L \left[\Omega^2 (x + r) \delta (h_v + h_w) \right] dx = \Omega^2 \int_0^L \frac{\partial}{\partial x} \left[(r(L - x) + \frac{1}{2}(L^2 - x^2)) \frac{\partial v}{\partial x} \right] \delta v$$
$$+ \frac{\partial}{\partial x} \left[(r(L - x) + \frac{1}{2}(L^2 - x^2)) \frac{\partial w}{\partial x} \right] \delta w dx$$

3.4 Potential Energy

For a blade, the cross sections are pre-twisted, the product of inertia need to be accounted for the potential energies. The strain energy for the Euler-Bernoulli Beam, should be expressed as:

$$\Pi = \frac{1}{2} \int_0^L \left\{ EA(\frac{\partial s}{\partial x})^2 + EI_z(\frac{\partial^2 v}{\partial x^2})^2 + EI_y(\frac{\partial^2 w}{\partial x^2})^2 + 2EI_{yz}(\frac{\partial^2 v}{\partial x^2})(\frac{\partial^2 w}{\partial x^2}) + GJ(\frac{\partial \phi}{\partial x})^2 \right\} dx \qquad (3.8)$$

In order to estimate the moments of inertia and the product of inertia, it is assumed the cross section is rectangular. Denate the principal moments as EI_1 for the flapwise, and EI_2 for the chordwise. And the twist angle is β. Then the moments of inertia and the product of inertia are:

$$EI_y = EI_2 \sin^2(\beta) + EI_1 \cos^2(\beta) \quad \text{chordwise}$$
$$EI_z = EI_2 \cos^2(\beta) + EI_1 \sin^2(\beta) \quad \text{flapwise} \qquad (3.9)$$
$$EI_{yz} = (EI_2 - EI_1) \sin(\beta) \cos(\beta)$$

Applying the variational to the potential energy yields:

$$\delta\Pi = \int_0^L \{EA\frac{\partial s}{\partial x}\frac{\partial}{\partial x}\delta s + EI_z\frac{\partial^2 v}{\partial x^2}\frac{\partial^2}{\partial x^2}\delta v + EI_y\frac{\partial^2 w}{\partial x^2}\frac{\partial^2}{\partial x^2}\delta w$$
$$+ EI_{yz}(\frac{\partial^2}{\partial x^2})\delta v(\frac{\partial^2 w}{\partial x^2}) + EI_{yz}(\frac{\partial^2 v}{\partial x^2})(\frac{\partial^2}{\partial x^2})\delta w + GJ\frac{\partial\phi}{\partial x}\frac{\partial}{\partial x}\delta\phi\}dx \tag{3.10}$$

After the integration by parts, Eq(3.10) can be writen as:

$$\delta\Pi = \int_0^L \{-EA\frac{\partial^2 s}{\partial x^2}\delta s + EI_z\frac{\partial^4 v}{\partial x^4}\delta v + EI_y\frac{\partial^4 w}{\partial x^4}\delta w+$$
$$EI_{yz}\frac{\partial^4 w}{\partial x^4}\delta v + EI_{yz}\frac{\partial^4 v}{\partial x^4}\delta w - GJ\frac{\partial^2\phi}{\partial x^2}\delta\phi\}dx \tag{3.11}$$

3.5   Work due to external force

In the present work, the gravity is ignored. The work done by the external force can be expressed as:

$$W = \int_0^L \Big[f_v(x,t)v + f_w(x,t)w + M_\phi(x,t)\phi\Big]dx \tag{3.12}$$

where:

f_v is chordwise load per unit length;

f_w is flapwise load per unit length;

M_ϕ is torsion load per unit length;

3.6   Equations of Motion

Apply Hamilton's principle, then collect all the terms of the integrand with respect to δs, δv, δw and $\delta\phi$ the coefficients can lead to equations of motion.

$$\int_{t_1}^{t_2} (\delta T - \delta\Pi + \delta W)\,dt = 0 \tag{3.13}$$

$$\int_{t_1}^{t2} \delta\Pi dt = E\int_0^L \int_{t_1}^{t2} \left\{-A\frac{\partial^2 s}{\partial x^2}\delta s + I_z\frac{\partial^4 v}{\partial x^4}\delta v + I_y\frac{\partial^4 w}{\partial x^4}\delta w + I_{yz}\frac{\partial^4 w}{\partial x^4}\delta v + I_{yz}\frac{\partial^4 v}{\partial x^4}\delta w\right\}dtdx$$

$$\int_{t_1}^{t_2} \delta W dt = \int_0^L \int_{t_1}^{t_2} \left[f_v \delta v + f_w \delta w + M_\phi \phi \right] dt dx$$

Therefore, the equations of motion is derived as:

Stretch motion

$$\rho A \left(\frac{\partial^2 s}{\partial t^2} - 2\Omega \frac{\partial v}{\partial t} - \Omega^2 s \right) - EA \frac{\partial^2 s}{\partial x^2} = \rho A \Omega^2 (r + x) \tag{3.14}$$

Chordwise motion

$$\rho A \left(\frac{\partial^2 v}{\partial t^2} + 2\Omega \frac{\partial s}{\partial t} - \Omega^2 v \right) + EI_z \frac{\partial^4 v}{\partial x^4} + EI_{yz} \frac{\partial^4 w}{\partial x^4} - \Omega^2 \rho A \frac{\partial}{\partial x} \left[\left(r(L-x) + \frac{1}{2}(L^2 - x^2) \right) \frac{\partial v}{\partial x} \right] = f_v \tag{3.15}$$

Flapwise motion

$$\rho A \frac{\partial^2 w}{\partial t^2} + EI_y \frac{\partial^4 w}{\partial x^4} + EI_{yz} \frac{\partial^4 v}{\partial x^4} - \Omega^2 \rho A \frac{\partial}{\partial x} \left[\left(r(L-x) + \frac{1}{2}(L^2 - x^2) \right) \frac{\partial w}{\partial x} \right] = f_w \tag{3.16}$$

Torsion motion

$$\rho J \frac{\partial^2 \phi}{\partial t^2} - GJ \frac{\partial^2 \phi}{\partial x^2} = M_\phi \tag{3.17}$$

Boundary conditions

The boundary condition can be expressed as:

$$\phi = s = v = w = \frac{\partial v}{\partial x} = \frac{\partial w}{\partial x} = 0 \quad \text{at} \quad x = 0$$

$$\frac{\partial \phi}{\partial x} = \frac{\partial s}{\partial x} = \frac{\partial^2 v}{\partial x^2} = \frac{\partial^2 w}{\partial x^2} = \frac{\partial^3 v}{\partial x^3} = \frac{\partial^3 w}{\partial x^3} = 0 \quad \text{at} \quad x = L \tag{3.18}$$

3.7 Element matrix
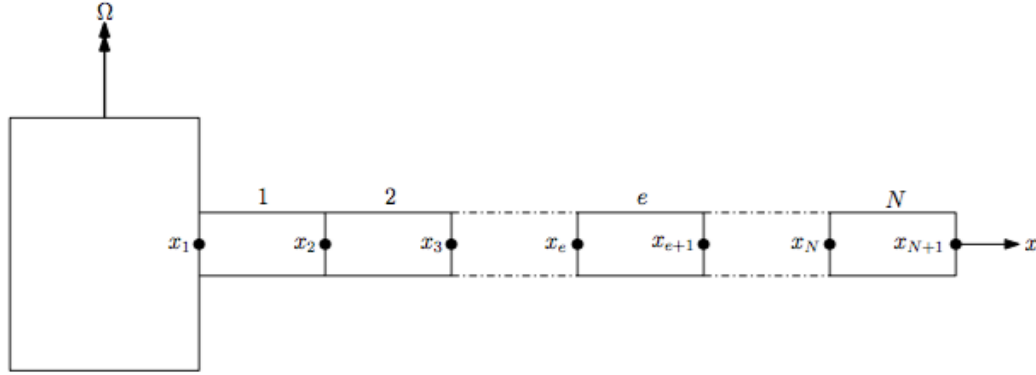
Figure 3.3: Discretization of the beam in finite elements

It can be seen that Equations of motion Eq(3.14), Eq(3.15) and Eq(3.16) are coupled. In order to solve these differential equations by finite element method, the discretization of the beam is shown in Figure(3.3).The number of nodes is denoted as $N+1$, while the number of elements is N. The element e defined by node numbers e and $e+1$.

The shape functions are defined Hermite interpolation functions. The stretch and torsion deformations are approximated as linear polynomials. And the chordwise and flapwise deformations have to be cubic in order to yield non zero shear force($\frac{\partial^3 v}{\partial x^3}$). The shape functions are expressed as: $\mathbf{N_s}$, $\mathbf{N_\phi}$ $\mathbf{N_v}$ $\mathbf{N_w}$, for stretch, torsion, chordwise deflection and flapwise deflection, respectively, which are shown in Appendix A.

A solution of the Finite element method, an approximate solution, is obtained in a finite dimensional function space. In order to find approximate solutions of Equation(3.14) to Equation(3.17), the weak forms are discretized by using the two-node beam elements defined above. The discretized equations of motion are:

$$\sum_{e=1}^{N} (\eta_e)^T \left\{ \mathbf{m_e}\ddot{\mathbf{d}}_\mathbf{e} + 2\Omega\mathbf{g_e}\dot{\mathbf{d}}_\mathbf{e} + \left[\mathbf{k_e} + \Omega^2(\mathbf{s_e} - \mathbf{c_e}) \right] \mathbf{d_e} \right\} = \sum_{e=1}^{N} (\eta_e)^T \mathbf{f_e} \qquad (3.19)$$

where $\mathbf{m_e}$, $\mathbf{g_e}$, $\mathbf{k_e}$ and $\mathbf{s_e}$ are the element mass, the element gyroscopic, the element stiffness and the element motion-induced stiffness matrices. And $\mathbf{d_e}$ the element deformation vector.

The element matrices are given is Appendix A.

3.8 Global matrix

Since $\eta_{\mathbf{e}}$ are arbitrary vectors, by assembling the element matrices and vectors, Equation(A.5) can be transformed to the global equation. The global equation is expressed as:

$$\mathbf{M}\ddot{\mathbf{d}} + 2\Omega\mathbf{G}\dot{\mathbf{d}} + \left[\mathbf{K} + \Omega^2(\mathbf{S} - \mathbf{C})\right]\mathbf{d} = \mathbf{f} \tag{3.20}$$

where $\mathbf{d}$ is the global deformation matrix:

$$\mathbf{d} = \left\{s_1, \phi_1, v_1, \theta_1, w_1, \psi_1, ..., s_N, \phi_N, v_N, \theta_N, w_N, \psi_N\right\}^T$$

$$\mathbf{M} = \mathbf{A}_{e=1}^N \mathbf{m_e} \quad \mathbf{G} = \mathbf{A}_{e=1}^N \mathbf{g_e} \quad \mathbf{K} = \mathbf{A}_{e=1}^N \mathbf{k_e} \quad \mathbf{S} = \mathbf{A}_{e=1}^N \mathbf{s_e} \quad \mathbf{C} = \mathbf{A}_{e=1}^N \mathbf{c_e} \quad \mathbf{f} = \mathbf{A}_{e=1}^N \mathbf{f_e}$$

where $\mathbf{A}$ denotes the assembly operator.

3.9 Modal Method

The equations of motion Eq(3.14)-Eq(3.17) can also be solved by modal method. The FAST code is based on modal theory, which gives linear structural response. In the present work, the modal shapes are determined by finite element method as shown above. Then, modal method is applied on time domain since it is reasonably accurate and computationally efficient in normal load cases.

Since the stretch deformation is limited, it is ignored in modal analysis in order to simplify the computation.

The deformation variables are approximated as follows:

$$v(x,t) = \sum_{i=1}^{\mu_1} \Phi_{1i}(x) q_{1i}(t)$$

$$w(x,t) = \sum_{i=1}^{\mu_2} \Phi_{2i}(x) q_{2i}(t) \tag{3.21}$$

$$\phi(x,t) = \sum_{i=1}^{\mu_3} \Phi_{3i}(x) q_{3i}(t)$$

Introduce Eq(3.21) into kinetic energy T Eq(3.6), then take partial derivatives of T with re-

spect to q_{1i} and q_{2i} and neglect the higher order nonlinear terms. The q_{2i} eqations are the same to q_{1i}'s, but with modal shape Φ_{2i} and general coordinate q_{2i}.

$$\frac{\partial T}{\partial q_{1i}} = \Omega^2 \sum_{j=1}^{\mu_1} \int_0^L EI_z \Phi_{1i} \Phi_{1j} q_{1j} dx - \Omega^2 \left[\sum_{j=1}^{\mu_1} \int_0^L \rho A \left(r(L-x) + \frac{1}{2}(L^2 - x^2) \right) \Phi'_{1i} \Phi'_{1j} q_{1j} dx \right] \quad (3.22)$$

$$\frac{d}{dt} \left(\frac{\partial T}{\partial \dot{q}_{1i}} \right) = \sum_{j=1}^{\mu_1} \int_0^L \rho A \Phi_{1i} \Phi_{1j} \ddot{q}_{1j} dx \quad (3.23)$$

Introduce Eq(3.21) into the potential energy Π Eq(3.8), then take partial derivatives of the potential energy with respect to q:

$$\frac{\partial \Pi}{\partial q_{1i}} = EI_z \sum_{j=1}^{\mu_1} \int_0^L \Phi''_{1i} \Phi''_{1j} q_{1j} dx + EI_{yz} \sum_{j=1}^{\mu_1} \int_0^L \Phi''_{1i} \Phi''_{2j} q_{2j} dx \quad (3.24)$$

$$\frac{\partial \Pi}{\partial q_{2i}} = EI_y \sum_{j=1}^{\mu_2} \int_0^L \Phi''_{2i} \Phi''_{2j} q_{2j} dx + EI_{yz} \sum_{j=1}^{\mu_2} \int_0^L \Phi''_{2i} \Phi''_{1j} q_{1j} dx \quad (3.25)$$

Introduce Eq(3.21) into the external work W Eq(3.12), then:

$$\frac{\partial W}{\partial q_{1i}} = \sum_{j=1}^{\mu_1} \int_0^L f_v \Phi_{1i} q_{1i} dx \quad (3.26)$$

$$\frac{\partial W}{\partial q_{2i}} = \sum_{j=1}^{\mu_2} \int_0^L f_w \Phi_{2i} q_{2i} dx \quad (3.27)$$

According to the Lagrange's equations of motion:

$$\frac{d}{dt} \left(\frac{\partial T}{\partial \dot{q}_i} \right) - \frac{\partial T}{\partial q_i} + \frac{\partial \Pi}{\partial q_i} = \frac{\partial W}{\partial q_i} \quad (3.28)$$

The equations of motion can be written as:

$$\mathbf{M}\ddot{\mathbf{q}} + 2\xi\omega_{\mathbf{n}}\dot{\mathbf{q}} + \mathbf{K}\mathbf{q} = \mathbf{F} \quad (3.29)$$

where ξ is the structural-damping ratio. Based on Reference[24], $\xi = 0.477465\%$ for the NREL 5MW blades. The modal shapes are obtained from finite element analysis using curve fitting.

The elements in mass and stiffness matrix are calculated and presented in Appendix B.

3.10   Blade eigenfrequency and eigenmodes

The natural frequencies calculated from FEM is shown in Table(3.1). Results from BModes are included for comparison.

Table(3.1) shows that the presented flexible blade model solved by FEM has high consistence with the results from Bmodes.

Table 3.1: Blade eigenfrequencies as computed from the presented FEM and compared to BModes (50 modes)[26]

	0rmp			12.1rmp		
	presented FEM[Hz]	Bmodes[Hz]	diff.	FEM[Hz]	Bmodes[Hz]	diff.
1st flapwise	0.677	0.683	-0.88%	0.764	0.734	4.09%
1st edgewise	1.086	1.089	-0.28%	1.117	1.098	1.73%
2st flapwise	1.954	1.958	-0.20%	2.051	2.017	1.69%
2st edgewise	4.007	4.008	-0.03%	4.049	4.030	0.47%
3st flapwise	4.560	4.541	0.42%	4.653	4.595	1.26%
1st torsion	5.575	5.550	0.45%	5.575	5.550	0.45%
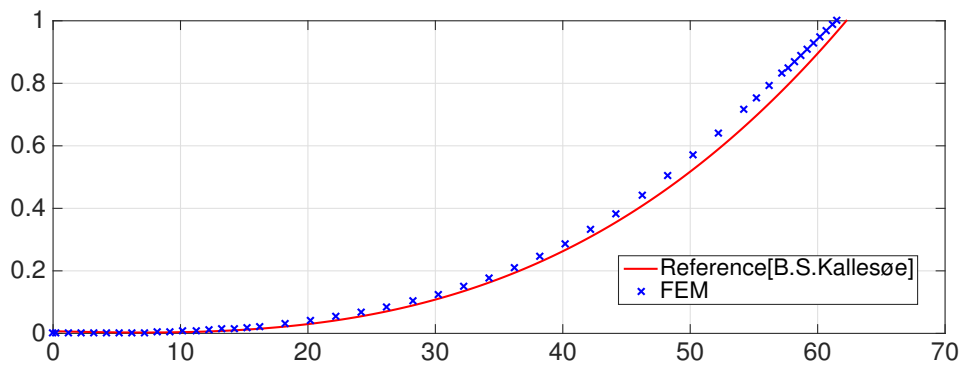
Figure 3.4: The first flapwise eigenmodes at $\Omega = 0 \text{rad/s}$ compared to Ref[27]
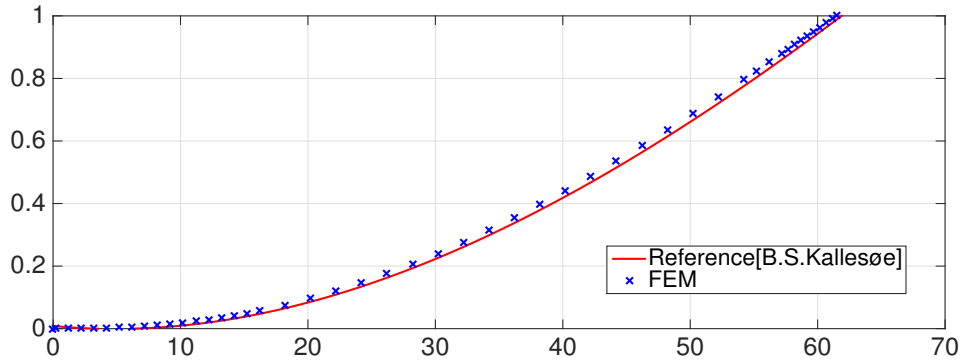
Figure 3.5: The first edgewise eigenmodes at $\Omega = 0$ rad/s compared to Ref[27]
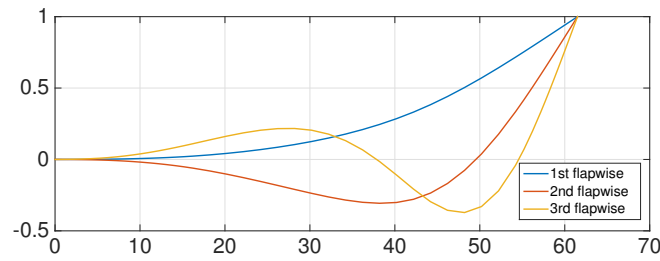
Figure 3.6: 1st,2nd and 3rd flapwise eigenmodes from finite element method
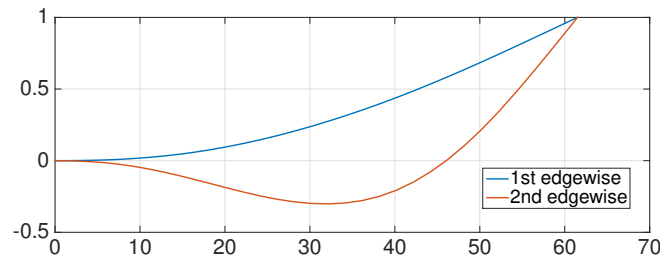
Figure 3.7: 1st and 2nd edgewise eigenmodes from finite element method
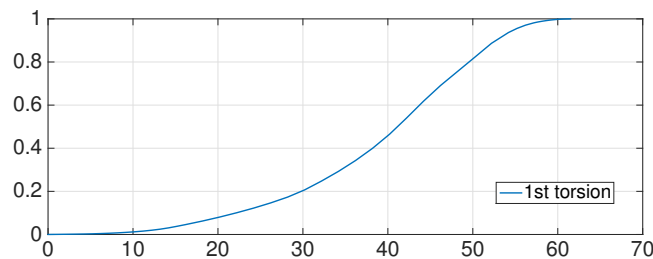
Figure 3.8: 1st torsion eigenmodes from finite element method

It can be seen that the natural frequencies obtained from finite element method have good agreement with the results based on simulation tools and the variation is within 1.0 % for non rotating blade. For blades rotating at the rated speed, the 1st flapwise mode has relative large variation, around 4.0%. The rotation speed strengthens the beam and results in higher natural frequencies. Since while the blade is rotating, centrifugal force can be considered as a tensile force, the stiffness of the blade increases.

The mode shapes are also compared to Reference[27] as shown in Figure(3.4) and Figure(3.5), which shows high consistence.

Chapter 4

Couple blade model with AeroDyn

In order to calculate the aerodynamics loads, the flexible and rigid blade models are coupled with code AeroDyn. An interface between the structure model and AeroDyn was written using FORTRAN. The positions, velocities and orientations for each blade element should be defined at each time step. The resulting forces calculted by the AeroDyn should be decomposed to the out-of-rotate plane and in-rotate plane for integration.

In addition, an external control system applies the generator torque according to a look-up table and blade pitch commands via PI control.

4.1   Baseline wind turbine

In the present work, NREL offshore 5-MW baseline wind turbine developed by National Renewable Energy Laboratory [24] is used. NREL offshore 5-MW baseline wind turbine is a conventional three-bladed upwind variable-speed variable blade-pitch-to-feather-controlled turbine. The main properties are shown in Table(4.1). The rotor diameter and hub height dimensions are 126.0m and 90.0m above the still water line (SWL), respectively. The blade is divided into 17 elements. And eight unique airfoil-data tables for the NREL offshore 5-MW baseline wind turbine are defined, which provides the two- dimensional airfoil-data coefficients.

Table(4.2) shows the aerodynamic models used in this study. The blade element theory is applied with some corrections.

Table 4.1: NREL 5MW baseline turbine specifications

Rated power	5MW
Rotor orientation	Upwind
Rotor configuration	3 blades, 61.5m length
Rotor, hub diameter	126m,3m
Hub height	90m
Cut-In, Rated, Cut-Out Wind Speed	3 m/s, 11.4 m/s, 25 m/s
Cut-In, Rated Rotor Speed	6.9 rpm, 12.1 rpm
Rated Tip Speed	80m/s
Overhang, Shaft Tilt, Precone	5m, 5°, -2.5^o
Rotor Mass	110,000 kg
Nacelle Mass	240,000 kg

Table 4.2: Aerodynamic models used in Aerodyn calculation

dynamic stall	Beddoes-Leishman model
dynamic inflow	BEM theory
tip-loss correction	Prandtl tip loss model
hub-loss correction	Prandtl hub loss model

4.2 Coordinate system

Global reference frame

The global X,Y,Z reference frame is fixed to the undeflected tower center line. The X axis is pointing in the downwind (zero degree wind) direction, the Y axis is pointing to the left looking along the positive X axis, and the Z axis is pointing vertically upward opposite gravity along the centerline of the undeflected tower. The unit length in XYZ direction is defined as $\vec{I}$, $\vec{J}$, $\vec{K}$.

Shaft reference frame

The shaft reference frame is defined at the apex of rotation. x axis is pointing along the shaft. It

can be considered as a frame which has a tilt angle for the global coordinate system.

It should be noted that the up tilt angle is defined as positive, which increases the hub height.

Hub reference frame

The hub coordinate system is located at the apex of rotation, as shown in Figure(4.1). x axis is pointing along the hub center line in the nominally downwind direction. And z axis is perpendicular to the hub center line with the same azimuth as Blade 1.

Hub reference defined in AeroDyn

Blade reference defined in AeroDyn
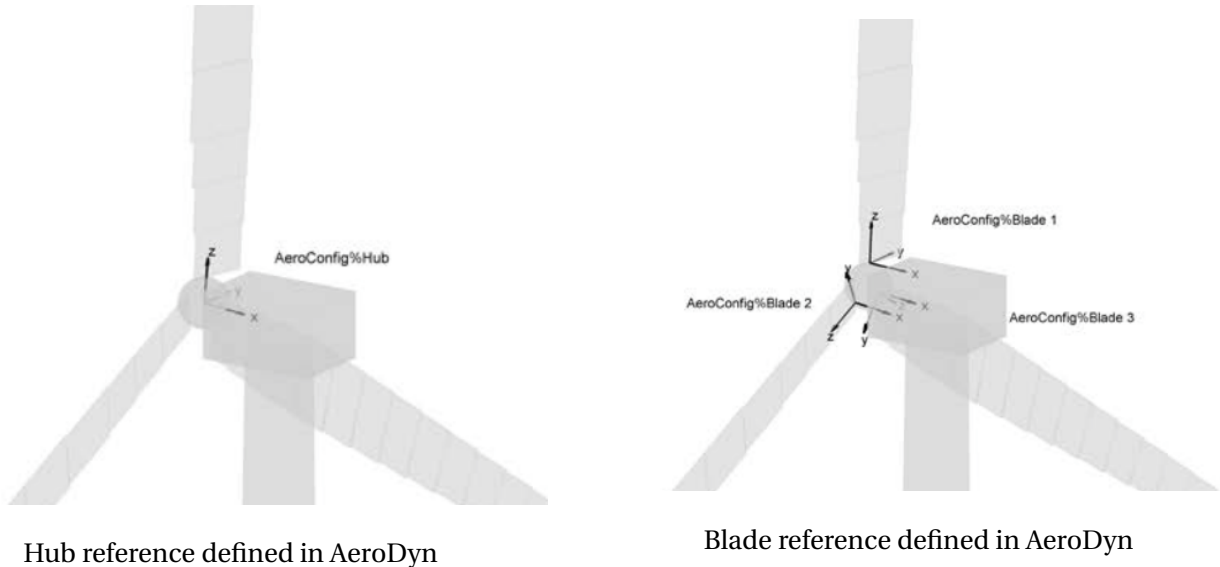
Figure 4.1: AeroDyn coordinate definition[28]

Blade reference frame

The blade reference system is rotating along the shaft. And the origin is at the blade root. x axis is pointing to suction side.y axis is pointing towards the trailing edge of the blade. And z axis is along the pitch axis towards the tip of the blade, as shown in Figure(4.1).The blade reference should also include the coned angle. And the blade reference should be updated for each calculation step.

Blade element reference frame

The blade is divided into several elements. Each element pitches and deflects with the blades. Blade element reference is located at the center of each element. And their orientations are the same as blade's.

4.3   Coordinate transformation

The position and velocity should be defined related to the global X,Y,Z reference frame. Thus, the coordinate transformation from local references to the global frame is needed.

For the directions of shaft, the tilt angle should be considered with respect to the global frame.

$$
\begin{bmatrix} \vec{i}_s \\ \vec{j}_s \\ \vec{k}_s \end{bmatrix} = \mathbf{T}_{\alpha_t} \begin{bmatrix} \vec{I} \\ \vec{J} \\ \vec{K} \end{bmatrix}
\tag{4.1}
$$

where $\vec{i}_s$, $\vec{j}_s$, $\vec{k}_s$ is the unit length of the shaft reference, and the tile angle is denoted as α_t.

The hub reference can be obtained by rotating the shaft frame with an azimuth angle of blade 1.

$$
\begin{bmatrix} \vec{i}_h \\ \vec{j}_h \\ \vec{k}_h \end{bmatrix} = \mathbf{T}_{\alpha_t} \mathbf{T}_{\mathbf{azim}} \begin{bmatrix} \vec{I} \\ \vec{J} \\ \vec{K} \end{bmatrix}
\tag{4.2}
$$

where $\vec{i}_h$, $\vec{j}_h$, $\vec{k}_h$ is the unit length for hub reference.

The blade frame should also consider the transformation due to the cone angle α_c and the pitch angle α_p. Three blades are equally distributed, with an angle of $2\pi/3$. The azimuth for Blade 1 is φ, for Blade 2 is $\varphi + 2\pi/3$ and for Blade 3 is $\varphi + 4\pi/3$. And $\vec{i}_b$, $\vec{j}_b$, $\vec{k}_b$ is the unit length for blade reference.

$$
\begin{bmatrix} \vec{i}_b \\ \vec{j}_b \\ \vec{k}_b \end{bmatrix} = \mathbf{T}_{\alpha_t} \mathbf{T}_{\mathbf{azim}} \mathbf{T_c} \mathbf{T_p} \begin{bmatrix} \vec{I} \\ \vec{J} \\ \vec{K} \end{bmatrix}
\tag{4.3}
$$

Blade twist should be considered for blade elements. The twist angle is denoted as β. Then, $\vec{i}_{ele}$, $\vec{j}_{ele}$, $\vec{k}_{ele}$ can be donated as:

$$
\begin{bmatrix} \vec{i}_{ele} \\ \vec{j}_{ele} \\ \vec{k}_{ele} \end{bmatrix} = \mathbf{T}_{\alpha_t} \mathbf{T}_{\mathbf{azim}} \mathbf{T_c} \mathbf{T_p} \mathbf{T}_\beta \begin{bmatrix} \vec{I} \\ \vec{J} \\ \vec{K} \end{bmatrix}
\tag{4.4}
$$

The transformation matrices are provided in Appendix C. Figure(4.2) shows the positions and velocities of the blade elements at a certain time step. It can be seen that the rigid blade keeps the straight while the flexible one has included some deflections.
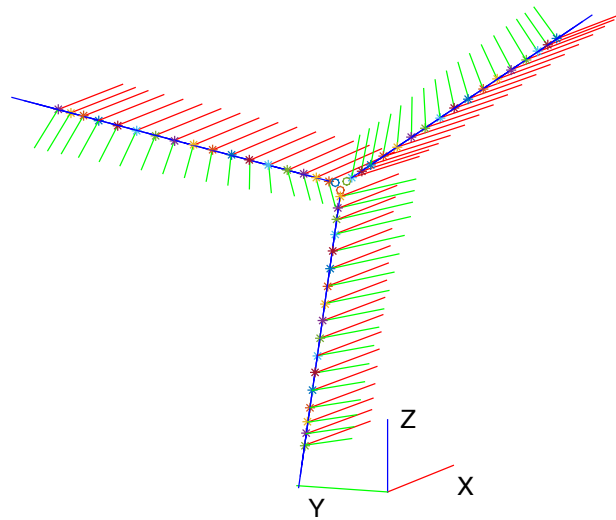
Rigid blades
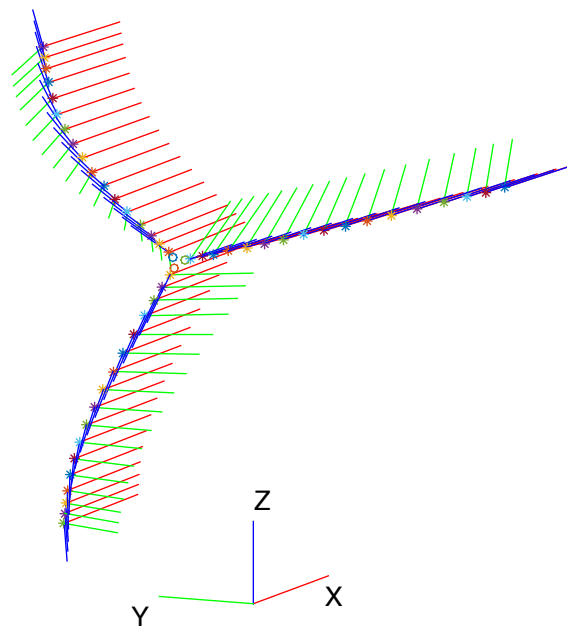
Flexible blades

Figure 4.2: Illustration of the rigid and flexible blade element positions and orientations definition in a certain time step

Chapter 5

Steady-state responses of rotor

The steady-state responses of rigid and flexible rotor model were obtained by running a series of simulations with steady and uniform wind speeds.

The effective simulation time is 10 minutes to make sure a steady-state has been reached. The simulation results were compared to results from FAST.

The differences between FAST and presented models are listed:

- In FAST, the NREL 5MW wind turbine is located in a land-based tower, but no support structure is included in this stage for the steady-state response of the presented models;

- Different pitch controller used in FAST and presented models. The detail is in Section(2.2.3);

- FAST only considers the flapwise bending and edgewise bending in the blade structure dynamics, while the flexible rotor model in this work also includes the torsional deflection.

In general, results from the rigid blade model and flexible blade model are in good agreement with the results in FAST.

In below-rated region, the pitch controller is inactive. The rigid blade and the flexible blade have the same pitch angle(0°). In this case, the rigid blade model has a slightly higher thrust force when compared to the flexible one. From a conservation of energy point of view, a part of energy in the incoming wind becomes the potential energy in the blade due to blade deformation, so it is expected the rigid blade has higher thrust force.

In above-rated region, the pitch controller is active. It can be seen that the flexible blade has a sightly lower pitch angle than the rigid one. In order to explain this phenomenon, one can

first assume that the pitch controller does not work, thus, the flexible blade should have a lower thrust force and aerodynamic torque due to the increased potential energy on blades. However, in above-rated region, a constant and rated power is expected. Therefore, the flexible blade has a relatively lower pitch angle to maintain the rated power.

Table 5.1: Some calculated data for steady-state response for comparison

	Rigid blade model			Flexible blade model		
U[m/s]	BlPitch[deg]	RotThrust[kN]	RotTorq	BlPitch[deg]	RotThrust[kN]	RotTorq
8	0	376.4	1960.2	0	370.6	1959.0
11	0	682.9	3892.6	0	662.1	3860.1
12	4.07	576.5	4180	3.61	578.6	4180
18	14.85	350.2	4180	14.48	351.6	4180

Table 5.2: Definition of output parameters

|		
RotTorq	the mechanical torque in the low-speed shaft	[kNm]
RotThrust	the rotor thrust	[kN]
GenSpeed	the rotational speed of the generator(high-speed shaft)	[rpm]
GenPwr	the electrical output of the generator	[kW]
RotSpeed	the rotational speed of the rotor(low-speed shaft)	[rpm]
GenTq	the electrical torque of the generator	[kNm]
BlPitch1	the pitch angle of Blade 1	[deg]
OoPDefl1	the out-of-plane and deflections of Blade 1	[m]
IPDefl1	the in-plane and deflections of Blade 1	[m]
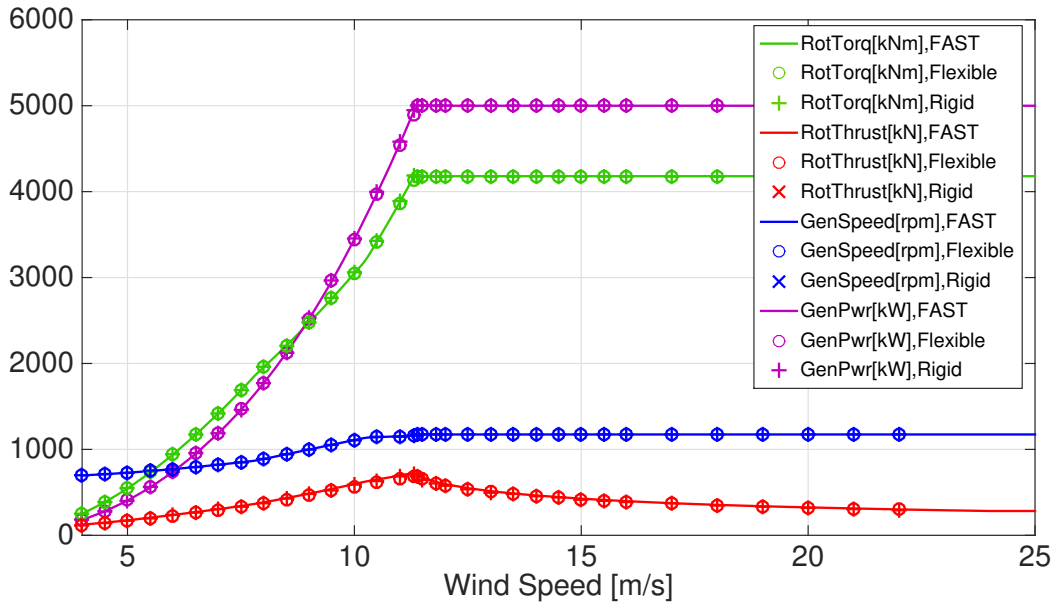
Figure 5.1: Wind turbine responses as function of wind speed.Comparison of FAST, flexible rotor model and rigid rotor model.
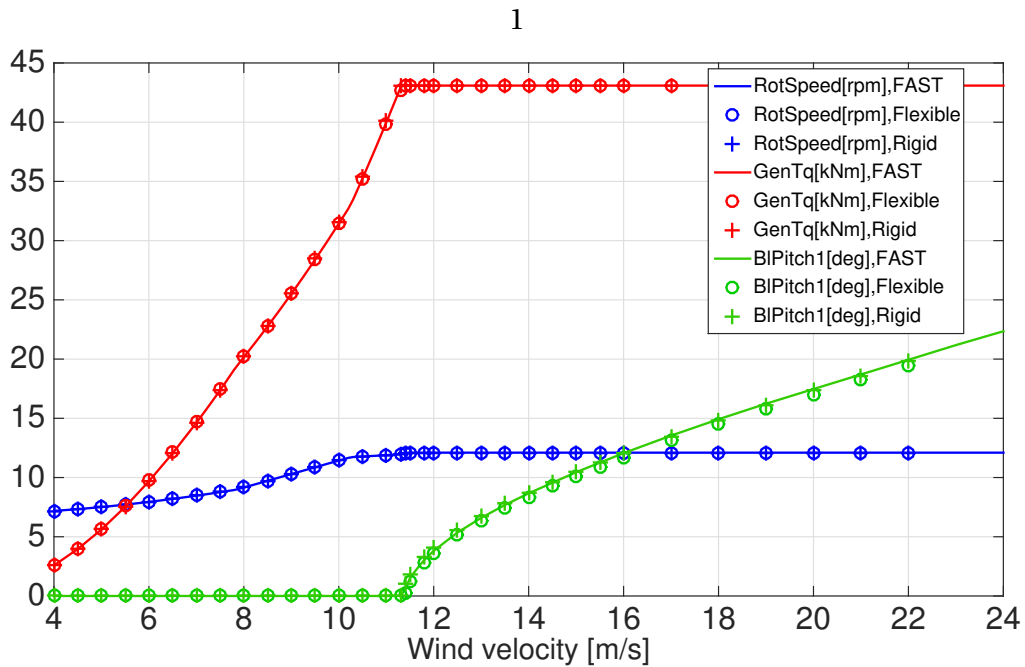

Figure 5.2: Wind turbine responses as function of wind speed.Comparison of FAST, flexible rotor model and rigid rotor model.
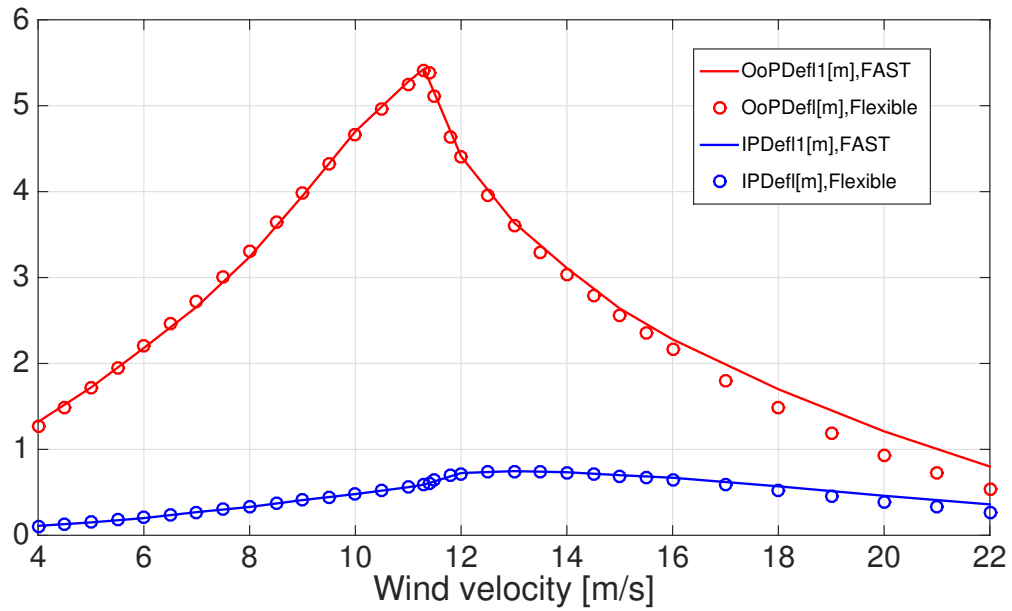
Figure 5.3: Wind turbine responses as function of wind speed.Comparison of FAST, flexible rotor model and rigid rotor model.

Chapter 6

Emulated Real-time Hybrid Model Test

For the 2015 NOWITECH ReaTHM test, a physical model(semi-submersible floater, tower and mooring lines) was established. In this study, an emulated ReaTHM test is carried out, which allows detecting potential errors in the allocation procedure, improving safety procedures, and running sensitivity studies on the time step used in the numerical model[7].

In the emulated ReaTHM testing, the 'physical' model is established in SIMO-RIFLEX, which is refered as 'emulated physical model' in the present work. The emulated physical model contains 5MW semi-submersible platform [8], tower, mooring lines and the mass of the turbine. It should be noted that the emulated physical model is in full scale, while in the 2015 NOWITECH ReaTHM test the model is in 1:30 scale.

The simulated position and velocity of the nacelle are passed and input to the modified Aero-Dyn code, and the aerodynamic forces are applied on the emulated physical model through a dynamic link library(DLL). The emulated ReaTHM test setup is described in detail in Section(6.1). The computational efficiency is discussed in Section(6.2). In Section(6.3), decay tests are performed to verify the reliability of the model. And in Section(6.4), the emulated ReaTHM test is verified in the irregular wave and turbulent wind load cases.

In this study, the emulated ReaTHM test with the rigid blade is referred as ReaTHM(R), and the test with the flexible blade is denoted as ReaTHM(F), for convenience.

6.1 Emulated ReaTHM Test Setup

6.1.1 Semi-submersible platform and coordinate system

Figure(6.1) shows the semi-submersible platform layout. The semi-submersible floater is composed of a central column which supports the tower and the wind turbine, three side columns and three pontoons[8]. Table(6.1) presents the main properties of the platform (excluding the wind turbine). The wind turbine is removed, but the mass of turbine is added to the nacelle in order to maintain the mass property of the whole system. In addition, the inertia of rotor is also estimated and added to the nacelle's inertia.

The global coordinate system is located at the centerline of the tower at the waterline. As shown in Figure(6.1), the x axis of the global coordinate system is pointing in the nominally downwind direction, and the z axis points upwards. The y axis is orthogonal with the x and z axis such that they form a right-handed coordinate system.

In this thesis, only aligned wind and wave is considered. The wave is coming along the x-axis, and the wind turbine also faces the x-axis.
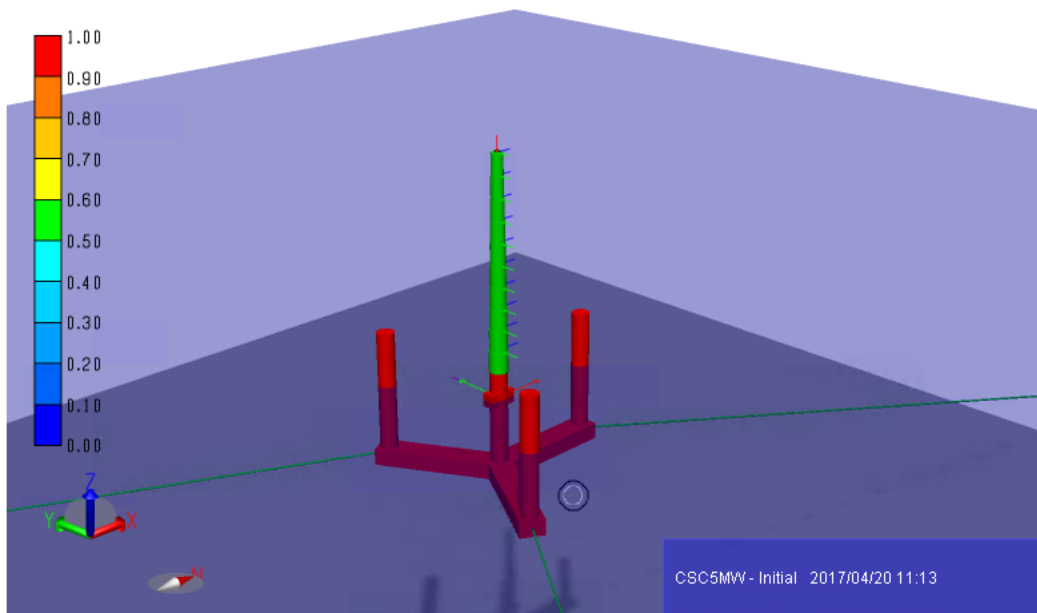

Figure 6.1: View of SIMA model and global coordinate system

Table 6.1: 5MW CSC Semi-submersible platform properties

COG(include tower and turbines)[m]	(0,0,-24.5)
Draft[m]	30
Freeboard[m]	20
Distance from center column midpoint to pontoon edge[m]	45.5
Pontoon height[m]	6
Pontoon width[m]	9
Diameter of center and offset columns[m]	6.5
Water depth[m]	200
Anchor point radius[m]	884.3
Natural frequency(include wind turbine)	
Surge[s]	83.5
Sway[s]	83.5
Heave[s]	25.3
Roll[s]	31.1
Pitch[s]	31.1
Yaw[s]	62.7

6.1.2 Frequencies of Interest

In the present study, the quantities of interest are the platform motions, the mooring lines tension and the forces at the tower/floater interface. The frequency content should be determined to correctly capture the quantities of interest.

Figure(6.2) shows the frequency content of interest. The natural frequencies for the platform motions are below the wave spectrum. Since the waves have a significant amount of energy, they will also have large effect on the quantities of interest. The first tower bending mode is also investigated in this study. The tower bending mode is at around 0.5Hz, which is coupled with three times of the rotational speed of the rotor(3P). Thus, the frequency of interest is decided to be 0-0.7Hz.

For the 2015 NOWITECH ReaTHM tests, a 1:30($\lambda = 30$) Froude scaling semi-submersible model was established. Under this scaling, the natural periods are scaled under $1/\sqrt{\lambda}$:

$$T_m = 1/\sqrt{\lambda} T_f \qquad (6.1)$$

Table(6.2) summarizes the scaled natural periods. Figure(6.3) shows the frequencies of interest for the 1:30 scaled model. It should be noted that during the 2015 ReaTHM testing in MARIN-TEK, 3P frequency was not included since the tower beding modes were out of the scope of the investigation.

Table 6.2: Semi-submersible FWT's natural frequency under the Froude scaling

	full model value	scaled value
Surge[s]	83.5	15.2
Sway[s]	83.5	15.2
Heave[s]	25.3	4.6
Roll[s]	31.1	5.7
Pitch[s]	31.1	5.7
Yaw[s]	62.7	11.4
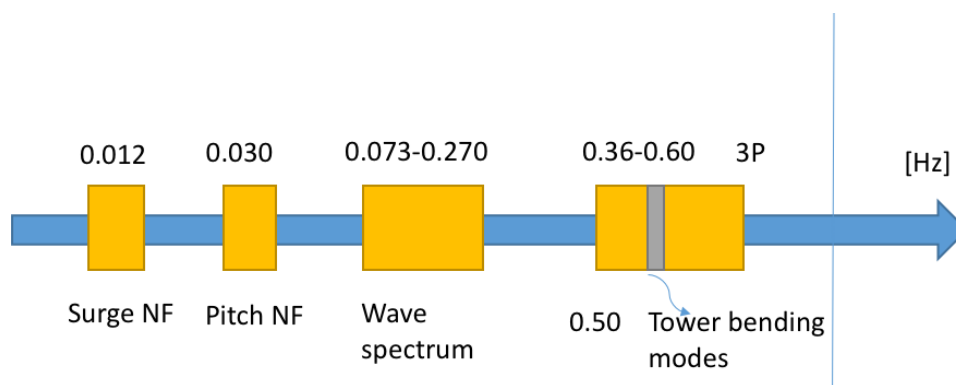
Figure 6.2: Frequency of interest for full scaled model test
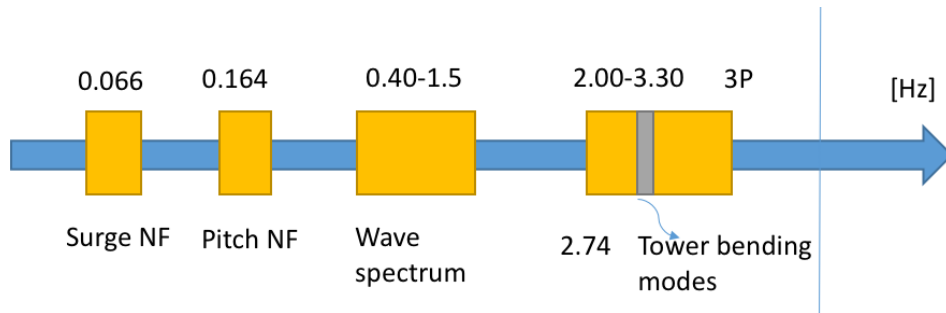
Figure 6.3: Frequency of interest for the 1:30 scaled model test

6.1.3   Simulation procedures

The simulation procedures are provided in Figure(6.4). SIMO-RIFLEX-AeroDyn simulation code is used. The simulation tool employs the finite element solver available in the combined SIMO/RIFLEX tool, passing position and velocity information to the aerodynamic code via DLL(dynamic link library) at the first iteration of each time step. Then, the DLL returns forces along the wind turbine blades. An external control system applies the generator torque according to a look-up table and blade pitch commands via PI control.

Figure 6.4: Illustration of emulated ReaTHM testing procedures

6.2   Computational Efficiency

The time for simulating the aerodynamic forces is recorded for each step, and the time steps in transition region are ignored. The average and the maximum time is shown in Table(6.3).It can be seen that the emulated ReaTHM(F) has 8% increased simulation time when compared to the rigid one.

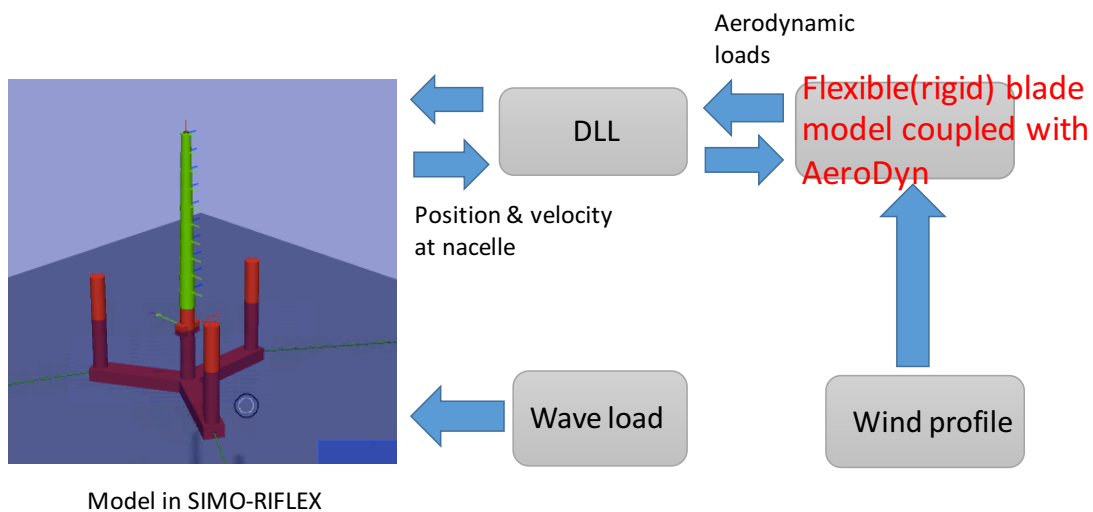For the full scaled model test of the semi-submersible platform, a maximum of 1.6×10^{-3}s simulation time is acceptable, since the highest frequency of interest is 0.60Hz, i.e. 1.67s. The simulation time is much lower than the highest frequency. Thus, the quantities of interest on the required frequency range can be captured correctly by the tests.

For the 1:30 scaled model test of the semi-submersible platform, the highest frequency of interest is 3.30Hz, i.e. 0.30s. 1.6×10^{-3}s simulation time is also acceptable. The time is only accounted for 0.5% of the highest frequency. Thus, the quantities of interest can be captured correctly in the 1:30 scaled model tests.

Table 6.3: Delayed time caused by simulating the aerodynamic forces

	mean time	max time
ReaTHM with flexible blades[s]	2.87×10^{-4}	1.6×10^{-3}
ReaTHM with rigid blades[s]	2.63×10^{-4}	7.6×10^{-4}

6.3   Decay tests

Decay tests were performed in six degrees of freedom to calculate the natural frequencies and damping of the platform motions. Decay tests were carried out in calm water without wind, and with wind below, at and above rated wind speed. The wind turbine control system is active with nonzero wind.

In addition, decay tests for integrated analysis of FWT were also performed in SIMA in order to verify the natural frequencies and mean offset of the emulated ReaTHM Testings with flexible blades.Then, a detail discussion for the emulated ReaTHM(F) is presented below, at and above rated region.

Table 6.4: Natural frequencies from decay tests

	Motion	no wind	8m/s	11.4m/s	15m/s
SIMA		83.5	86.7	90.6	87.5
ReaTHM(flexible)	surge[s]	83.5	86.5	90.1	87.5
ReaTHM(rigid)		83.4	86.8	90.4	87.5
SIMA		83.5	-	-	-
ReaTHM(flexible)	sway[s]	83.6	-	-	-
ReaTHM(rigid)		83.6	-	-	-
SIMA		25.3	-	-	-
ReaTHM(flexible)	heave[s]	25.3	-	-	-
ReaTHM(rigid)		25.3	-	-	-
SIMA		31.1	-	-	-
ReaTHM(flexible)	roll[s]	31.1	-	-	-
ReaTHM(rigid)		31.1	-	-	-
SIMA		31.1	31.6	34.6	33.2
ReaTHM(flexible)	pitch[s]	31.1	31.5	36.0	34.7
ReaTHM(rigid)		31.1	31.5	36.0	34.7
SIMA		62.7	-	-	-
ReaTHM(flexible)	yaw[s]	62.4	-	-	-
ReaTHM(rigid)		62.5	-	-	-

Table 6.5: Mean offset of platform in constant wind

	Motion	8m/s	11.4m/s	15m/s
SIMA		4.47	8.21	4.83
ReaTHM(flexible)	surge[m]	4.38	8.36	4.94
ReaTHM(rigid)		4.39	8.38	4.94
SIMA		4.18	7.78	4.61
ReaTHM(flexible)	pitch[deg]	4.22	7.85	4.73
ReaTHM(rigid)		4.23	7.90	4.73

The natural frequencies are summarized in Table(6.4). The emulated ReaTHM tests have close natural frequencies in six degrees of motion when compared to integrated FWT simulation in SIMA. The surge and pitch motion natural frequency are larger at the rated wind velocity due to the wind forces and the action of the pitch controller.

The mean offset of platform in the constant wind can also be obtained from decay tests. The mean offset is summaried in Table(6.5). In the below-rated wind velocity region, the mean offsets of the surge and pitch motion increase with the increase of wind velocity, because of the increase of thrust force. And ReaTHM(R) is observed to have a slightly higher offset since the rigid blade will produce larger thrust than the flexible one. The highest offset is observed at the rated wind velocity. Then in above-rated region, the mean offsets decrease due to the reduced thrust force.
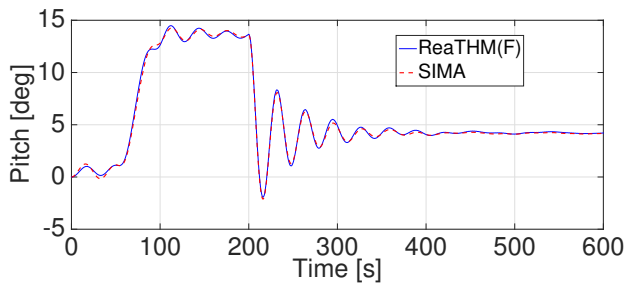
Figure(6.5) also shows that the ReaTHM with flexible blade has good agreement with SIMA simulation.
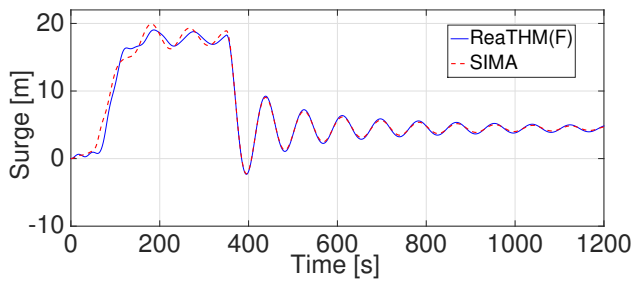
Surge decay in constant wind v=8m/s
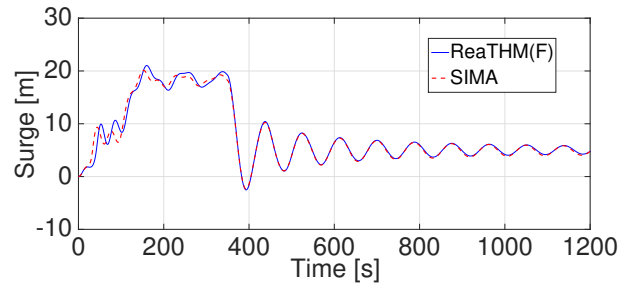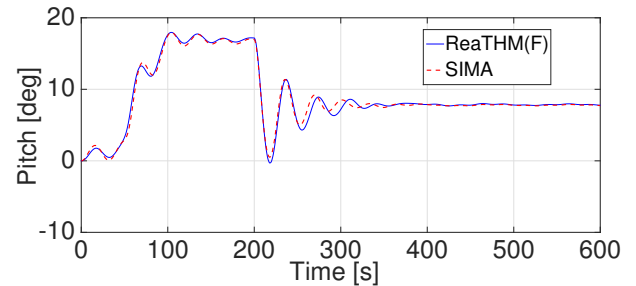

Surge decay in constant wind v=15m/s

Pitch decay in constant wind v=8m/s

Pitch decay in constant wind v=11.4m/s

Figure 6.5: Comparison surge decay motion and pitch decay motion between SIMA and emulated ReaTHM(F) simulation

6.3.1 Below rated wind velocity

Surge and pitch decay tests were carried out at wind velocity $U = 8m/s$. Figure(6.6) shows the surge decay at constant wind velocity 8m/s. Compared to the test without wind, a slight increase of damping is observed due to the aerodynamic damping. In below-rated wind region, assume the FWT has a small velocity down the wind, which means the relative velocity between wind and the FWT is smaller. The thrust force applied on the structure will decrease, leading to less motion into the wind. Thus, the damping is increased.

A significant lengthening of the natural period (3 seconds) is also observed in Figure(6.6) due to the wind forces and the action of the pitch controller.
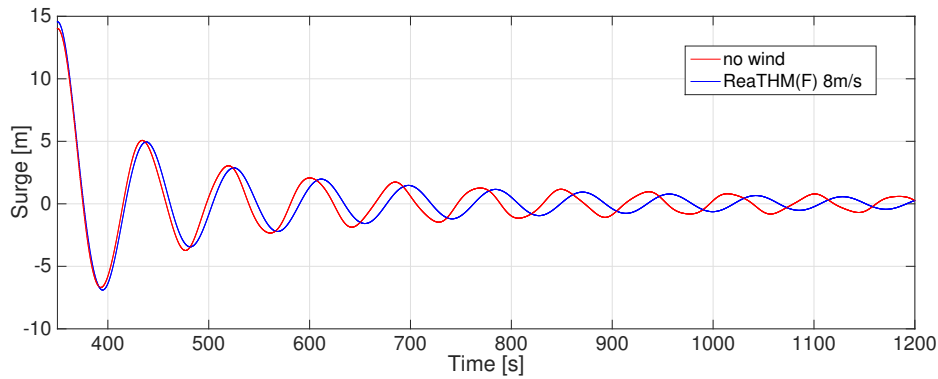

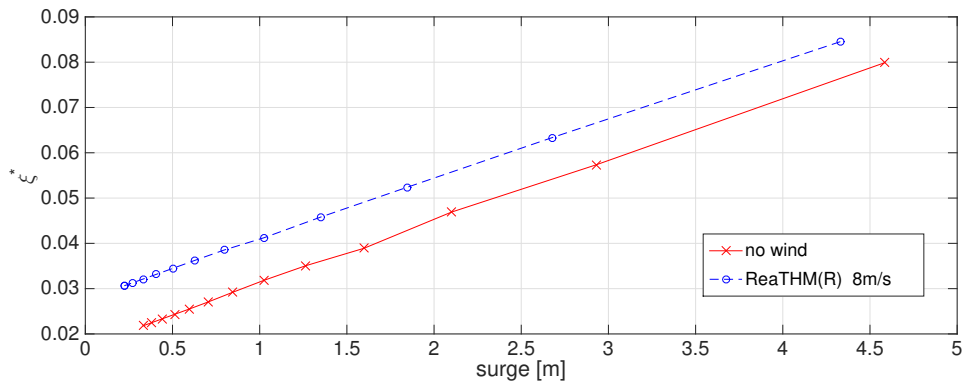
Figure 6.6: Surge decay at constant wind 8m/s

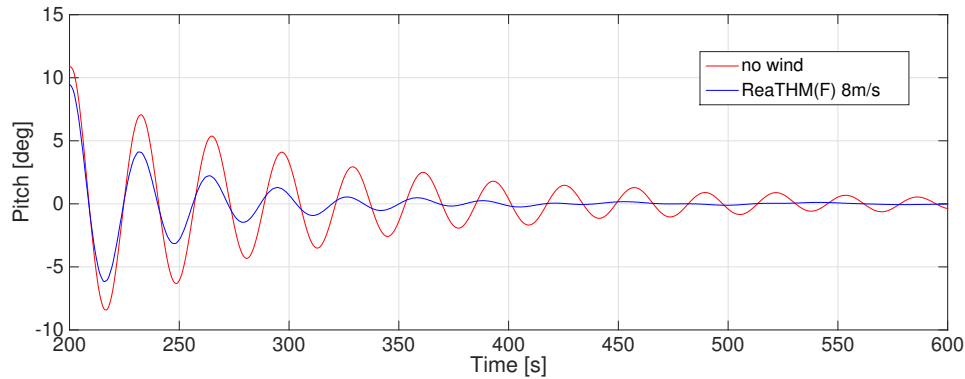Figure 6.7: Surge damping at constant wind 8m/s

Figure 6.8: Pitch decay at constant wind 8m/s

Figure(6.7) shows the damping ratio is increasing with the increase of the surge motion.

Figure(6.8) shows the pitch decay at below-rated wind velocity. A significant increase of pitch damping is observed when compared to the test without wind. And large variation in the length of each cycle in pitch decay is also observed. The later cycles have larger natural frequency.

6.3.2 At rated wind velocity

Surge and pitch decay tests were carried out at wind velocity 11.4m/s, which is the rated wind speed for the NREL 5 MW wind turbine. In can be seen that the surge damping at rated wind velocity is very close to the case without wind. However, it is expected a lower damping at the rated wind velocity due to the aerodynamic damping. At the rated wind velocity, assume the FWT moves against the wind, the relative wind velocity increases,and the thrust decreases, leading to further motion against the wind.

The reason for not having a lower damping is that in this case, the turbine reaches an equilibrium with a pretty high angle(7.8 degrees). It means that it doesn't necessarily reach the rated condition, since the wind speed it sees is effectively lower. Some decreased damping for 11.5 m/s rather than for 11.4 m/s is observed in Figure(6.9). It also means that the wind turbine is very sensitive at the rated velocity.

Figure(6.10) shows the pitch damping. The damping is slightly larger than the tests below the rated wind velocity. And a significant lengthen of the natural frequency can be observed.
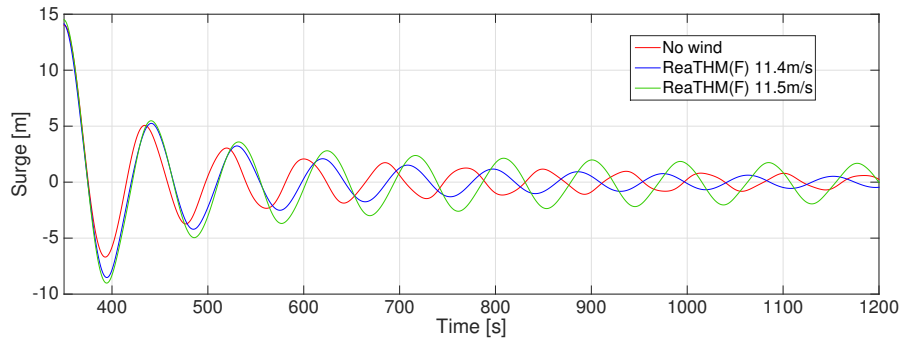
Figure 6.9: Surge damping at constant wind 11.4m/s
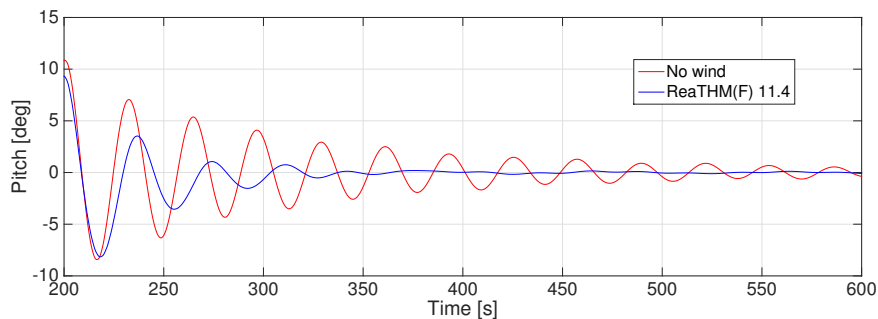
Figure 6.10: Pitch decay at constant wind 11.4m/s

6.3.3 Above rated wind velocity

The wind turbine blade pitch controller is active at above-rated wind speeds. There is a slight decrease in the surge damping when compared to the case without wind, but the difference is small. Figure(6.11) shows the surge velocity and Figure(6.12) shows the blade pitch angle. The mean blade pitch is around 17.2 degrees and the variation of the blade pitch angle is small. It can be seen that there is a delay between the surge velocity and the blade pitch angle. Assume the FWT moves against the wind, the relative velocity seen by the blades will increase. However, due to the delay of the blade pitch, the thrust force is also decreased with a delay, leading to the presence of some aerodynamic damping. Therefore, we do not seen a significant decrease of the surge damping at above rated wind velocity region.

For the pitch decay, the damping is higher for the 20m/s wind velocity when compared to no wind case. Similarly, there is a delay between the platform pitch motion velocity and the blade

Figure 6.11: Surge velocity at above rated wind velocity U=20m/s

Figure 6.12: Blade pitch angle for surge decay at above rated wind velocity U=20m/s

Figure 6.13: Pitch velocity at above rated wind velocity U=20m/s

Figure 6.14: Blade pitch angle for pitch decay at above rated wind velocity U=20m/s

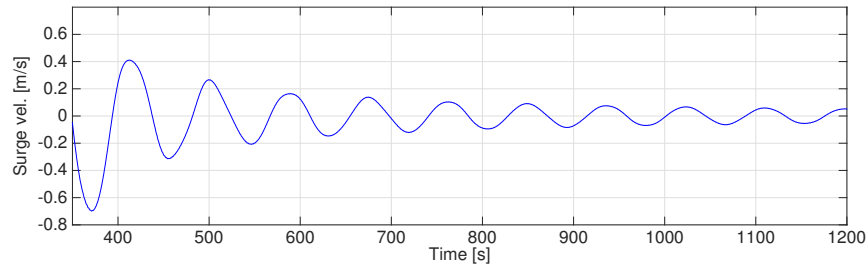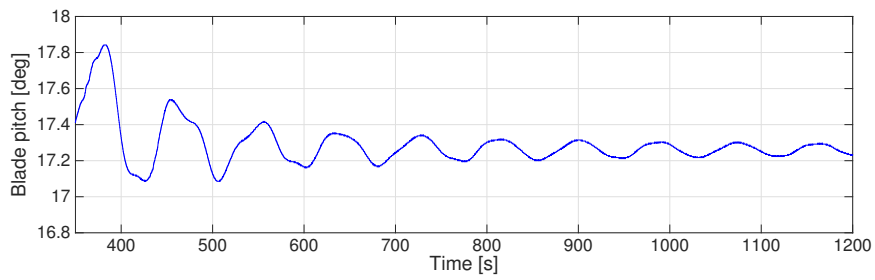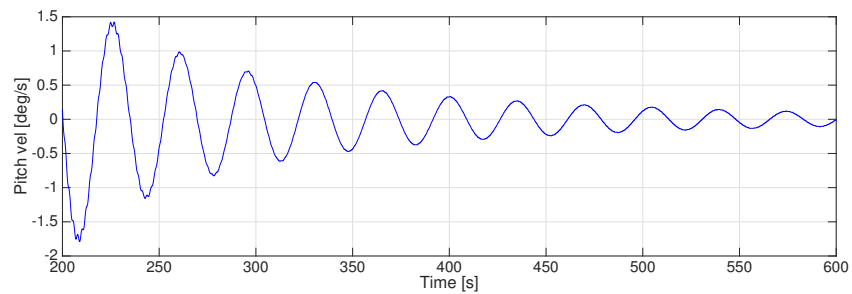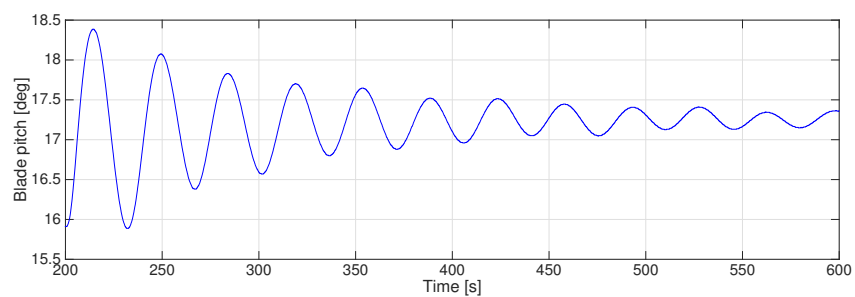pitch angle, as shown in Figure(6.13) and Figure(6.14). The effect of the delay results in the presence of some aerodynamic damping in the system.

6.4 Irregular wave and turbulent wind tests

6.4.1 Load cases

The emulated ReaTHM testings are also verified in the irregular wave and turbulent wind cases. Three load cases were chosen for the tests. One mean wind speed below the rated, one near the rated, and one above the rated, as shown in Table(6.6).

The tests were carried out with aligned wind and waves coming from the x direction and no current was included. The wind turbine was operating and no extreme load cases were considered. The LC1 and LC2 were chosen as the same to the cases in Reference[29], so that comparison can be made with 2015 NOWITECH ReaTHM testing.

The effective simulation time for each case is 1 hour. The turbulent wind input was generated in 64-bit TurbSim v1.5[30].

Table 6.6: Irregular wave and turbulent wind test load cases

	H_s[m]	T_p[s]	U[m/s]	I%	comment
LC1	3.60	10.2	11	17.0	with/without wind,flexible,rigid
LC2	5.20	8	8	19.5	flexible,rigid
LC3	4	10	18	14.9	flexible,rigid

6.4.2 Responese of ReaTHM with flexible blades

The emulated ReaTHM testings with the flexible blades were calculated with wind-wave combined loads under load case 1. The integrated analysis of the FWT under load case 1 was also carried out in SIMA, which is referred as the baseline performance to verify the emulated ReaTHM(F) tesing in the irregular wave and turbulent wind. The baseline performance is presented in Appendix D. The comparison between the emulated ReaTHM test and SIMA simulation is shown in Table(6.7), which shows good agreements.

Table 6.7: Results from the emulated ReaTHM test with flexible blades with wind-wave combined loads under load case 1 compared to SIMA simulation

	ReaTHM(F)	SIMA
Std. suege[m]	1.65	1.60
Mean Surge[m]	6.91	6.92
Std. Heave[m]	0.19	0.19
Std. Pitch[deg]	1.69	1.99
Mean Pitch[deg]	6.36	6.13
Std. M_{TOWY}[MNm]	20.68	23.08
Mean M_{TOWY}[MNm]	87.79	84.13
Std. F_{moor1}[KN]	78.81	75.13

The emulated ReaTHM testings with the flexible blades were also calculated with wave-only load, wind-only load, and wind-wave combined loads under load case 1. Table(6.8) shows some key statistics values for the emulated ReaTHM testing with flexible blades.

Table 6.8: Statistics values for ReaTHM testing with flexible blades

	wind-wave	wave only	wind only	Superposition in time domain	Deviation (%) from superposition
Std.Surge[m]	1.65	0.26	1.86	1.87	11.84
Mean Surge[m]	6.91	0.16	6.75	6.91	0.08
Std. Heave[m]	0.19	0.18	0.07	0.20	1.86
Std. Pitch[deg]	1.69	0.18	1.72	1.72	1.37
Mean Pitch[deg]	6.36	0.21	6.34	6.55	2.86
Std. M_{TOWY}[MNm]	20.68	6.35	20.06	20.97	1.41
Mean M_{TOWY}[MNm]	87.79	3.07	87.65	90.72	3.22
Std. F_{MOOR1}[KN]	78.81	16.98	90.79	92.18	14.50
Std. F_{MOOR2}[KN]	67.95	14.09	74.95	76.16	10.78
Std. F_{MOOR3}[KN]	70.97	14.09	78.54	79.69	10.95

Figure(6.15) shows the time series of platform motions in wind-wave combined, wind-only and wave-only conditions. The mean values were removed. And the corresponding low frequency, wave frequency and high frequency part of motions spectrum are presented in Figure(6.16).

Figure 6.15: Platform motions in wind-wave,wind-only,wave-only conditions for ReaTHM testing with flexible blades.$H_s = 3.6m.T_p = 10.2s.U = 11m/s.$(Mean value removed)

Surge motion is mainly caused by the wind force. And it can be seen that the low-frequency motions are primarily excited by the wind. A large peak is observed at 0.075rad/s. Since the

surge natural frequency is around 0.075rad/s, resonance occurs due to the wind force. And a small peak is observed at 0.19rad/s(pitch natural frequency). Thus, it can be concluded that surge motion and pitch motion is a little coupled. In addition, the presence of waves tends to decrease the low-frequency response. The wind loads does not excited much motion on the wave-frequency part. And there are small peaks at the tower flexible mode due to the impulse loads at a the triple of the rotor rotation frequency(3P).
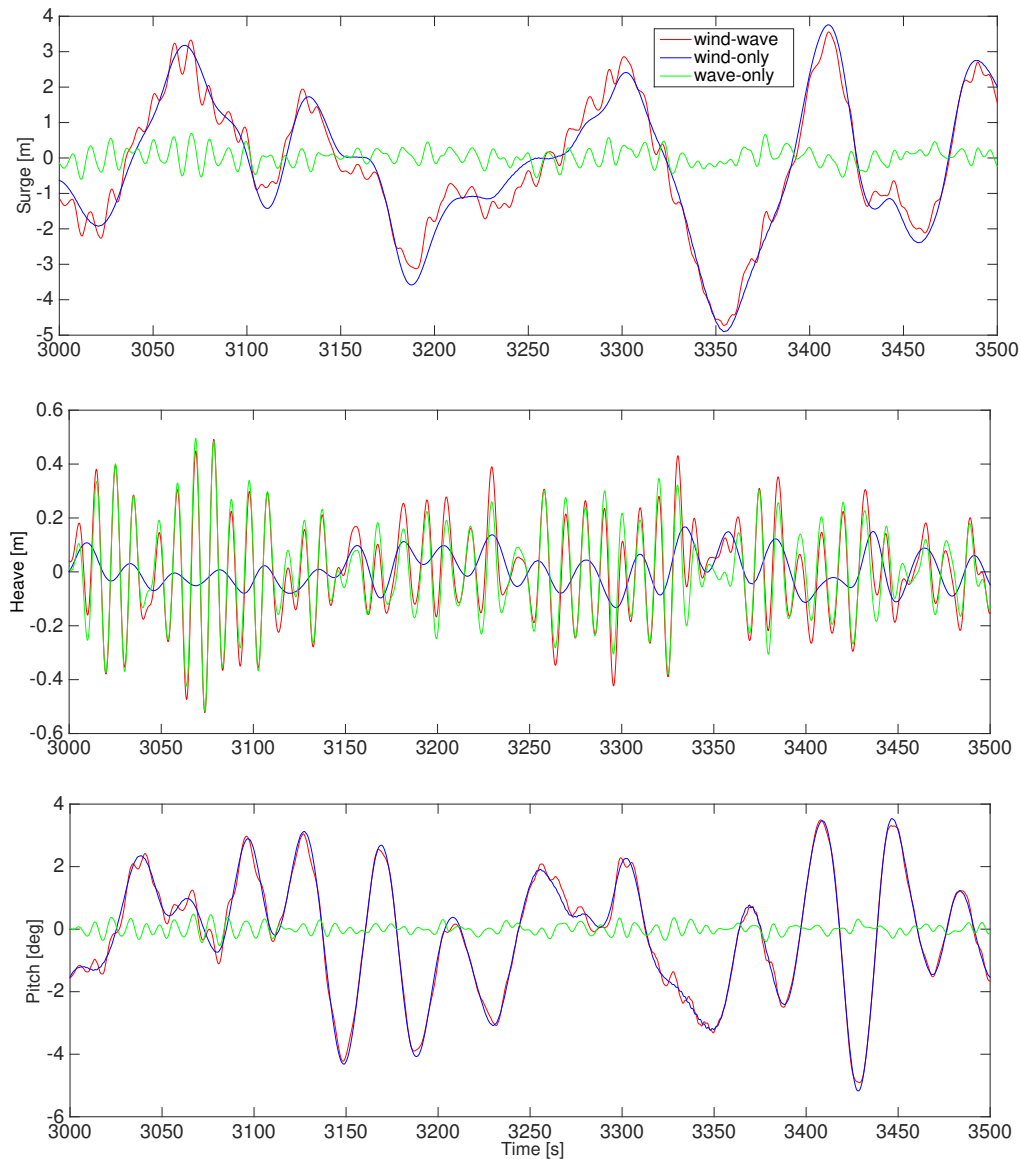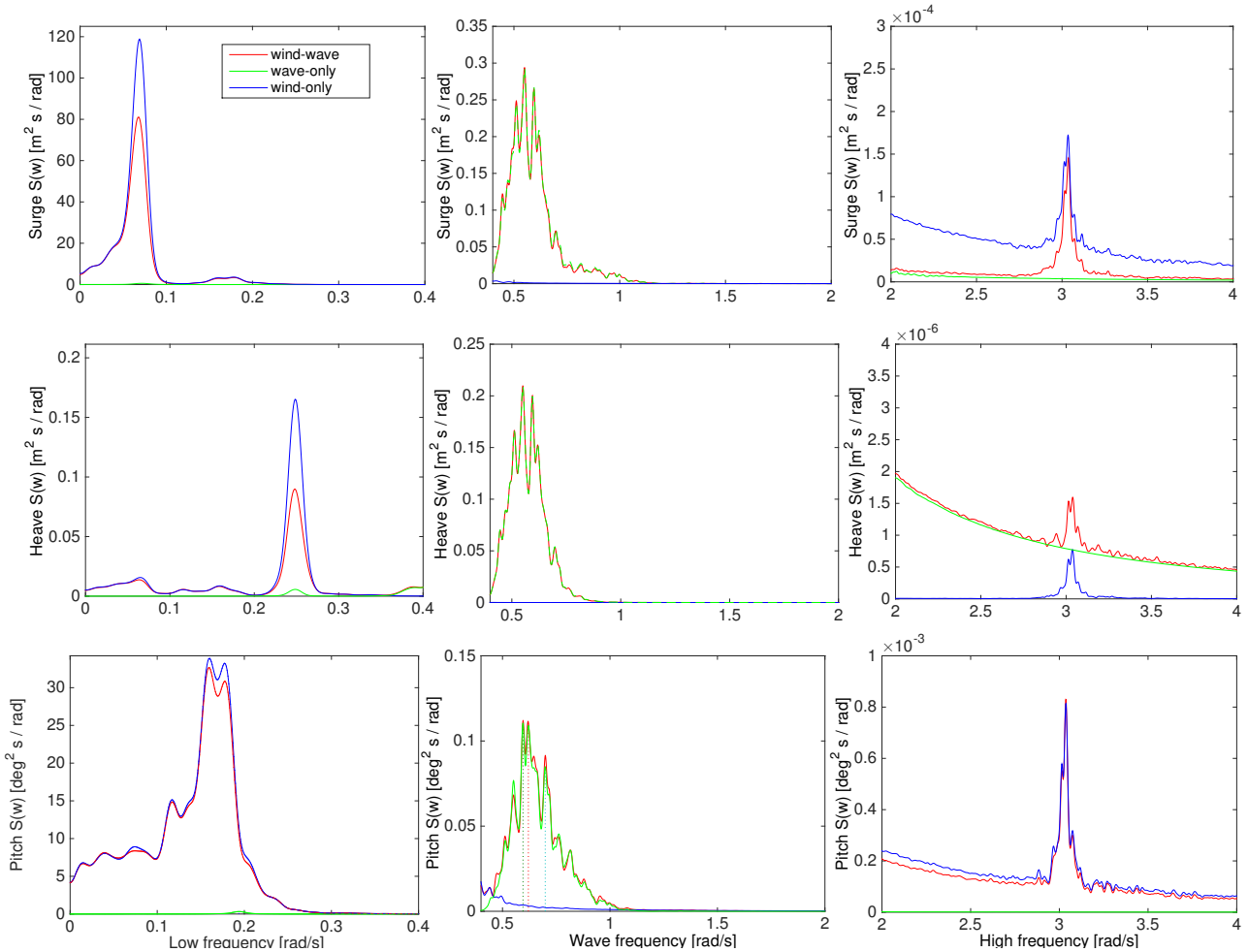

Figure 6.16: Spectrum for platform motions in wind-wave,wind-only,wave-only conditions for ReaTHM testing with flexible blades.$H_s = 3.6m.T_p = 10.2s.U = 11m/s$.

Heave motion is mainly caused by the wave loads. From the low-frequency heave motion, it can be seen that there is a peak around 0.25rad/s, since it is the heave resonance frequency. The heave response is largest in wave-only condition and the presence of wind damped the heave motion.

Pitch motion is mainly caused by the wind loads. And the low-frequency motions are primarily excited by the wind. A large peak is observed at pitch natural frequency(0.19rad/s). And some small peaks are observed around 0.1rad/s, since the coupling effect between surge and pitch motion. Also, it can be seen that wind loads causes little energy on the wave-frequency.

Figure(6.17) shows the time series and spectral of the fore-aft tower bending moment(M_{TOWY}). It can be seen that the wind loads contributes more to M_{TOWY} than the wave loads. The low frequency response is mainly excited by the wind loads and the wave-frequency responses are quite independent from the low- frequency response. In addition, due to the coupling effect between the tower flexible mode and 3P, large peaks are observed in high frequency part except for the wave-only condition.
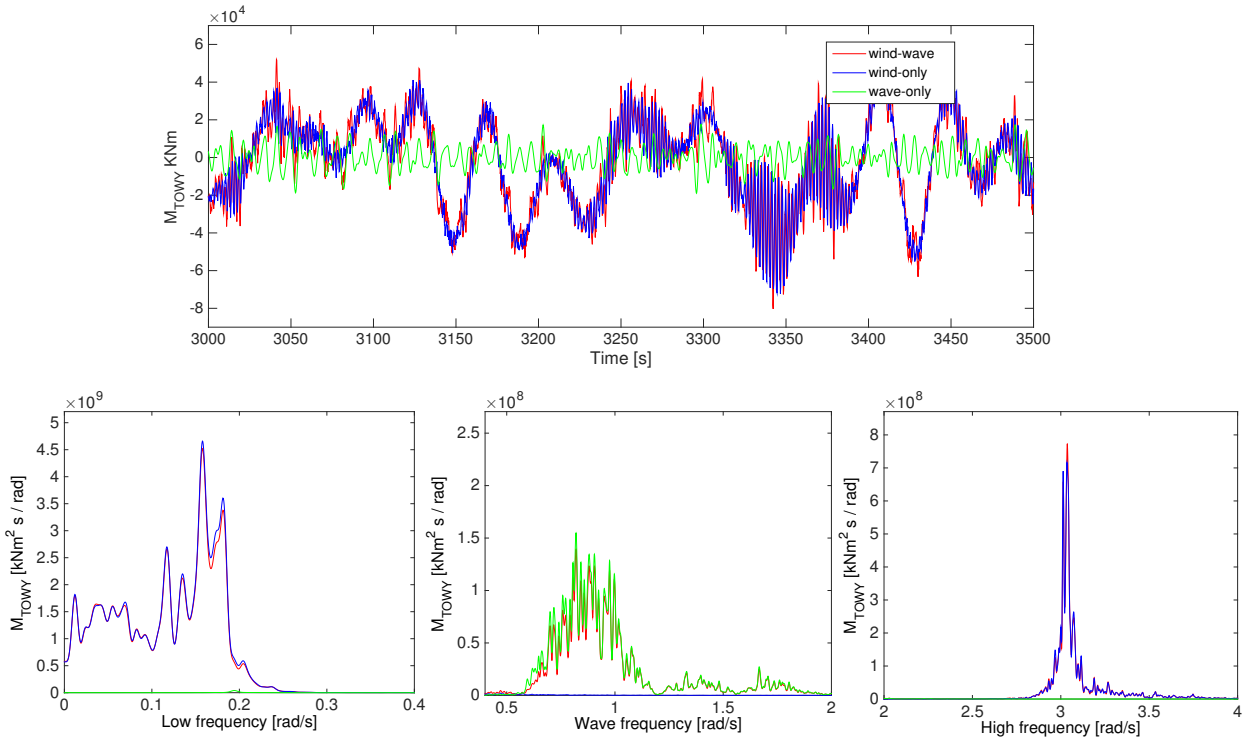
Figure 6.17: Time history and spectrum for the tower fore-aft bending moment in wind-wave,wind-only,wave-only conditions for ReaTHM testing with flexible blades. $H_s = 3.6m. T_p = 10.2s. U = 11m/s.$(Mean value removed)

Figure(6.18) shows the time series and spectrum of the mooring line 1 tension. The tension is largest in wave-only condition and the presence of wind damped the tension. The low frequency response is mainly excited by the wind load. In addition, there is some response at the tower

bending mode frequency.
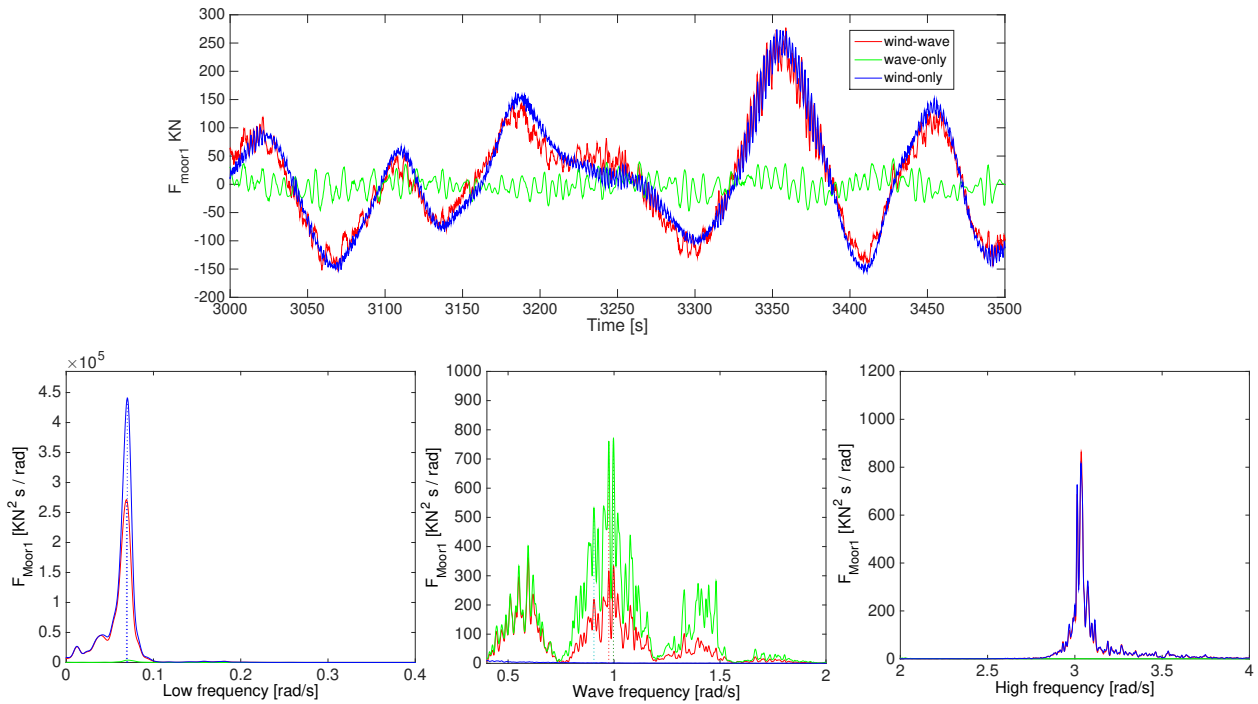
Figure 6.18: Time history and spectrum of mooring line tensions in wind-wave,wind-only,wave-only conditions for ReaTHM testing with flexible blades.$H_s = 3.6m.T_p = 10.2s.U = 11m/s.$(Mean value removed)

6.4.3 Responese of ReaTHM with rigid blades

Similarly, the emulated ReaTHM testing with rigid blades was also carried out. The responses are compared with the results from the 2015 NOWITECH ReaTHM testing with the rigid blades shown in Ref[29].

The keys statistics values are listed in Table(6.9) and shows consistent trend with the results from the 2015 NOWITECH ReaTHM testing. The comparison between the emulated ReaTHM(F) testing and ReaTHM(R) testing is discussed in detail in Chapter 7.

Table 6.9: Statistics values for ReaTHM testing with rigid blades

	wind-wave	wave only	wind only	Superposition in time domain	Deviation (%) from superposition
Std.Surge[m]	1.74	0.26	1.96	1.98	11.80
Mean Surge[m]	6.98	0.16	6.83	6.99	0.15
Std. Heave[m]	0.19	0.18	0.07	0.20	1.57
Std. Pitch[deg]	1.77	0.18	1.80	1.80	1.18
Mean Pitch[deg]	6.45	0.21	6.44	6.64	2.88
Std. M_{TOWY}[MNm]	23.41	6.35	23.00	23.79	1.58
Mean M_{TOWY}[MNm]	89.40	3.07	89.26	92.33	3.17
Std. F_{MOOR1}[KN]	83.59	16.98	96.23	97.49	14.14
Std. F_{MOOR2}[KN]	72.51	14.09	80.06	81.14	10.64
Std. F_{MOOR3}[KN]	74.76	14.09	82.96	84.07	11.07

Chapter 7

Effect of blade flexibility

7.1 Effect on semi-submersible platform

The emulated ReaTHM testing were carried out in load cases as shown in Table(6.6) with flexible and rigid blades. Difference in percentage of the results given by emulated ReaTHM(R),relative to emulated ReaTHM(F) are shows in Table(7.1) under LC1.

In general, using a rigid rotor is conservative. As expected, the rigid blade has a slightly higher thrust force in the below-rated wind velocity. The increase of the rotor mean thrust results in an increase in mean surge motion, pitch motion and tower base bending moment. The standard deviation of the thrust for the rigid rotor is increased by 5.75%, which leads to an increased dynamic response of surge and pitch motion.

Based on the mooring line arrangement, line 2 and line 3 are more tensioned than line 1. Due to a higher thrust force in the emulated ReaTHM(R), line 1 is less tensioned in the emulated ReaTHM(R) when compared to the emulated ReaTHM(F). Thus, a negative difference of percentage is observed.

Figure(7.1) shows the thrust spectrum. At the low frequency part, the emulated ReaTHM(R) has a slightly higher peak for the thrust force, leading to the higher mean value of the thrust. The wave frequency responses for these two cases are similar. The emulated ReaTHM(R) has a larger peak in the high frequency part due to the influence of the tower shadow, which results in the increased standard deviation. Since the incoming wind has to travel around the tower, the tower changes the local inflow. As each blade passes through the tower, the thrust can vary at

blade passing frequency(3P). This effect is much larger for the rigid blades.

Table 7.1: Difference in percentage of the results given by ReaTHM(R),relative to ReaTHM(F). $H_s = 3.6m. T_p = 10.2s. U = 11m/s$.

difference [%]	Mean	Max	std.
Thrust	1.04	1.60	5.75
Surge	1.11	2.43	5.68
Pitch	1.37	3.81	3.23
M_{TOWY}	1.36	10.64	8.25
F_{Moor1}	-0.30	1.67	6.07
F_{Moor2}	0.24	1.10	6.73
F_{Moor3}	0.10	0.87	5.34

Figure 7.1: Thrust spectrum for the emulated ReaTHM with the rigid blades and the flexible blades in load case $1. H_s = 3.6m. T_p = 10.2s. U = 11m/s$.

Figure(7.2) shows the platform motions spectrum. Due to the aligned wind and wave loads, the sway, roll and yaw motion is small. The surge and pitch motions are more important.

For the surge motion at the low frequency part, the emulated ReaTHM(F) has less responses. The rigid blades results in more dynamic response in the tower bending mode. Similarly, the presence of the blade structure flexibility damped the pitch motion, leading to a reduced mean pitch motion for the emulated ReaTHM(F). And at the high frequency part, the rigid blades has a large peak, which explains the larger standard deviation in the emulated ReaTHM(R).

For the sway, roll and yaw motion, the flexible blades result in a larger asymmetrical rotor load, which becomes lateral force and yaw moment. However, since the motions are small, they are not the main considerations for this tests.

Figure 7.2: Platform motions for the emulated ReaTHM with the rigid blades and the flexible blades in load case $1. H_s = 3.6m. T_p = 10.2s. U = 11m/s.$

Figure(7.3) shows the spectrum for the tower fore-aft bending moment and the mooring lines tensions. M_{TOWY} is mainly caused by the surge and pitch motions of the platform, while the mooring line tensions is mainly caused by the surge motion. The flexible blades have lower thrust force, leading to a slightly lower surge and pitch motion. Thus, the mean M_{TOWY} and mooring lines tensions are smaller in the emulated ReaTHM(F) tesing. In addition, large increased response is observed in the high frequency part for the emulated ReaTHM(R) testing. This is because that as each blade passes through the tower, the resulting thrust variations at blade passing frequency(3P) can lead to a large fatigue load. This effect is much larger for the rigid blades.

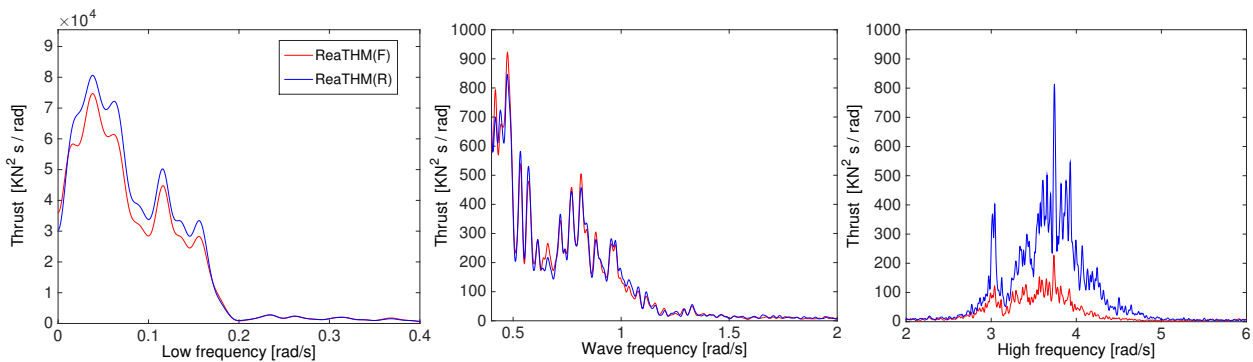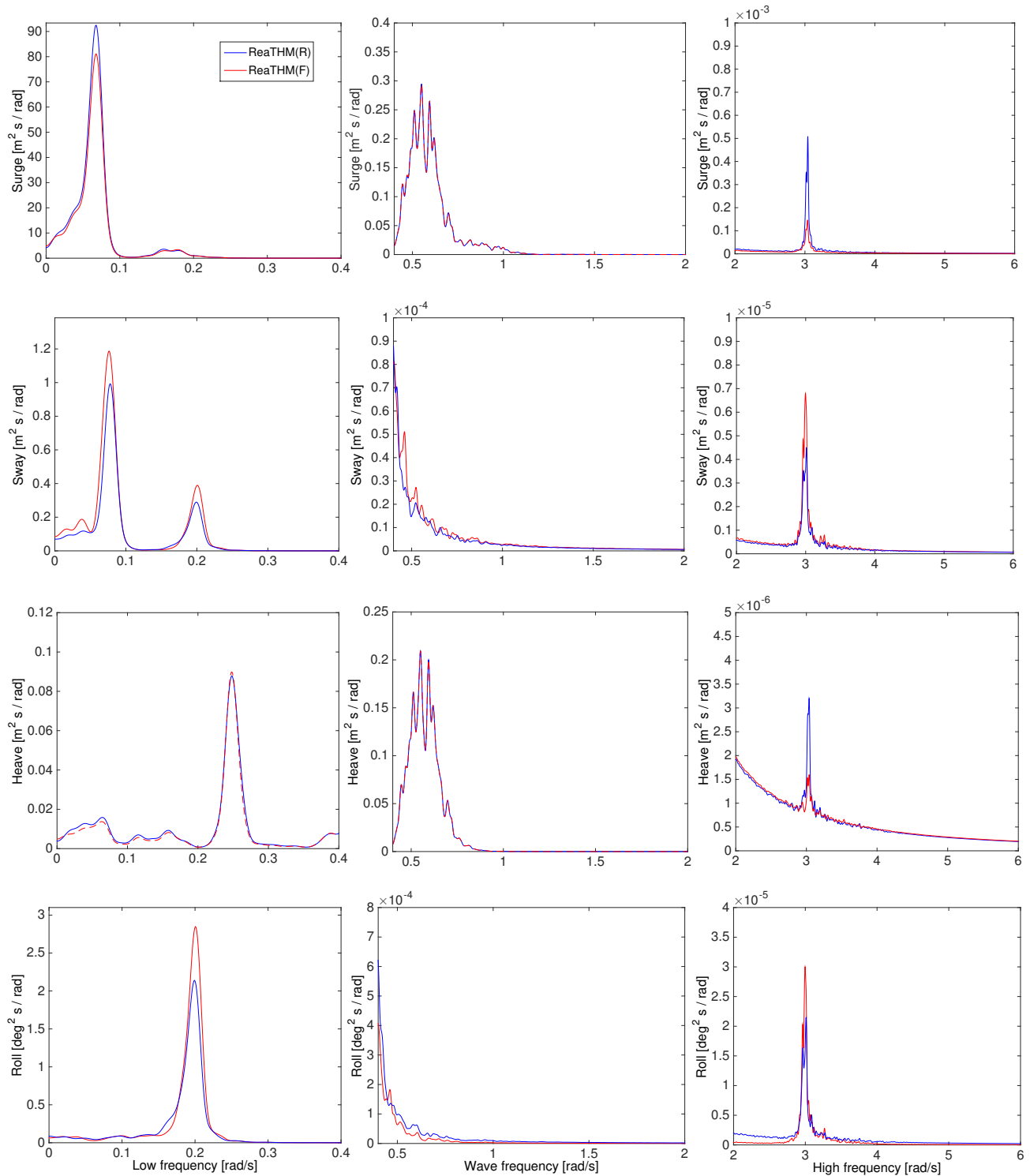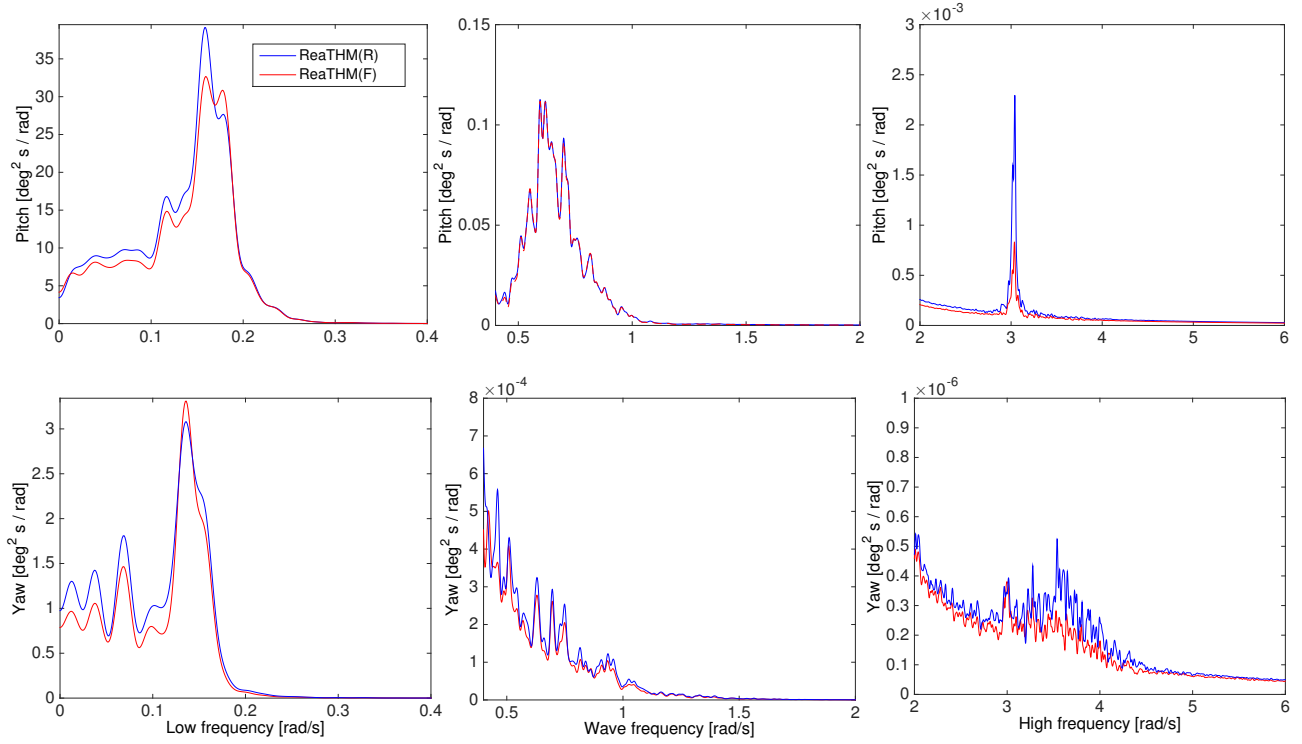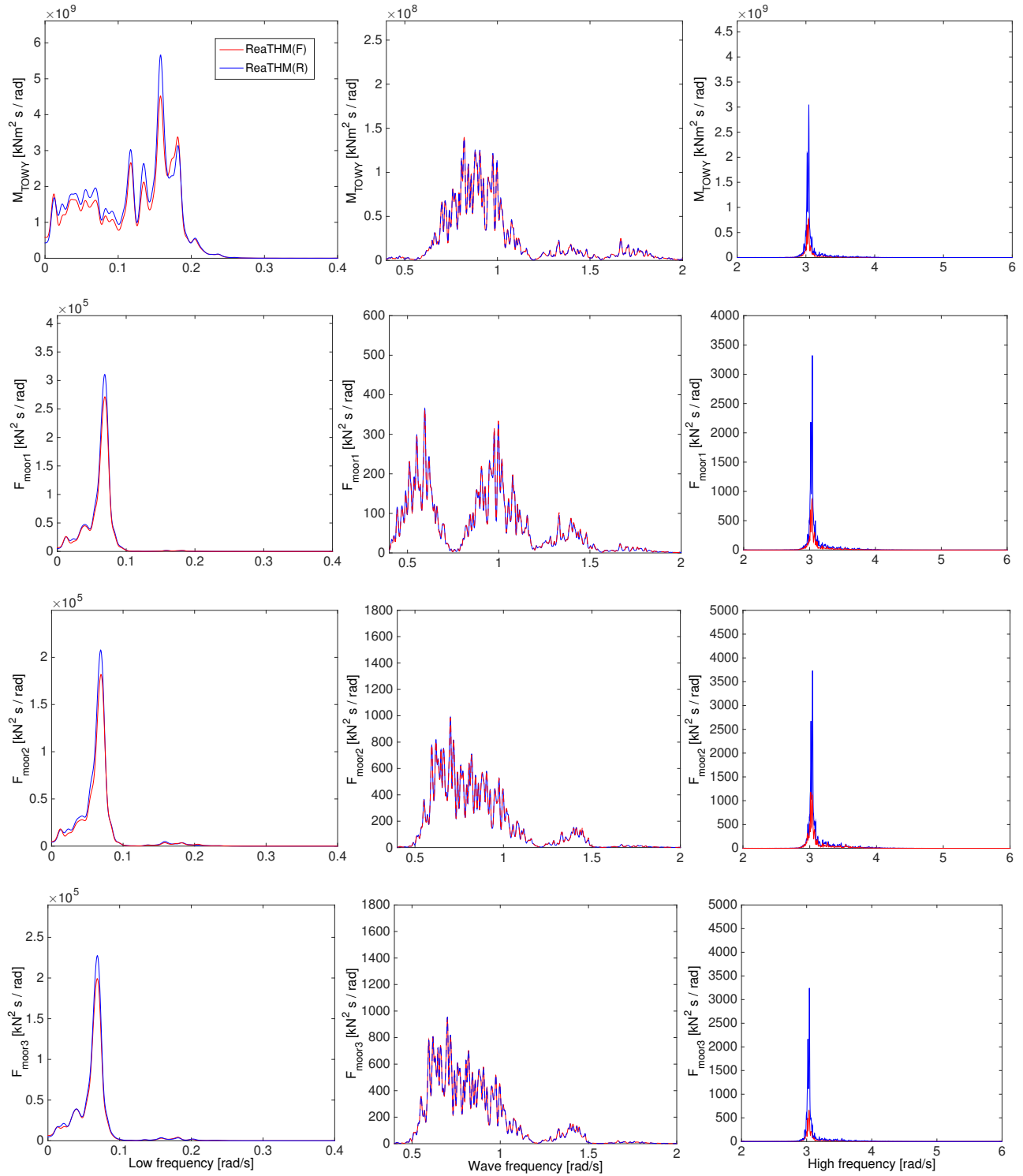Figure 7.3: Tower fore-aft bending moment and mooring lines tension spectrum for the emulated ReaTHM with the rigid blades and the flexible blades in load case 1. $H_s = 3.6m$. $T_p = 10.2s$. $U = 11m/s$.

Figure(7.4) show the effect of blade structure flexibility on the platform under the different load cases. It can be seen that the blade structure flexibility has little effect on the mean value for the platform motions, M_{TOWY} and the mooring lines tension(within the difference of (1-2%). At below rated wind region, the test with rigid blades leads to a slightly higher mean value due to the higher thrust force. At above rated region, the test with the flexible blades has larger motion.

The blade flexibility has a large effect on the standard deviation of the tower fore-aft bending moment and the mooring lines tensions(up to 10%). Thus, if the fatigue analysis should be considered for the ReaTHM testing, a rigid blade will be too conservative.
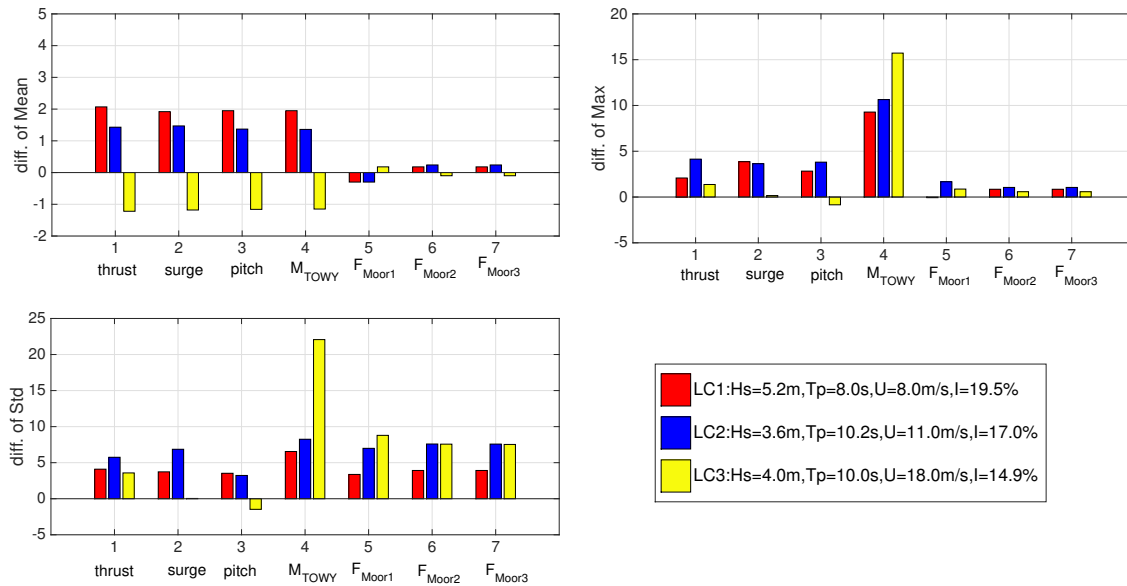
Figure 7.4: Difference in percentage of the results given by ReaTHM(R),relative to ReaTHM(F) with wind velocity below, near, above rated.

7.2 Effect on TLP platform

The effects of blade structure flexibility is also dependent on the platform type. In this section, the blade structure flexibility effect on the tension leg platform(TLP) is discussed.

TLPWT1[31] design is used. The natural frequencies for this FWT and the blade vibration are given in Table(7.2). It can be seen that the natural frequencies of TLPWT1 is close to the natural frequency of the blades. Thus, resonance may occur, leading to larger dynamics response for

the platform with the flexible blades.

Table 7.2: Natural frequency for TLPWT1 design and blade vibration

	TLPWT1		Blade
surge[s]	55.78	1st flap[s]	1.50
Heave[s]	0.55	1st edge[s]	0.92
Pitch[s]	2.79	2st flap[s]	0.51
Yaw[s]	13.99	2st edge[s]	0.25
		3st flap[s]	0.22
		1st torsion[s]	0.18

7.3 Summary

The effect of blade structure flexibility for the dynamic analysis of the FWTs, can be concluded in two aspects:

(1) The influence of the tower shadow. Since the incoming wind has to travel around the tower, the tower changes the local inflow. As each blade passes through the tower, the resulting thrust variations at blade passing frequency(3P) can lead to a large fatigue load. This effect is much larger for the rigid blades: if the local inflow velocity is reduced due to the tower shadow, the velocity seen by the rigid blade is changed suddenly. However, for the flexible ones, it can vibrate to offset some of the change.

The fatigue load has large effect on the tower fore-aft bending moment for the semi-submersible platform, since the 1st tower bending mode is coupled with 3P(blade passing frequency).

(2) Resonance may occur when the platform natural frequency is closed to the blade vibration natural frequency, such as the wind turbine suppurted by the tension leg platform(TLP).

Chapter 8

Sensitivity to limited actuation

In ReaTHM testing, the aerodynamics loads are evaluated numerically. Then, the loads are applied to the physical model by a set of actuators. In principle, all six components(three aerodynamic forces, two aerodynamic moments and the generator torque) should be applied through an appropriate actuation. However, some of these components may be smaller than others. Thus, it may have less effect on the FWT global analysis. Bachynski E. E.[32] shows a sensitive analysis on effects of incomplete actuation in the ReaTHM testing with rigid blades, and concludes that five out of the six components of the aerodynamic loading significantly affected the quantities of interest and the aerodynamic heave force is removed during the 2015 NOWITECH ReaTHM tesing.

In this section, a sensitive analysis on effects of incomplete actuation in the emulated ReaTHM testing with flexible blades is carried out. The aerodynamics loads are removed one by one. Then the corresponding analysis is carried out through SIMO-RIFEX-AeroDyn with flexible blades. The quantities of interest are compared to the baseline platform performance which is calculated with the complete actuation.

The tests are carried out with aligned wind and waves coming from the x direction and no current is included. The load cases are chosen as Table(6.6). For each case, the effective simulation time is 1 hour.

8.1 Baseline platform performance

The NOWITECH semi-submersible platform performances on LC1,LC2 and LC3 are predicted by SIMO-RIFLEX-AeroDyn simulation with complete actuation(all six components of loads are applied), which is shown in Figure(8.1).

These results are considered to be baseline performance for further comparison. Figure(8.1) shows the standard deviations for the selected responses below, near and above rated wind velocity. It can be seen that the standard deviations for sway($\sigma(\xi_2)$), heave($\sigma(\xi_3)$), roll($\sigma(\xi_4)$) and yaw($\sigma(\xi_6)$) motion are small since there are little lateral forces with aligned wind and wave loads. In general, the standard deviations tends to increase as the wind velocity. But for surge motion, ($\sigma(\xi_1)$) decrease at the load case 3.
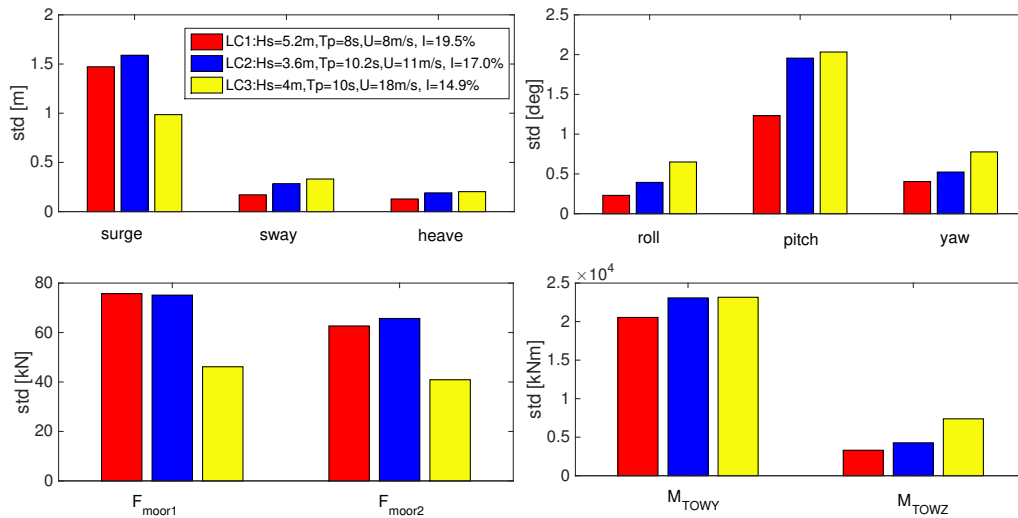
Figure 8.1: Standard deviations for the selected responses below, near and above rated wind velocity

8.2 Effects of incomplete actuation

The aerodynamic thrust and generator torque are large and considered to be of great importance effects for a FWT. In addition, according to Ref[32], in aligned wind and wave conditions, the effect of removing aerodynamic sway force is up to 80% change in standard deviation of sway motion, roll motion, and tower side-side bending moment. Thus, in the present work, it is

also considered that the aerodynamic sway force has important effect.

This section considers the effects of removing:

(1) Aerodynamic pitch moment

(2) Aerodynamic yaw moment

(3) Aerodybamic heave force

8.2.1 Aerodynamic pitch moment

In general, the aerodynamic pitch moment has a relatively large effect on the tower base fore-aft bending moment(M_{TOWY}), with 2-7% on the mean value, and 3-8% on the standard value.

Figure(8.3) shows the spectrum for the tower base fore-aft bending moment and the pitch motion. It can be seen that removing the aerodynamic pitch moment results in a slight decrease near 0.16rad/s, but a small increase at 0.18rad/s. Thus, the overall difference on mean values is not very large.

In addition, removing the aerodynamic pitch moment has limited effect on the wave frequency response. In high frequency part, a significant decrease is observed for the case without the aerodynamic pitch moment.

Ref[32] shows that removing pitch moment had quite a large effect on the standard deviation of the pitch motion($\approx 10\%$) for sensitivity analysis of the ReaTHM testing with the rigid blades. However, in this study, the difference is somewhat limited($\approx 1\%$). The reason is that only aligned wind-wave cases are considered in this thesis, while Ref[32] also includes the misaligned load cases.

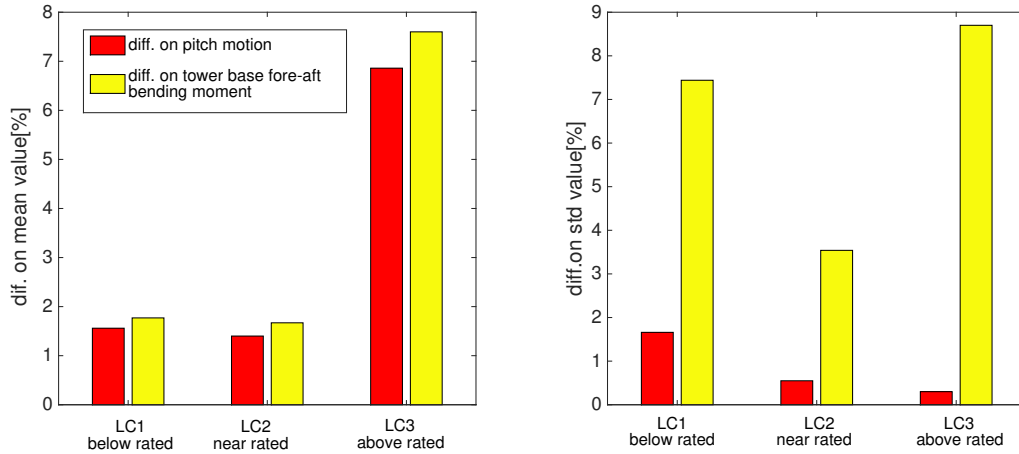And the aerodynamic pitch moment has limited effect on surge, sway and roll motion with aligned wind and wave.

Figure 8.2: Difference on pitch motion and tower base fore-aft bending moment given by removing aerodynamic pitch moment actuation,relative to complete actuation
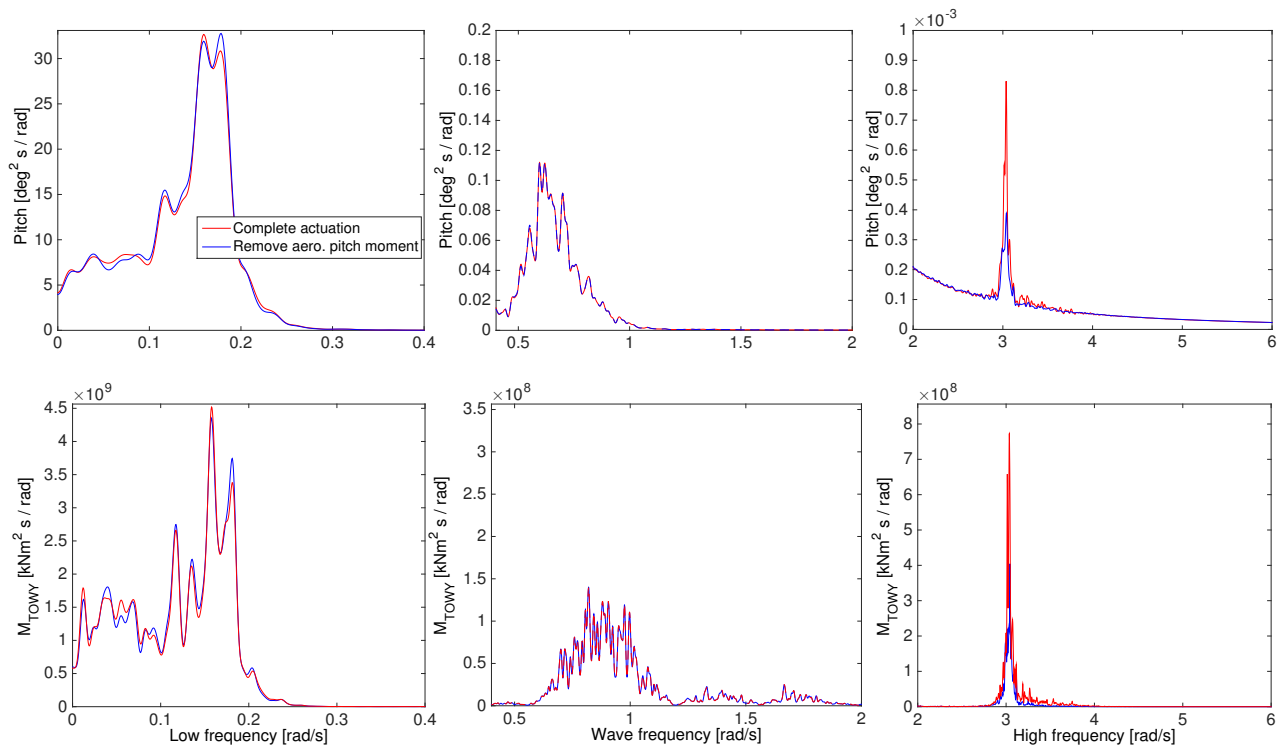

Figure 8.3: Tower base fore-aft bending moment and pitch motion spectrum for LC2 with complete actuation and with removed aerodynamics pitch moment

8.2.2 Aerodynamic yaw moment

With the aligned wind and wave loads, the aerodynamic yaw moment is caused by the asymmetrical out-of-plane rotor loads. The platform yaw motion is small. In this situation, the relative difference between the case with complete actuation and the case removing the aerodynamic yaw moment, is not representative. Thus, the yaw motion time series is presented in Figure(8.4). It can be seen that the yaw motion is mainly caused by the aerodynamic yaw moment with the aligned wind and wave loads.

In addition, the aerodynamic yaw moment also have relatively large effect on the platform sway motion. It can be seen from Figure(8.5) that removing the aerodynamic yaw moment results in a decrease in sway frequency.
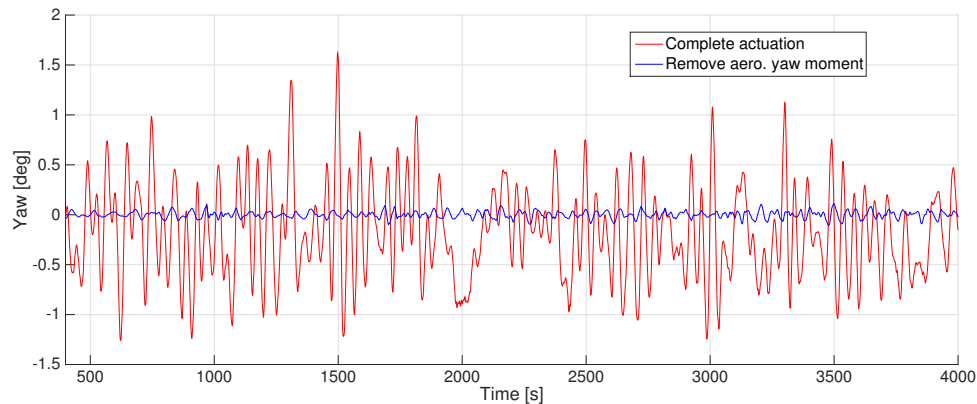

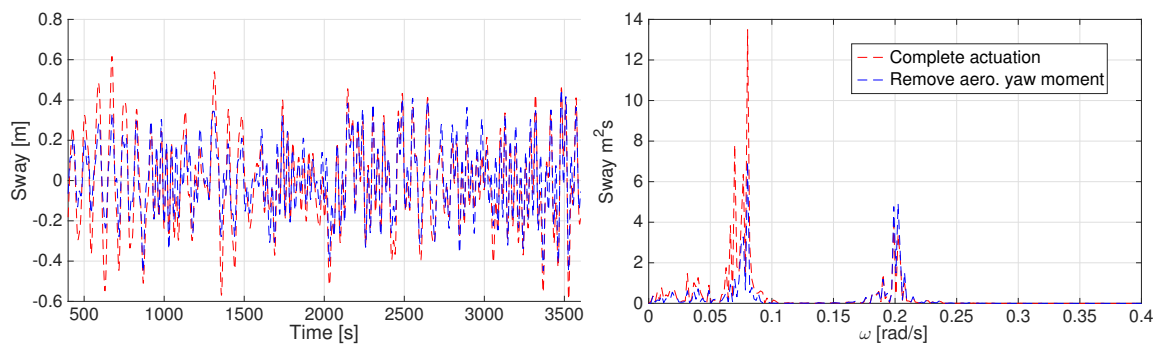Figure 8.4: Yaw motion with complete actuation and with removed aerodynamic yaw moment on LC2

Figure 8.5: Sway motion and spectra with complete actuation and with removed aerodynamic yaw moment on LC2

8.2.3 Aerodynamic heave force

The aerodynamic heave force has little effect on the platform motions, mooring lines and the tower base bending moment.

Figure(8.6) shows the time series and spectra of heave motion. It can be seen that removing the aerodynamic heave force almost has no obvious change on heave motion. This is because the heave motion is primarily caused by the wave loads.
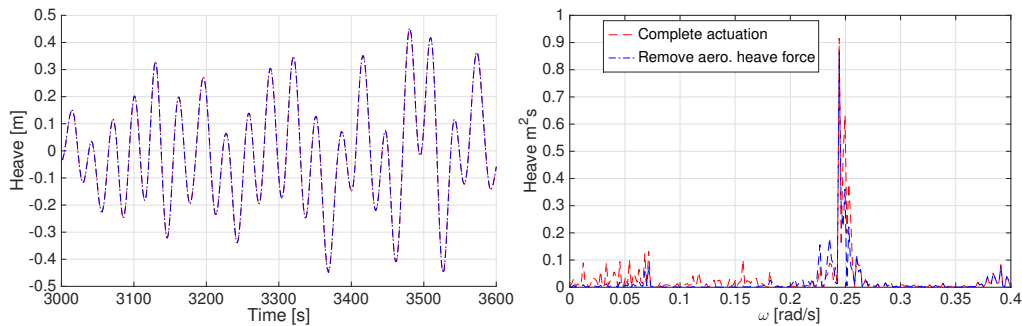
Figure 8.6: Heave motion and spectra with complete actuation and with removed aerodynamic heave force on LC2

8.2.4 Summary

The sensitivity analysis of ReaTHM testing of FWTs with limited actuation of aerodynamic forces was developed. Since some motions of the platform are small under the aligned wave and wind loads(such as sway, roll and yaw) , the relative difference can be very large, while the absolute change of the value is low.

Aerodynamic thrust force and generator torque are generally considered to be important for the global motions of FWTs. In addition, the aerodynamic pitch moment has large effect on the tower base fore-aft bending moment, and a slightly large effect on the platform pitch motion. The aerodynamic yaw moment is the primary cause for the platform yaw motion. If the aerodynamic yaw moment is removed, the platform yaw motion can not be excited.

However, the aerodynamic heave force has very limited effect on the platform motion, mooring lines and the tower base fore-aft bending moment. Therefore, in order to reduce the computation time, and reduce the complexity of the actuation system arrangement in ReaTHM testing, the aerodynamic heave force can be removed.

Chapter 9

Recommendation and conclusion

9.1 Recommendation

This study shows that using a rigid blade model is too conservative. The effects of blade flexibility on the mean values is limited(1%). The effects on the standard deviation of platfrom motions and mooring lines are around 3-8%. In particular, the effects of blade flexibility on the standard deviation of tower fore-aft bending moment are large, leading to large fatigue damage.

However, 2015 NOWITECH ReaTHM test uses a rigid tower model. Therefore, using flexible blades model will not lead to a significant difference.

If SINTEF Ocean plans to do the ReaTHM test with tension leg platform(TLP), it is recommended to use the developed methodology to see if flexible blades should be used.

In addition, the simulation time with the presented flexible blade model is acceptable.

9.2 Conclusion

In this study, an effective flexible rotor model is provided using finite element analysis and modal analysis method. The steady-state responses of the flexible rotor model and the rigid rotor model are given and compared to the results from FAST. It shows that the flexible blades have lower thrust force in below-rated wind velocity region and a slightly lower pitch angle in above-rated region.

The emulated ReaTHM testing with rigid and flexible blades was carried out. The setup of

the test and the performance of the rotor model was verified by decay tests, as well as tests in irregular wind and wave case. It turns out that using a rigid blade is more conservative. The rigid blade will produce larger fatigue loads at blade passing frequency(3P). Thus, if fatigue analysis should be included in the ReaTHM testing, it is better to use a flexible blade.

In addition, the effect of the blade structure flexibility is dependent on the platform type. When the bottom-fixed or TLP support structures are used, it is desired to consider flexible blades due to the resonance between the blade vibration and platform motions.

The computational efficiency is briefly discussed in the present work. It shows that using a flexible blade leads to a mean of 8% increased simulation time for each step. The simulation time is acceptable in the emulated ReaTHM testing with the semi-submersible platform. Besides, some platforms may have higher requirement for computational efficiency. For example, the TLPWT has lower natural periods. Thus, to capture the quantities of interest on the required frequency range is more difficult.

Another challenge for the ReaTHM testing is how to put the actuators to mimic the simulated aerodynamic forces correctly. A sensitivity analysis of the importance of the six loads components was carried out. It shows that the aerodynamic heave force has little effect on the quantities of interest. Thus, the aerodynamic heave force can be removed in order to reduce the complexity of the actuation system arrangement in ReaTHM testing.

Appendix A

Matrices used in FEA

The shape function can be expressed as:

$$\mathbf{N_s} = [\frac{x_{e+1} - x}{h_e}, 0, 0, 0, 0, 0, \frac{x - x_e}{h_e}, 0, 0, 0, 0, 0]^T \tag{A.1}$$

$$\mathbf{N_\phi} = [0, \frac{x_{e+1} - x}{h_e}, 0, 0, 0, 0, 0, \frac{x - x_e}{h_e}, 0, 0, 0, 0]^T$$

$$\mathbf{N_v} = [0, 0, \frac{(x - x_{e+1})^2(2x - 3x_e + x_{e+1})}{h_e^3}, \frac{(x - x_e)(x - x_{e+1})^2}{h_e^2}, 0, 0,$$
$$0, 0, \frac{-(x - x_e)^2(2x + x_e - 3x_{e+1})}{h_e^3}, \frac{(x - x_e)^2(x - x_{e+1})}{h_e^2}, 0, 0]^T$$

$$\mathbf{N_w} = [0, 0, 0, 0, \frac{(x - x_{e+1})^2(2x - 3x_e + x_{e+1})}{h_e^3}, \frac{(x - x_e)(x - x_{e+1})^2}{h_e^2},$$
$$0, 0, 0, 0, \frac{-(x - x_e)^2(2x + x_e - 3x_{e+1})}{h_e^3}, \frac{(x - x_e)^2(x - x_{e+1})}{h_e^2}]^T$$

in which h_e is the element size given by:

$$h_e = x_{e+1} - x_e \tag{A.2}$$

The element deformation vector can be denoted as:

$$\mathbf{d_e} = [s_e, \phi_e, v_e, \theta_e, w_e, \psi_e, s_{e+1}, \phi_{e+1}, v_{e+1}, \theta_{e+1}, w_{e+1}, \psi_{e+1}]^T \tag{A.3}$$

The weighting functions for the stretch, torsion, chordwise and flapwise deformations are given

by:

$$\bar{s} = (\eta_{\mathbf{e}})^T \mathbf{N_s} \quad \bar{\phi} = (\eta_{\mathbf{e}})^T \mathbf{N}_\phi \quad \bar{v} = (\eta_{\mathbf{e}})^T \mathbf{N_v} \quad \bar{w} = (\eta_{\mathbf{e}})^T \mathbf{N_w} \tag{A.4}$$

The discretized equations for the stretch, chordwise, flapwise and torsion motions are:

$$\sum_{e=1}^{N} (\eta_{\mathbf{e}})^T \left\{ \mathbf{m_e}\ddot{\mathbf{d}}_\mathbf{e} + 2\Omega\mathbf{g_e}\dot{\mathbf{d}}_\mathbf{e} + \left[\mathbf{k_e} + \Omega^2(\mathbf{s_e} - \mathbf{c_e}) \right]\mathbf{d_e} \right\} = \sum_{e=1}^{N} (\eta_{\mathbf{e}})^T \mathbf{f_e} \tag{A.5}$$

where $\mathbf{m_e}$, $\mathbf{g_e}$, $\mathbf{k_e}$ and $\mathbf{s_e}$ are the element mass, the element gyroscopic, the element stiffness and the element motion-induced stiffness matrices. These element matrices can be expressed as:

$$\mathbf{m_e} = \rho A \int_{x_e}^{x_{e+1}} \left[\mathbf{N_s}\mathbf{N_s}^T + \mathbf{N_v}\mathbf{N_v}^T + \mathbf{N_w}\mathbf{N_w}^T \right] dx + \rho J \int_{x_e}^{x_{e+1}} \mathbf{N}_\phi\mathbf{N}_\phi^T dx \tag{A.6}$$

$$\mathbf{g_e} = \rho A \int_{x_e}^{x_{e+1}} \left[\mathbf{N_v}\mathbf{N_s}^T - \mathbf{N_s}\mathbf{N_v}^T \right] dx$$

$$\mathbf{k_e} = \int_{x_e}^{x_{e+1}} \left[EA\frac{d\mathbf{N_s}}{dx}\frac{d\mathbf{N_s}^T}{dx} + EI_z\frac{d^2\mathbf{N_v}}{dx^2}\frac{d^2\mathbf{N_v}^T}{dx^2} + EI_y\frac{d^2\mathbf{N_w}}{dx^2}\frac{d^2\mathbf{N_w}^T}{dx^2} \right.$$
$$\left. + EI_{yz}\frac{d^2\mathbf{N_v}}{dx^2}\frac{d^2\mathbf{N_w}^T}{dx^2} + EI_{yz}\frac{d^2\mathbf{N_w}}{dx^2}\frac{d^2\mathbf{N_v}^T}{dx^2} + GJ\frac{d\mathbf{N}_\phi}{dx}\frac{d\mathbf{N}_\phi^T}{dx} \right] dx$$

$$\mathbf{s_e} = \rho A \int_{x_e}^{x_{e+1}} \left[r(L-x) + \frac{1}{2}(L^2 - x^2) \right] \left(\frac{d\mathbf{N_v}}{dx}\frac{d\mathbf{N_v}^T}{dx} + \frac{d\mathbf{N_w}}{dx}\frac{d\mathbf{N_w}^T}{dx} \right) dx$$

$$\mathbf{c_e} = \rho A \int_{x_e}^{x_{e+1}} \left[\mathbf{N_s}\mathbf{N_s}^T + \mathbf{N_v}\mathbf{N_v}^T \right]$$

$$\mathbf{f_e} = \int_{x_e}^{x_{e+1}} \left[\rho A \Omega^2(r+x)\mathbf{N_s} + f_v\mathbf{N_v} + f_w\mathbf{N_w} + M_\phi\mathbf{N}_\phi \right] dx$$

Appendix B

Matrices used in Modal analysis

Flapwise and edgewise deflections are coupled. The equations of motion in time domain are given as:

$$
\begin{bmatrix} M_{ij}^{11} & M_{ij}^{12} \\ M_{ij}^{21} & M_{ij}^{22} \end{bmatrix} \ddot{\mathbf{q}} + 2\xi\omega_{\mathbf{n}}\dot{\mathbf{q}} + \begin{bmatrix} K_{ij}^{B2} + \Omega^2(K_{ij}^{G2} - M_{ij}^{22}) & K_{ij}^{B23} \\ K_{ij}^{B32} & K_{ij}^{B3} + \Omega^2 K_{ij}^{G3} \end{bmatrix} \mathbf{q} = \begin{bmatrix} F_{2i}^{v} \\ F_{3i}^{w} \end{bmatrix}
$$

Since two flapwise and two edgewise mode shapes are considered. The matrices $\mathbf{M}$, $\omega_{\mathbf{n}}$, $\mathbf{K}$ are 4×4. where:

$$
M_{ij}^{ab} = \int_0^L \rho A \Phi_{ai} \Phi_{bj} dx
$$

$$
K_{ij}^{B2} = \int_0^L EI_z \Phi_{2i}'' \Phi_{2j}'' dx
$$

$$
K_{ij}^{B3} = \int_0^L EI_y \Phi_{3i}'' \Phi_{3j}'' dx
$$

$$
K_{ij}^{Bab} = \int_0^L EI_{yz} \Phi_{ai}'' \Phi_{bj}'' dx
$$

$$
K_{ij}^{Ga} = \int_0^L \frac{1}{2} \rho A (L^2 - x^2) \Phi_{ai}' \Phi_{aj}' dx + r \int_0^L \rho A (L - x) \Phi_{ai}' \Phi_{aj}' dx
$$

$$
F_{2i}^{v} = \int_0^L f_v \Phi_{2i} dx
$$

$$
F_{3i}^{w} = \int_0^L f_w \Phi_{3i} dx
$$

Only one torsion mode shape is considered and the equtions of motion is given as:

$$\left[\int_0^L \rho J \Phi \Phi dx\right] \ddot{q} + 2\xi\omega_n \dot{q} + \left[\int_0^L GJ\Phi'\Phi' dx\right] q = \int_0^L M_\phi \Phi dx$$

Appendix C

Coordinate transformation matrix

$$\mathbf{T}_{\alpha_t} = \begin{bmatrix} \cos\alpha_t & 0 & -\sin\alpha_t \\ 0 & 1 & 0 \\ \sin\alpha_t & 0 & \cos\alpha_t \end{bmatrix} \tag{C.1}$$

$$\mathbf{T}_{\mathbf{azim}} = \begin{bmatrix} 1 & 0 & 0 \\ 0 & \cos\alpha_{azim} & \sin\alpha_{azim} \\ 0 & -\sin\alpha_{azim} & \cos\alpha_{azim} \end{bmatrix} \tag{C.2}$$

$$\mathbf{T}_{\mathbf{c}} = \begin{bmatrix} \cos\alpha_c & 0 & -\sin\alpha_c \\ 0 & 1 & 0 \\ \sin\alpha_c & 0 & \cos\alpha_c \end{bmatrix} \tag{C.3}$$

$$\mathbf{T}_{\mathbf{p}} = \begin{bmatrix} \cos\alpha_p & -\sin\alpha_p & 0 \\ \sin\alpha_p & \cos\alpha_p & 0 \\ 0 & 0 & 1 \end{bmatrix} \tag{C.4}$$

$$\mathbf{T}_{\beta} = \begin{bmatrix} \cos\beta & -\sin\beta & 0 \\ \sin\beta & \cos\beta & 0 \\ 0 & 0 & 1 \end{bmatrix} \tag{C.5}$$

Appendix D

SIMA Baseline performance

The integrated SIMA simulation of the semi-submersible platform under load case 1 ($H_s = 3.60\,m, T_p = 10.2\,s, U = 11\,m/s$) is presented.

Table D.1: Statistics values for the integrated SIMA simulation with flexible blades

	wind-wave
Std.Surge[m]	1.60
Mean Surge[m]	6.92
Std. Sway[m]	0.28
Std. Heave[m]	0.19
Std. Roll[deg]	0.40
Std. Pitch[deg]	1.99
Mean Pitch[deg]	6.13
Std. Yaw[deg]	0.53
Std. M_{TOWY}[MNm]	23.08
Mean M_{TOWY}[MNm]	84.13
Std. F_{MOOR1}[KN]	75.13
Std. F_{MOOR2}[KN]	65.70
Std. F_{MOOR3}[KN]	70.21
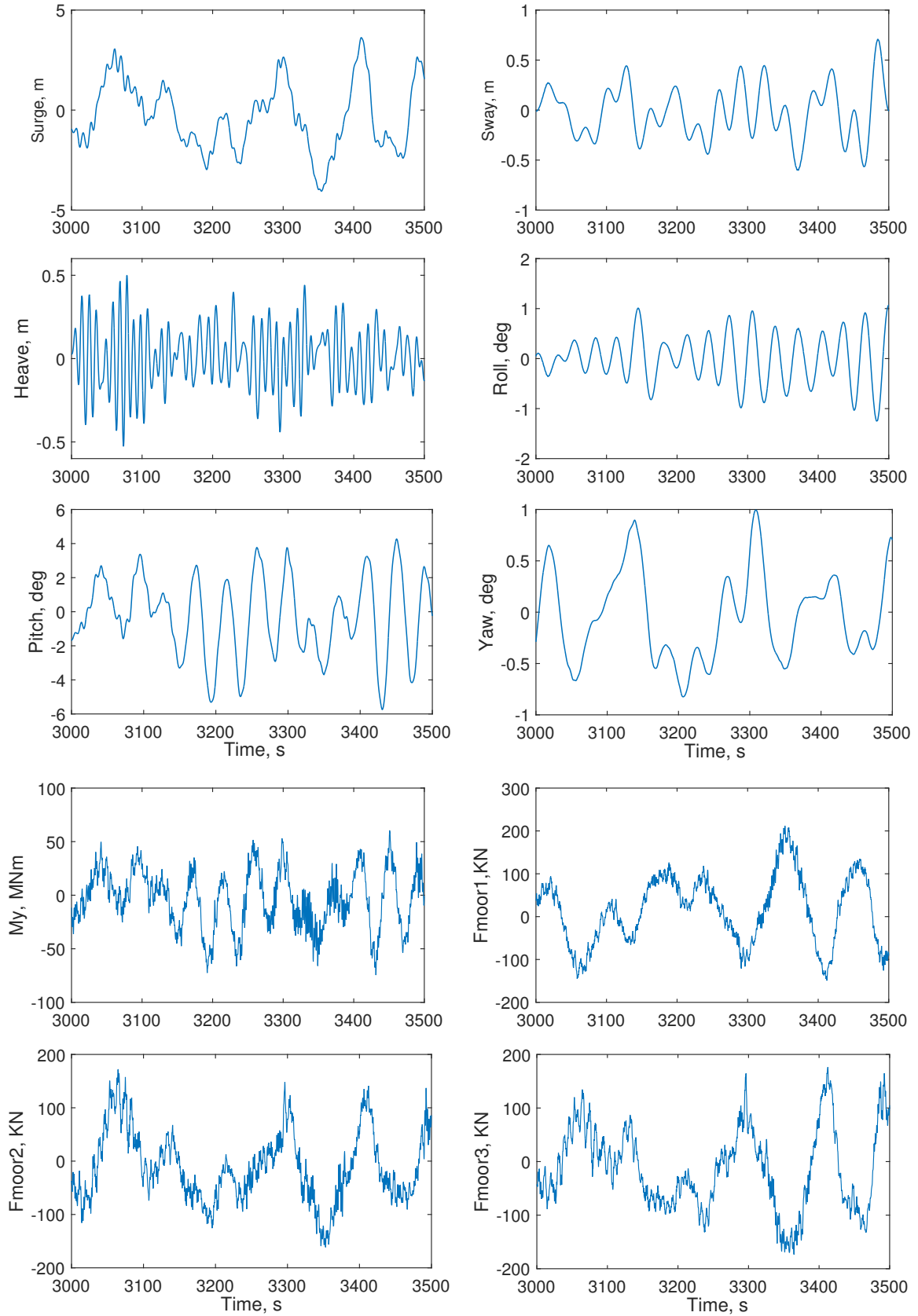
Bibliography

[1] Simon-Philippe Breton and Geir Moe. Status, plans and technologies for offshore wind turbines in europe and north america. *Renewable Energy*, 34(3):646 – 654, 2009.

[2] Rebecca J. Barthelmie and Sara Pryor. A review of the economics of offshore wind farms. *Wind Engineering*, 25(4):203–213, 2001.

[3] Wind Europe. Wind in power 2016 european statistics. Technical report, Wind Europe, 2017.

[4] EWEA. Deep water- the next step for offshore wind energy. Technical report, European Wind Energy Association, 2013.

[5] Amy N Robertson, Jason M Jonkman, Andrew J Goupee, Alexander J Coulling, Ian Prowell, James Browning, Marco D Masciola, and Paul Molta. Summary of conclusions and recommendations drawn from the deepcwind scaled floating offshore wind system test campaign. In *ASME 2013 32nd International Conference on Ocean, Offshore and Arctic Engineering*, pages V008T09A053–V008T09A053. American Society of Mechanical Engineers, 2013.

[6] Matthew J Fowler, Richard W Kimball, Dale A Thomas, and Andrew J Goupee. Design and testing of scale model wind turbines for use in wind/wave basin model tests of floating offshore wind turbines. In *ASME 2013 32nd International Conference on Ocean, Offshore and Arctic Engineering*, pages V008T09A004–V008T09A004. American Society of Mechanical Engineers, 2013.

[7] Thomas Sauder, Valentin Chabaud, Maxime Thys, Erin E Bachynski, and Lars Ove Sæther. Real-time hybrid model testing of a braceless semi-submersible wind turbine: Part i—the

hybrid approach. In *ASME 2016 35th International Conference on Ocean, Offshore and Arctic Engineering,* pages V006T09A039–V006T09A039. American Society of Mechanical Engineers, 2016.

[8] Chenyu Luan, Zhen Gao, and Torgeir Moan. Design and analysis of a braceless steel 5-mw semi-submersible wind turbine. In *ASME 2016 35th International Conference on Ocean, Offshore and Arctic Engineering,* pages V006T09A052–V006T09A052. American Society of Mechanical Engineers, 2016.

[9] Jason Mark Jonkman. *Definition of the Floating System for Phase IV of OC3.* Citeseer, 2010.

[10] HH Yoo, RR Ryan, and Richard A Scott. Dynamics of flexible beams undergoing overall motions. *Journal of Sound and vibration*, 181(2):261–278, 1995.

[11] HH Yoo and SH Shin. Vibration analysis of rotating cantilever beams. *Journal of Sound and vibration*, 212(5):807–828, 1998.

[12] J Chung and Hong Hee Yoo. Dynamic analysis of a rotating cantilever beam by using the finite element method. *Journal of Sound and Vibration*, 249(1):147–164, 2002.

[13] Hong Hee Yoo, Jung Hun Park, and Janghyun Park. Vibration analysis of rotating pre-twisted blades. *Computers & Structures*, 79(19):1811–1819, 2001.

[14] Marco António Costa Fonseca Lima et al. Rotating cantilever beams: Finite element modeling and vibration analysis. 2013.

[15] Metin O Kaya. Free vibration analysis of a rotating timoshenko beam by differential transform method. *Aircraft engineering and aerospace Technology*, 78(3):194–203, 2006.

[16] MNV Ramesh and N Mohan Rao. Free vibration analysis of pre-twisted rotating fgm beams. *International Journal of Mechanics and Materials in Design*, 9(4):367–383, 2013.

[17] Andrew Cordle, Jason Jonkman, et al. State of the art in floating wind turbine design tools. In *The Twenty-first International Offshore and Polar Engineering Conference*. International Society of Offshore and Polar Engineers, 2011.

[18] Jason M Jonkman, Marshall L Buhl Jr, et al. Fast user's guide. *National Renewable Energy Laboratory, Golden, CO, Technical Report No. NREL/EL-500-38230*, 2005.

[19] PJ Moriarty and AC Hansen. Aerodyn theory manual.

[20] Erin Elizabeth Bachynski. Design and dynamic analysis of tension leg platform wind turbines. 2014.

[21] Norwegian Marine Technology Research Insitute(MARINTEK). Simo user's manual.

[22] Norwegian Marine Technology Research Insitute(MARINTEK). Riflex user's manual.

[23] Martin OL Hansen. *Aerodynamics of Wind Turbines*. Routledge, 2013.

[24] Jason Jonkman, Sandy Butterfield, Walter Musial, and George Scott. Definition of a 5-mw reference wind turbine for offshore system development. *National Renewable Energy Laboratory, Golden, CO, Technical Report No. NREL/TP-500-38060*, 2009.

[25] Robert D Cook et al. *Concepts and applications of finite element analysis*. John Wiley & Sons, 2007.

[26] Harald Ormberg, Erin E Bachynski, et al. Global analysis of floating wind turbines: Code development, model sensitivity and benchmark study. In *The Twenty-second International Offshore and Polar Engineering Conference*. International Society of Offshore and Polar Engineers, 2012.

[27] Bjarne Skovmose Kallesøe. Equations of motion for a rotor blade, including gravity, pitch action and rotor speed variations. *Wind Energy*, 10(3):209–230, 2007.

[28] BJ Jonkman and JM Jonkman. Addendum to the user's guides for fast, a2ad, and aerodyn released march 2010-february 2013. *National Renewable Energy Laboratory: Golden, Colorado*, 2013.

[29] Erin E Bachynski, Maxime Thys, Thomas Sauder, Valentin Chabaud, and Lars Ove Sæther. Real-time hybrid model testing of a braceless semi-submersible wind turbine: Part ii—experimental results. In *ASME 2016 35th International Conference on Ocean, Offshore and Arctic Engineering*. American Society of Mechanical Engineers, 2016.

[30] Bonnie J Jonkman. Turbsim user's guide: Version 1.50. 2009.

[31] Erin E Bachynski and Torgeir Moan. Hydrodynamic modeling of tension leg platform wind turbines. In *ASME 2013 32nd International Conference on Ocean, Offshore and Arctic Engineering*. American Society of Mechanical Engineers, 2013.

[32] Erin E Bachynski, Valentin Chabaud, and Thomas Sauder. Real-time hybrid model testing of floating wind turbines: sensitivity to limited actuation. *Energy Procedia*, 2015.